SANDIA REPORT
SAND2006-1053
Unlimited Release
Printed April 2006

Decomposition of Contaminants Using Photochemically Active Nanoparticles

Kevin F. McCarty, Blake A. Simmons, Timothy J. Boyle, Sherrika D. Daniel, Thomas Zifer, Evelyn Cruz, Michael Lattman, Jup T. Polanams, Dwight R. Jennison, Daniel H. Morse, Scott Spangler, W. Miles Clift, and Richard A. Kemp

Prepared by
Sandia National Laboratories
Albuquerque, New Mexico 87185 and Livermore, California 94550

Sandia is a multiprogram laboratory operated by Sandia Corporation,
a Lockheed Martin Company, for the United States Department of Energy's
National Nuclear Security Administration under Contract DE-AC04-94AL85000.

Approved for public release; further dissemination unlimited.

Sandia National Laboratories

Issued by Sandia National Laboratories, operated for the United States Department of Energy by Sandia Corporation.

NOTICE: This report was prepared as an account of work sponsored by an agency of the United States Government. Neither the United States Government, nor any agency thereof, nor any of their employees, nor any of their contractors, subcontractors, or their employees, make any warranty, express or implied, or assume any legal liability or responsibility for the accuracy, completeness, or usefulness of any information, apparatus, product, or process disclosed, or represent that its use would not infringe privately owned rights. Reference herein to any specific commercial product, process, or service by trade name, trademark, manufacturer, or otherwise, does not necessarily constitute or imply its endorsement, recommendation, or favoring by the United States Government, any agency thereof, or any of their contractors or subcontractors. The views and opinions expressed herein do not necessarily state or reflect those of the United States Government, any agency thereof, or any of their contractors.

Printed in the United States of America. This report has been reproduced directly from the best available copy.

Available to DOE and DOE contractors from
U.S. Department of Energy
Office of Scientific and Technical Information
P.O. Box 62
Oak Ridge, TN 37831

Telephone: (865) 576-8401
Facsimile: (865) 576-5728
E-Mail: reports@adonis.osti.gov
Online ordering: http://www.doe.gov/bridge

Available to the public from
U.S. Department of Commerce
National Technical Information Service
5285 Port Royal Rd
Springfield, VA 22161

Telephone: (800) 553-6847
Facsimile: (703) 605-6900
E-Mail: orders@ntis.fedworld.gov
Online order: http://www.ntis.gov/help/ordermethods.asp?loc=7-4-0#online

SAND2006-1053
Unlimited Release
Printed April 2006

Decomposition of Contaminants Using Photochemically Active Nanoparticles

Kevin F. McCarty, Blake A. Simmons, Thomas Zifer, Evelyn Cruz,
Michael Lattman, and Daniel H. Morse

Sandia National Laboratories
P.O. Box 969
Livermore, California 94551

Timothy J. Boyle, Sherrika D. Daniel, Jup T. Polanams,
Dwight R. Jennison, Scott Spangler, and Richard A. Kemp

Sandia National Laboratories
P.O. Box 5800
Albuquerque, NM 87185

Abstract

The decomposition of hazardous biological (viruses and bacteria) and non-biological (e.g., nerve agents, H_2S, HCN) compounds can be realized using a new class of photochemically active nanoparticles that have been fine-tuned for decontamination applications. Several metal oxides (TiO_2, ZnO, Fe_2O_3, WO_3) have demonstrated the ability to destroy contaminants upon exposure to UV light. However, to make them of practical use, improving their activity is necessary. These materials work by photoactivating water and oxygen to create highly reactive species (e.g., OH•) that readily decompose the compounds described above. This project researched developing a new class of highly photoactive materials by combining: scientific investigation into the mechanisms of photocatalysis, advanced techniques to synthesize nanoparticles, and testing the ability of these materials to destroy simulants of CBW/NTA agents. In-situ microscopy established that the photocatalytic activity occurred uniformly over a TiO_2 surface. A large number of nanomaterials were synthesized and evaluated. Two main nanoparticle synthesis routes were explored: (A) solution routes and (B) solvothermal routes. Specialized test equipment was designed and constructed. We discovered a large number of doped-TiO_2 materials that were less active than un-doped TiO_2. However, our testing showed that several materials synthesized were more catalytically active than any un-doped material, including newly commercialized TiO_2 nanoparticles.

Contents

1. Introduction 13

2. Real-time Microscopy of Photocatalysis on TiO_2 Surfaces 15

2.1 Effect of UV irradiation on O_2 reaction with TiO_2 15

2.2 Imaging photochemical decomposition on undoped TiO_2 17

2.3 Imaging photochemical decomposition on metal-doped TiO_2 17

3. Photocatalytic Reactor Design and Testing 19

3.1 Reactor description 19

3.2 Photoreactor Characterization 20

3.3 Photocatalytic Reactor Calibration 25

3.4 Typical Photocatalytic Testing Protocol 26

3.4 Parts list for UV exposure experiments 27

4. Titanium Dioxide Nanoparticle Synthesis Routes 29

4.1 Introduction 29

4.2 Solution Route 30

4.3 High temperature and pressure route 31

5. Nanoparticle Synthesis, Characterization, and Evaluation 32

5.1 Introduction 32

5.2 TiO_2 Nanoparticles 32

5.3 Nitrogen Doped TiO_2 Nanoparticles. 39

5.4 Noble Metal Doped TiO_2 Nanoparticles 43

5.5 Lanthanide doped TiO_2 49

5.6 Doping with $Ln(OR)_3$. 50

5.7 Synthesis of Ln_2O_3 Nanoparticles using MeIm/H_20 prep 51

5.8 Synthesis of Lanthanide Oxide Materials using the Microemulsion Prep 53

5.9. Gadolinium-Doped TiO_2 55

5.10 Synthesis of LnOCl particles using a Parr Digestion Bomb Prep 58

5.11 Doping Ti compounds with Lanthanide Alkoxides using Parr Digestion Bomb .. 59

5.12 Ammonia-Based Lanthanide Doping of TiO_2 61

6. Doping Commercially Available Nanocrystalline TiO_2 69

6.1 Introduction..... 69

6.2 Initial Results and Doping with Lanthanides..... 69

6.3 Enhanced Dispersion and Doping of Commercially Available TiO_2 76

7. Summary 81

Figures

Figure 1. Schematic depiction of photocatalytic mechanism in TiO_2. 13

Figure 2. LEEM images of UV-catalyzed reaction of O_2 with TiO_2. 15

Figure 3. Rate of UV-catalyzed reaction of O_2 with TiO_2. 16

Figure 4. Real-time microscopy of photocatalysis on TiO_2.. 17

Figure 5. LEEM images as a Ag film dewets a TiO_2 (110) surface. 18

Figure 6. Photograph of the Sandia photocatalytic reactor. 19

Figure 7. Schematic depiction of the overall layout of the photoreactor and (inset) photo of the empty case unit. 20

Figure 8. Spectra of the lamps used in the photocatalytic reactor. 22

Figure 9. Warm-up times of two different lamps: (a) 350 and (b) 400 nm. 23

Figure 10. Spatial dependence of light intensity in the photocatalytic reactor with (a) 400 nm, (b) 350 nm, and (c) sample-to-sample variation at 400 nm. 24

Figure 11. Chemical structure and proper chemical name for methyl orange. 25

Figure 12. Plot of photobleaching of the dye, methyl orange, without photocatalyst present at 350 and 300 nm. 25

Figure 13. Plot of data obtained from 5 runs of the photocatalytic degradation of a dye, methyl orange, at 350 nm. 26

Figure 14. La Mer Growth principles for particle growth pathways. 29

Figure 15. Microemulsion based synthesis route to nanophase TiO_2. 30

Figure 16. Experimental setup for the preparation of nanoparticles in hot solution..... 31

Figure 17. Parr digestion bomb for nanoparticle syntheses.. 32

Figure 18. TEM images (left, middle) of nanocrystalline TiO2 synthesized with Triton X-100, and the associated diffuse reflectance plot of the material (right). 33

Figure 19. XRD data taken from heat-treated TiO_2 produced using Triton X-100 with an image of the anatase unit cell, with anatase indexed peak locations presented as red lines. 34

Figure 20. Effect of temperature and time on the crystalline structure and average crystal size of TiO2 synthesized with the microemulsion route. 35

Figure 21. Impact of particle size on photocatalytic activity..... 36

Figure 22. Plot of biocidal efficiency of nanocrystalline TiO2 in the inactivation of *E. coli* cells at 350 nm. 37

Figure 23. TEM images of TiO_2 synthesized with titanium tetraisopropoxide and acetyl acetone.. 37

Figure 24. TEM image and EDS spectrum of "dry" TiO_2 after dispersion in 1-octadecene 38

Figure 25. TEM image and EDS spectrum of a "wet" specimen TiO_2

after dispersion in 1-octadecene 39

Figure 26. Image of TiO_xN_y yellow powder produced after heating..... 40

Figure 27. TEM images of (left) white powder and (right) yellow powder. 40

Figure 28. EDS analysis of TiON powder (left) white powder as-synthesized and (right) yellow powder produced after heating at 400 ^{o}C for 1h. 40

Figure 29. Graph depicting the comparison between different types of TiON in the photocatalytic degradation of methyl orange at 419 nm as a function of processin 41

Figure 30. TEM image of TiON showing large agglomerated particles.. 42

Figure 31. UV-Vis diffuse reflectance plots showing the impact of the N dopant..... 42

Figure 32. Metal particles on TiO_2 (left) and the inverse TiO_2 on metals (right). 43

Figure 33. TEM images (left) of TiO_2-Au doped photocatalyst and (right) EDS of the same indicating the presence of Au and Ti.. 44

Figure 34. Plot showing the comparison between Au-doped and undoped TiO_2 as a function of wavelength 45

Figure 35. Structure of a $(OPy)_2Ti(OPr^i)_2$ alkoxides. 45

Figure 36. Schematic and experimental modification of CdSe materials with TiO_2. 46

Figure 37. Schematic of bifunctionalized phenol 47

Figure 38. Structure plots of (a) $(OPy)_2Ti(OPr^i)_2$ and (b) $(OPy)_2Ti(4AP)_2$. 48

Figure 39. TEM images of Ag nanoparticles. 48

Figure 40. Structure of (a) $Ln(N(SiMe_3)_2)_3$ and (b) $Ln_4(\mu\text{-}ONep)_8(ONep)_4$..... 49

Figure 41. Y-doped TiO_xN_{1-x} (5:1 [Ti]:[Y]) TEM image and EDS spectra..... 50

Figure 42. Er-doped TiO_xN_{1-x} (5:1 [Ti]:[Er]) TEM and EDS spectra..... 50

Figure 43. Plot of photocatalytic degradation of methyl orange with various metal dopants of TiON at 350nm. 51

Figure 44. Pr_2O_3 nanoparticles were approximately 200 nm in size 52

Figure 45. Characterization of Nd_2O_3 nanoparticles 52

Figure 46. Characterization of Eu_2O_3 nanoparticles..... 52

Figure 47. Gd_2O_3 nanoparticles were approximately 10 nm in size..... 53

Figure 48. Characterization of Ho_2O_3 nanoparticles.. 53

Figure 49. Europium oxide material synthesized using a microemulsion prep.. 54

Figure 50. Gadolinium oxide material synthesized using a microemulsion prep. 54

Figure 51. A holmium oxide material synthesized using a microemulsion prep..... 55

Figure 52. Diffuse reflectance plots of the Gd doped TiO_2 57

Figure 53. Photocatalytic efficiency bar graph of the Gd doped materials as a function of wt% Gd..... 57

Figure 54. Hexagonal-shaped PrOCl crystals. 58

Figure 55. Hexagonal-shaped EuOCl crystals. 58

Figure 56. Nanoparticles of Pr-doped TiO_2.. 59

Figure 57. Nanoparticles of Yb-doped TiO_2. 60

Figure 58. Nanoparticles of Tb-doped TiO_2..... 60

Figure 59. Photocatalytic efficiency of Pr doped TiO2 as a function of wavelength..... 61

Figure 60. TEM image and EDS spectrum of 3% Eu doped aggregated TiO_2 utilizing ammonia-based approach..... 62

Figure 61. Left, TEM image of 3% Eu doped TiO_2 heated at 212°C. Right, TEM image of 3% Eu doped TiO_2 heated at 318°C. 62

Figure 62. Left, diffraction pattern of 3% Eu doped TiO_2 heated at 318°C. Right, EDS spectrum confirms no change in the sample composition. 63

Figure 63. TEM image and EDS spectrum of TiO_2 heated at 318°C. 63

Figure 64. Diffuse reflectance plot of the Eu (left) and Yb (right) doped non-dispersed TiO_2 under various conditions and dopant levels. 64

Figure 65. Comparison bar graph of the photocatalytic efficiency of various doped non-dispersed TiO_2 after 45 minutes of exposure at 350 and 419 nm exposures. 64

Figure 66. TEM image shows some loose TiO_2 particles after doping with 0.5% Eu. ... 65

Figure 67. TEM images 0.5% Eu doped TiO_2 heated at 200°C showing loose particles. 65

Figure 68. 0.5% Eu doped TiO_2 utilizing ammonia-based approach at 300°C shows that TiO_2 particles begin to agglomerate. ... 66

Figure 69. TEM images of 1% Yb doped TiO_2 with ammonia-based approach show loose TiO_2 particles in the sample prior to heating ... 66

Figure 70. Left, TEM image shows 1% Yb doped TiO_2 sample at 217°C. Right, TEM image shows the sample at 320°C showing TiO_2 particles ... 67

Figure 71. TEM image of the sample annealed at 400 °C shows heavy agglomeration, no TiO_2 particles were observed ... 67

Figure 72. Bar graph comparison performance plot of the doped TiO2 samples with undoped and commercially available materials at 350 nm after 45 minutes of exposure. ... 68

Figure 73. TEM image of the Aldrich TiO_2 (catalog# 634662) dry sample shows the large particles of mixed anatase and rutile phase ... 69

Figure 74. TEM images of 1% Eu doped agglomerated Aldrich TiO_2 particles dried overnight at 105°C.. ... 70

Figure 75. TEM images of 1% Eu doped agglomerated Aldrich TiO_2 at 135 °C ... 70

Figure 76. Left TEM image shows 1% Eu doped TiO_2 at 221 °C. Right TEM image shows the sample heated at 300 °C. ... 71

Figure 77. Diffuse reflectance plot of 0.5% Eu doped commercial non-dispersed TiO_2 ... 73

Figure 78. Photocatalytic activity of 0.5% Eu doped commercial non-dispersed TiO_2 ... 73

Figure 79. Photocatalytic activity of 1.0% Eu doped commercial non-dispersed TiO_2 ... 74

Figure 80. Photocatalytic activity of 2.0% Eu doped commercial non-dispersed TiO_2 ... 74

Figure 81. Diffuse reflectance plots of 3.0% Eu doped commercial non-dispersed TiO_2 ... 75

Figure 82. Photocatalytic activity of 3.0% Eu doped commercial non-dispersed TiO_2 ... 75

Figure 83. “Dry” TEM images of dispersed Aldrich TiO2 (#634662), showing smaller particles.. ... 76

Figure 84. Left, TEM images of dispersed and washed Aldrich TiO_2. Right, image taken at a 150K magnification showing some particle sizes less than 10nm. 77

Figure 85. TEM image of 1% Eu doped dispersed Aldrich TiO2.. 77

Figure 86 Left, TEM image of 1% Eu doped dispersed Aldrich TiO2 heated at 135°C. Right, TEM image of sample heated at 260°C. 78

Figure 87. UV-Vis diffuse reflectance data from the Eu doped dispersed TiO_2..... 79

Figure 88. Plot of Photocatalytic Activity of Eu Doped/Dispersed TiO_2 with UV exposure at 350 nm 79

Figure 89. UV-Vis diffuse reflectance data from the 0.5% Yb doped dispersed TiO_2 80

Figure 90. UV-Vis diffuse reflectance data from the 1% Yb doped dispersed TiO_2 81

1. Introduction

Since the discovery of photoinduced water cleavage on titanium dioxide (TiO_2) electrodes in the early 1980s,[1] TiO_2 photocatalysts have generated great attention as alternative materials to aid in water and air purification.[2] TiO_2 photocatalysts possess very effective oxidative properties when illuminated with UV light with wavelengths of less than 385 nm. The bandgap for these n-type semiconductors is commonly reported as 3.2 eV.[3] With holes (h^+) and hydroxyl radicals ($OH\cdot$) generated in the valence band, and electrons (e^-) and superoxide ions (O^{2-}) generated in the conduction band, as shown in Figure 1, illuminated TiO_2 photocatalysts can decompose and mineralize organic compounds by participating in a series of oxidation reactions leading to carbon dioxide.[4] It has been shown that TiO_2 photocatalysts are effective in the deactivation of chemicals,[5] bacteria,[6] viruses,[7] and fungi.[8]

This photocatalytic process is unique as compared to other decontaminants in that any byproducts (remaining in contact with the material) from the initial oxidative attack mechanism will be subsequently degraded until the ultimate products, e.g. harmless minerals and carbon dioxide, are produced. This produces a decontamination methodology that is inherently safe and environmentally friendly.[9]

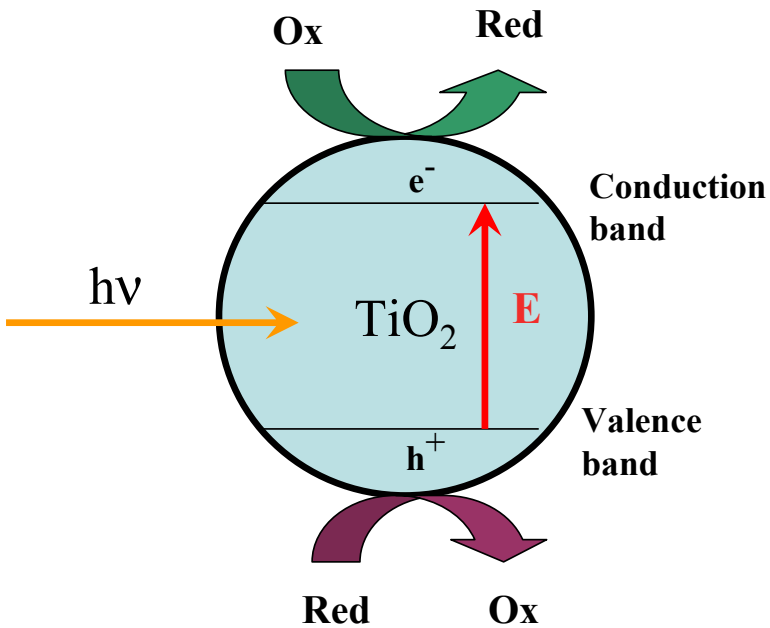

Figure 1. Schematic depiction of photocatalytic mechanism in TiO_2.

---

[1] Borgarello, E.; Kiwi, J.; Pelizzetti, E.; Visca, M.; Graetzel, M. *Nature*, **1981**, 289(5794), 158-60.
[2] Hidaka, H.; Jou, H.; Nohara, K.; Zhao, J. *Chemosphere*, **1992**, 25(11), 1589-97.
[3] Serpone, N.; Pelizzetti, E.; Gratzel, M. *Coordination Chemistry Reviews*, **1985**, 64, 225-45.
[4] Anpo, M. *Studies in Surface Science and Catalysis*, **2000**, 130A, 157-166.
[5] Horikoshi, S.; Hidaka, H.; Serpone, N. *J. of Photochem. and Photobio., A: Chem.* **2004**, 161(2-3), 221-225.
[6] Crittenden, J.C.; Suri, R.P.S.; Perram, D.L.; Hand, D.W. *Water Research*, **1997**, 31(3), 411-418.
[7] Koizumi, Y.; Taya, M. *Biochemical Engineering Journal*, **2002**, 12(2), 107-116.
[8] Hojerova, J.; Jantova, S.; Hanusova, B.; Vollek, W. *SOFW Journal*, **2001**, 127(8), 9,12,14-15.
[9] Pozzo, R.L.; Baltanas, M.A.; Cassano, A.E. *Catalysis Today*, **1997**, 39(3), 219-231.

We set out to develop a fundamental understanding of the processes involved in photocatalysis and synthesize a doped nanocrystalline TiO_2 that can effectively act as a self-regenerative biocide and render CBW/NTA agents inactive upon contact with this surface. To that end, we have developed multiple synthetic and analytical approaches that allow for the realization of various doped nanocrystalline TiO_2 in order to maximize the photocatalytic efficiency of the doped material when compared to bulk TiO_2.[10] The normal bandgap energy of bulk TiO_2 occurs around ca. 365 nm, or 3.2 eV. The presence of dopants can red-shift this energy,[11] thus producing a more active photocatalyst at higher wave-lengths by lowering the required bandgap as evidenced by an observed shift in the absorbance onset values through UV-Vis spectroscopy.[12] The dopants we have found to be the most reactive and efficient are rare earth metal oxides based on erbium,[13] ytterbium,[14] yttrium,[15] and europium.[16] We have shown that these nanocrystalline photo-catalysts are highly effective in the oxidation of a chemical agent simulant dye, methyl orange, which is a standard general indicator of photocatalytic efficiency[17] and free radical attack processes that exist at the surface of the photocatalyst. This process of dye degradation is through an oxidative attack on the dye molecule itself, which is also responsible for the biocidal action of the photocatalyst.[18] This oxidative free radical attack disrupts cellular function by degrading the cell and/or the associated cellular biological coat/membrane, ultimately leading to cell death and biological inactivity of secreted pathogens.

Metal oxides have been demonstrated by us to be effective biocidal agents as well. It is believed that nanophase metal oxides are easily incorporated into the cellular structure itself, and when exposed to appropriate excitation conditions disrupts cellular function and initiates cell death. This has been shown for both vegetative and sporulated cells.[19] We have tested our undoped nanophase TiO_2 in the deactivation of *Escherichia coli* cells in solution. These preliminary results indicate that the presence of dopants will enhance the photocatalytic degradation of CBW/NTA components. We have also developed a route to doped photocatalysts that are significantly more active in visible light conditions by utilizing nitrogen as a dopant as reported in recent journals in the scientific literature.[20]

---

[10] Shah SI, Li W, Huang CP, Jung O, Ni C. *Proceedings of the National Academy of Sciences*, **2002**, 99, 6482-86.
[11] Bessekhouad, Y.; Robert, D.; Weber, J.-V. *Catalysis Today*, **2005**, 101(3-4), 315-321.
[12] Pappa, R.; Cova, U.; D'Angeli, E.; Giongo, M. *Environmental Technology*, **1998**, 19(8), 851-856.
[13] Bahtat, A.; Bouderbala, M.; Bahtat, M.; Bouazaoui, M.; Mugnier, J.; Druetta, M. *Thin Solid Films*, **1998**, 323(1,2), 59-62.
[14] Chiasera, A.; Tosello, C.; Moser, E.; Montagna, M.; Belli, R.; Goncalves, R. R.; Righini, G. C.; Pelli, S.; Chiappini, A.; Zampedri, L.; Ferrari, M. *Journal of Non-Crystalline Solids*, **2003**, 322(1-3), 289-294.
[15] Dutta, N. C.; Bhattacharyya, D. K. *Journal of Radioanalytical and Nuclear Chemistry*, **1996**, 204(1), 167-172.
[16] Garcia-Rocha, M.; Conde-Gallardo, A.; Hernandez-Calderon, I.; Palomino-Merino, R. *Modern Physics Letters B*, **2001**, 15(17, 18 & 19), 769-773.
[17] Comparelli, R.; Fanizza, E.; Curri, M. L.; Cozzoli, P. D.; Mascolo, G.; Passino, R.; Agostiano, A. *Applied Catalysis, B: Environmental*, **2005**, 55(2), 81-91.
[18] Huang Z, Maness, PC, Blake, DM, Wolfrum, EJ, Smolinski, SL, Jacoby, WA. *J. Photochem. and Photobio. A: Chem.*, **2000,** 130, 163-70
[19] Stoimenov PK, Klinger RL, Marchin GL, Klabunde, KJ. *Langmuir,* **2002**, 18, 6679-86.
[20] Chen, S.Z.; Zhang, P.Y.; Zhuang, D.-M.; Zhu, W.-P. *Catalysis Communications*, **2004**, 5(11), 677-680.

2. Real-time Microscopy of Photocatalysis on TiO_2 Surfaces

2.1 Effect of UV irradiation on O_2 reaction with TiO_2

To initiate study of photochemistry using low-energy electron microscopy (LEEM), we studied the effect of UV irradiation on the reaction of oxygen with TiO_2. An oxygen-deficient, rutile crystal was exposed to O_2 at elevated temperature. Under these conditions, the O_2 reacts on the surface with Ti stored in the bulk, forming new TiO_2 crystal. The rate of chemical reaction is measured by the rate at which two different structures form sequentially on the surface. The two structures give different contrast in the LEEM images (Fig. 2). Thus the local rate of chemical reaction is determined from the frequency that the image intensity at a particular spot on the surface oscillates (Fig. 3, left).[21]

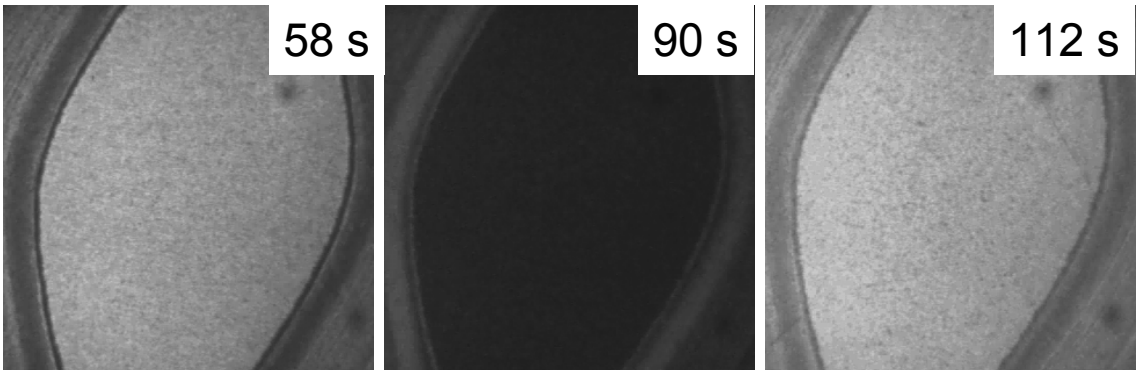

Figure 2. LEEM images of UV-catalyzed reaction of O_2 with TiO_2. Images obtained as the TiO_2 (110) surface at 460°C reacts with $3x10^{-6}$ torr O_2. The feature is a large, atomically flat terrace surrounded by a bunch of atomic steps. The contrast change occurs because the surface cycles through two different surface structures as it reacts with O_2. Images are 3.5 x 3.5 μm^2.

[21] McCarty, K. F.; *Surf. Sci.*, **2003**, 543, 185.

We found that the reaction rate was essentially the same (<5% difference) with and without UV exposure, which came from a Hg lamp (Fig. 3, right). This result is surprising since recent work has shown that the rate at which $SrTiO_3$ reacts with O_2 is significantly enhanced by UV exposure.[22] Since TiO_2 is an n-type semiconductor (unlike p-type $SrTiO_3$), UV irradiation will increase the hole concentration significantly without appreciably changing the concentration of conduction electrons.

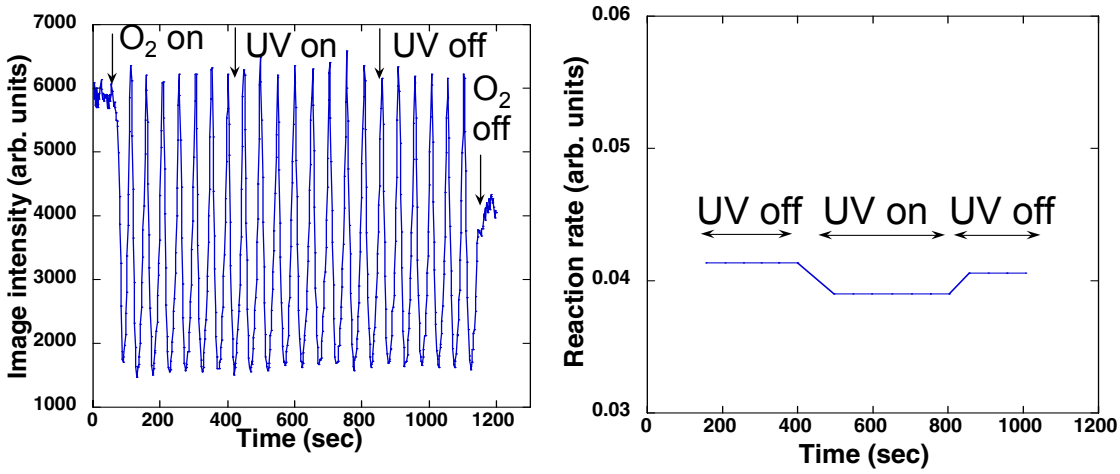

Figure 3. Rate of UV-catalyzed reaction of O_2 with TiO_2. Left. Image intensity versus time as O_2 reacts with TiO_2. As the crystal grows, it cycles through two different surface structures, which appear bright or dark. The oscillation frequency is proportional to the crystal growth rate. The crystal was irradiated with UV light from about 400 to 850 seconds. Right. The reaction rate is essentially unchanged with UV irradiation.

Given the lack of enhancement, we conclude that holes are not involved in the rate-determining step of oxygen's reaction with TiO_2. In addition, we imaged the adsorption/desorption of water with the TiO_2 surface. While adsorption could be clearly observed in the imaging (because of the nearly 1 volt change in work function), we found no spatial variations in H_2O concentration even next to surface steps. This result establishes that spatial gradients in water concentration do not exist.

[22] Merkle, R.; Maier, J.; *Phys. Chem. Chem. Phys.* **2002** *4*, 4140.

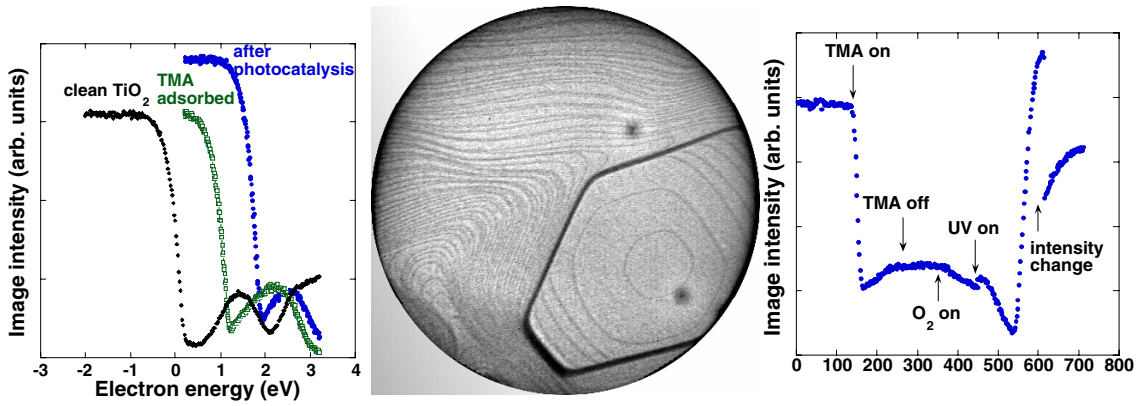

Figure 4. Real-time microscopy of photocatalysis on TiO_2. a) Change in electron reflectivity of TiO_2 surface between clean surface, TMA adsorbed surface, and after photocatalysis. b) LEEM image (5 μm field of view) before adsorption showing atomic steps. c) Change in image intensity during TMA adsorption and photocatalysis.

2.2 Imaging photochemical decomposition on undoped TiO_2

We then used LEEM to image the adsorption and photocatalytic oxidation of trimethlyacetic acid (TMA) on the TiO_2 (110) surface (Fig. 4). The LEEM's electron beam was found to readily decompose the TMA at energies above about 3 eV. Because of this effect, imaging had to be performed at low energies, where the image contrast originates from differences in work function. As shown in Fig. 4 (left), the intensity of the reflected electrons versus electron energy curves change significantly between the clean and TMA covered surface. By properly selecting the electron energy, a large change in image contrast occurred when TMA adsorbed on the surface. The photocatalytic decomposition is illustrated in Fig. 4 (right) – the TMA decomposes when exposed to both UV light and O_2 (O_2 alone has only a small effect). Both the adsorption and decomposition of the TMA occurred uniformly across the surface. That is, atomic steps on the substrate appeared to play no special role. We established that the rate of photocatalytic oxidation could be accurately measured using this approach. We found that the reaction rate increased greatly with O_2 pressure.

2.3 Imaging photochemical decomposition on metal-doped TiO_2

Finally we used LEEM to image the photocatalytic oxidation of trimethlyacetic acid on TiO_2 (110) surfaces that were covered with metal islands. Discrete metal islands were prepared by evaporating metal onto the surface. We examined the coinage metals of Cu, Ag, and Au (Fig. 5). We found that the decomposition of TMA did not occur preferentially around the metal islands. However, our ability to make hard conclusions about the effect of metal dopants on photocatalysis is limited by the resolution limitations imposed by having to image using very low-energy electrons. That is, imaging near the work-function threshold significantly degrades the resolution, making it difficult to image near the metal particles.

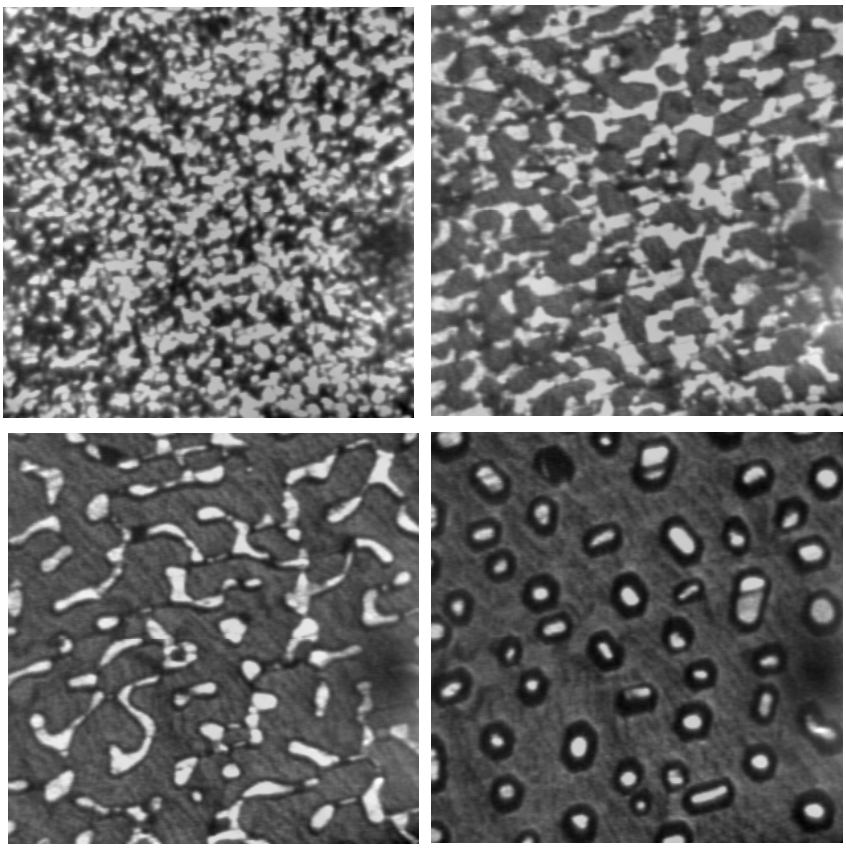

Figure 5. LEEM images as a Ag film dewets a TiO_2 (110) surface. The end state (lower right) after annealing is flat-topped 3D islands of Ag.

3. Photocatalytic Reactor Design and Testing

3.1 Reactor description

We have built a general-purpose system for exposing multiple photocatalyst samples under controlled conditions (Figures 6 and 7). A light-tight aluminum enclosure with a hinged door was assembled from 1/8 inch thick aluminum panels mounted to a frame made from aluminum extrusions and fittings purchased from 80/20 Inc. (see parts list). Interchangeable lamps with peak energies around 254, 300, 350, or 400+ nm were mounted on adjustable brackets to supply a range of UV spectra and intensities. An optical fiber connected to a calibrated UV-Vis spectrometer recorded both the spectrum and the absolute intensity at sample level. A variable-speed shaker table provided controlled agitation of the samples during exposure. Air temperature was automatically controlled by circulating water from a heater/chiller through a heat exchanger. A computer-controlled the UV exposure time as well as the spectrometer. Power to the lamps was interlocked by a switch on the door. We also used a commercially available Rayonet ultraviolet photoreactor in some of the early experiments while the Sandia unit was being fabricated. This reactor consists of a circular ring of lamps that can be removed. We used four sets of wavelengths that were very similar to the ranges stated previously: 254, 300, 350, and 419 nm. The major differences found in the commercial reactor were the lack of power output control, temperature control, and data recording options.

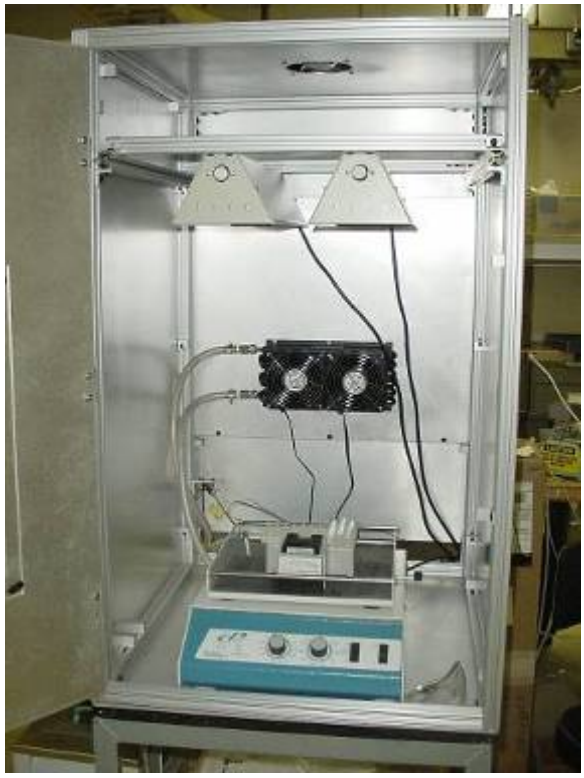

Figure 6. Photograph of the Sandia photocatalytic reactor.

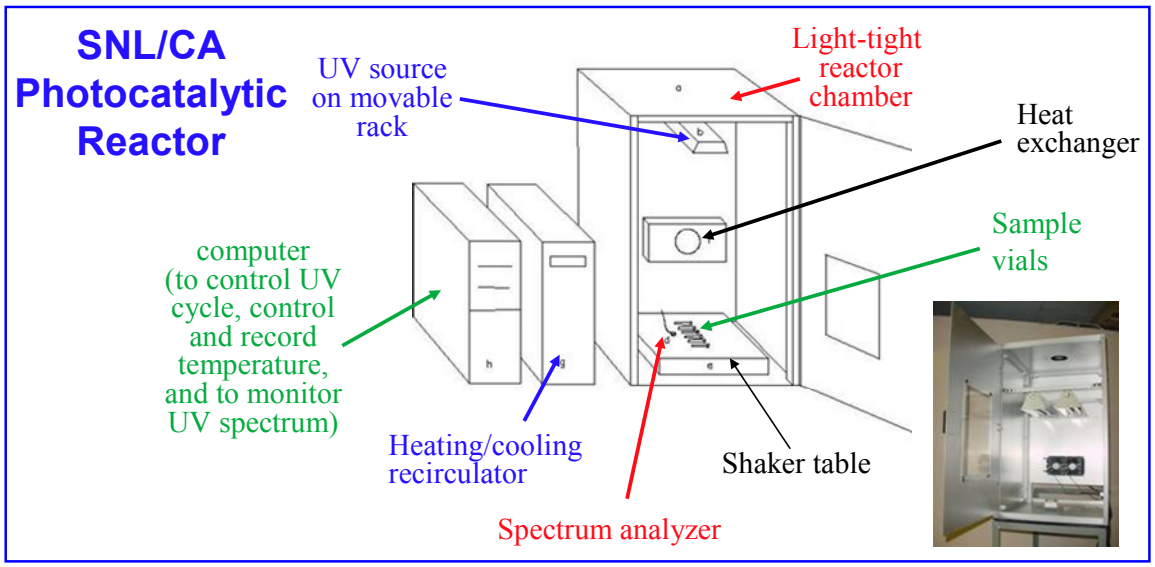

Figure 7. Schematic depiction of the overall layout of the photoreactor and (inset) photo of the empty case unit.

3.2 Photoreactor Characterization

Our first samples consisted of particles suspended in a stoppered quartz cuvette or test tube partially filled with methyl orange solution. In later experiments, we placed fixed catalytic material at the bottom of a Petri dish covered with a known amount of methyl orange. The Petri dishes were covered with a thin, UV-transparent plastic film to minimize evaporation (which could change the methyl orange concentration) and were weighed before and after each exposure. Most of our exposures were made with the samples placed 3.8 cm below the 350 nm lamps. Spectra from our three types of lamps are shown below. A ¼ inch thick UF-4 Plexiglass sheet was placed below a Panacol model UV-H254 lamp to filter wavelengths less than 400 nm (Fig. 6). Spectra of the lamps used in the photocatalytic reactor.

Figure 9 shows the relative lamp intensity as a function of time during warmup. The 350 nm lamp (a) warmed up very rapidly. In the case of the 400 nm lamp (b) the warm-up time is much longer. We eliminated the warm-up effect by covering the samples with an aluminum foil shutter that was removed remotely after five minutes.

Figure 10 shows the spatial variation in flux inside the reactor. Plot (a) shows the variation in flux as a function of transverse distance from the midline between two lamp tubes measured 1.5 inches below the bottom of the tubes. A sheet of aluminum foil was placed under the samples to reflect a fraction of the light back through the samples. The spectrometer was terminated with a cosine corrector with a 2 pi sterradian solid angle that was pointed straight up. Reflected light from the foil was also measured with the sensor looking straight down at about 1 mW/cm2 +/- 0.2mW. The maximum flux was 5.2 mW/cm at the midline, which would make the total radiation ~6.2 W/cm^2 including reflected light.

The cuvettes are approximately 1.5 inches long and the quartz test tubes are approximately 3.5 inches long. Variation across the length of the cuvette would be <3%. The flux at the ends of the test tube would be about 18% less than the flux at the midline. The average level across the whole length of the test tube would be less than 3% lower than the level in the center. There is no measurable variation in the other dimension (along the length of the tubes) over the middle 8 inch distance we normally used. Similar measurements (Fig. 10b) were made with the 400 nm lamps with the bottom of the lamp holder inches above the spectrometer. Flux under the center of the lamp was measured at 4.5 mW/cm2 in the upward direction. At this distance, the variation along the length of the cuvette and test tube are about the same as with the 350 nm lamp. In this case, there is also some variation between sample positions (Fig. 10c). The spectrometer must be centered under the lamp in both directions. With 6 samples, the edge of the outer samples would be 2.125 inch from the center, and the flux would be about 5% low.

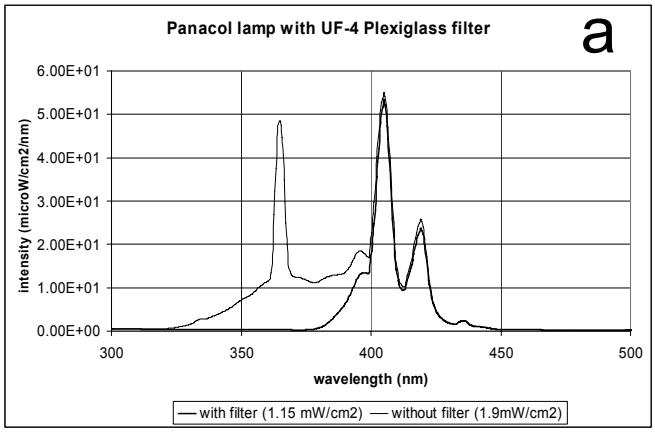

Cal 254 Lamps (Two Pairs of Lamps, 20.5" from Detector)

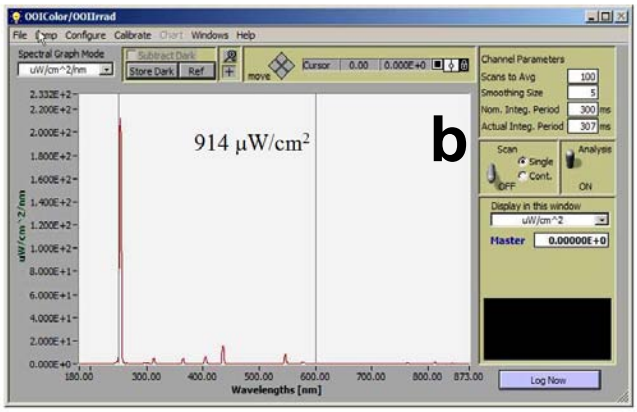

Cal 365 Lamps (Two Pairs of Lamps, 12" and 20.5" from detector)

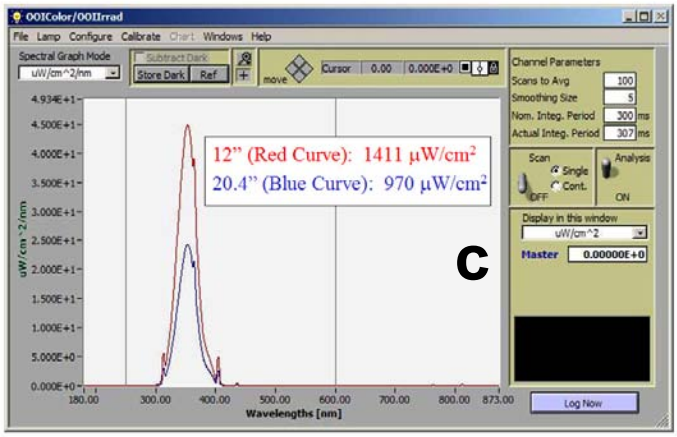

✓ Lamp specifications are for 730 μW/cm² at 12" for one pair of lamps

Figure 8. Spectra of the lamps used in the photocatalytic reactor.

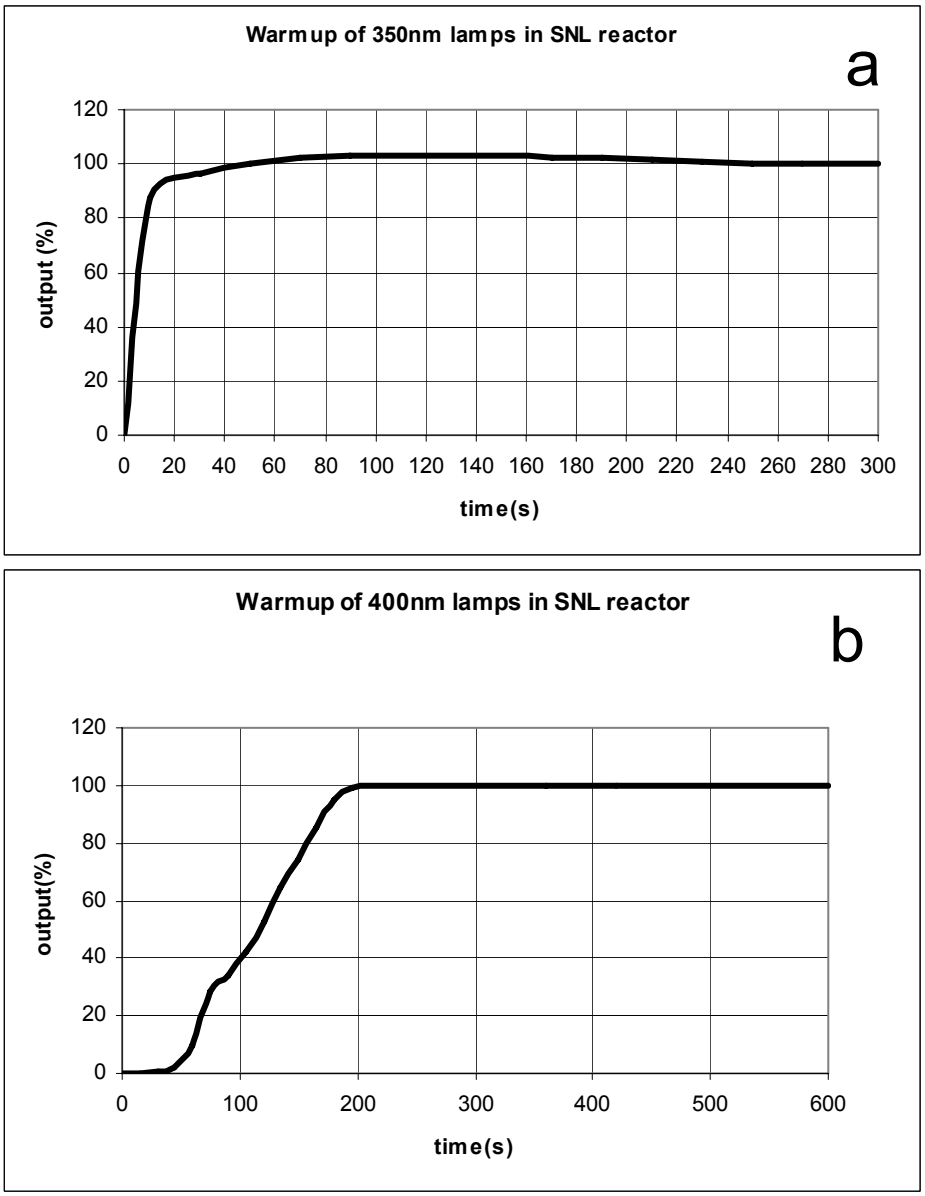

Figure 9. Warm-up times of two different lamps: (a) 350 and (b) 400 nm.

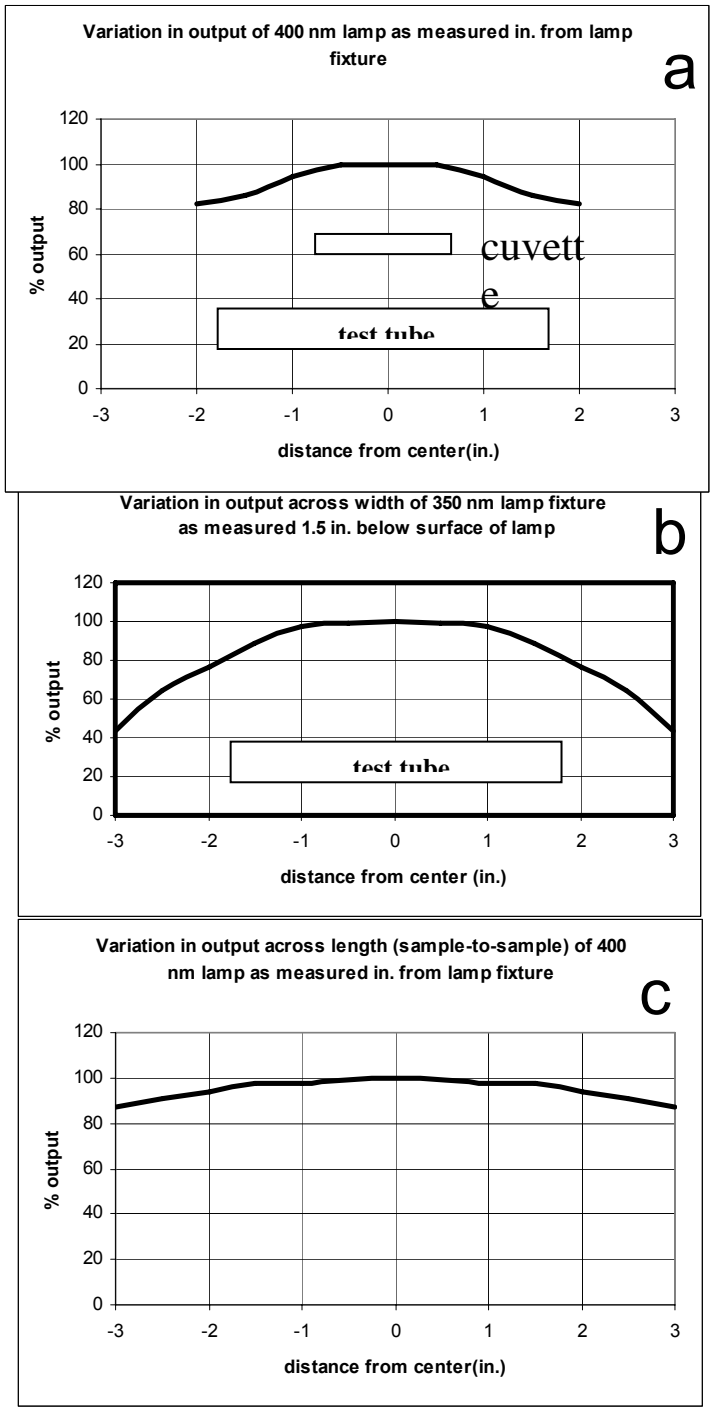

Figure 10. Spatial dependence of light intensity in the photocatalytic reactor with (a) 400 nm, (b) 350 nm, and (c) sample-to-sample variation at 400 nm.

3.3 Photocatalytic Reactor Calibration

In order to ensure that the target photocatalytic analyte, typically a dye (methyl orange), would not photobleach excessively during testing and thus add a "bias" term in the results, calibration plots were generated by exposing solutions of the dye, molecular structure presented in Figure 11, in water to the various wavelengths of illumination without the photocatalyst TiO_2 present. The results are presented in Figure 12 and show that for the case where 350 nm is utilized, little or no degradation of the 4-[4-(dimethylamino)phenylazo]benzenesulfonic acid sodium salt (methyl orange) is observed. It should be noted, however, that at 254 nm the dye will suffer some degradation (~12% over 45 minutes of exposure) due to photobleaching, but at all other wavelengths the loss is minimal as compared to that produced by the photocatalyst.

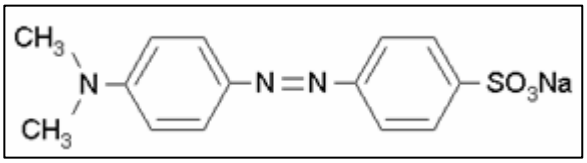

4-[4-(dimethylamino)phenylazo]benzenesulfonic acid sodium salt

Figure 11. Chemical structure and proper chemical name for methyl orange.

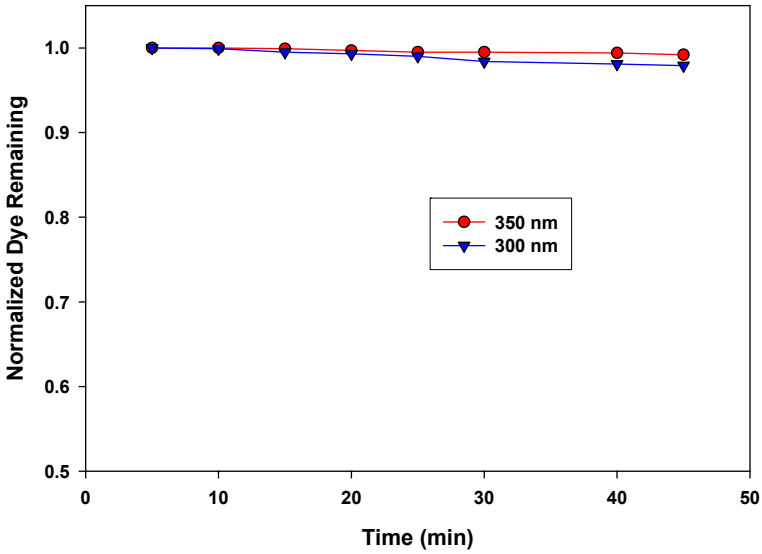

Figure 12. Plot of photobleaching of the dye, methyl orange, without photocatalyst present at 350 and 300 nm.

We also conducted an evaluation of the reproducibility of the data generated by using a commercially available nanocrystalline photocatalyst to degrade methyl orange to demonstrate sample-to-sample and run-to-run reproducibility. Utilizing the procedure detailed in section 3.4 below, a series of 5 different TiO_2 and dye containing solutions was created and the photocatalytic activity recorded at 350 nm as a function of exposure time. The results, shown in Figure 13, indicate that the process is very reproducible and the results show deviations well within normal expectations of experimental variance and yielded no statistically significant outliers.

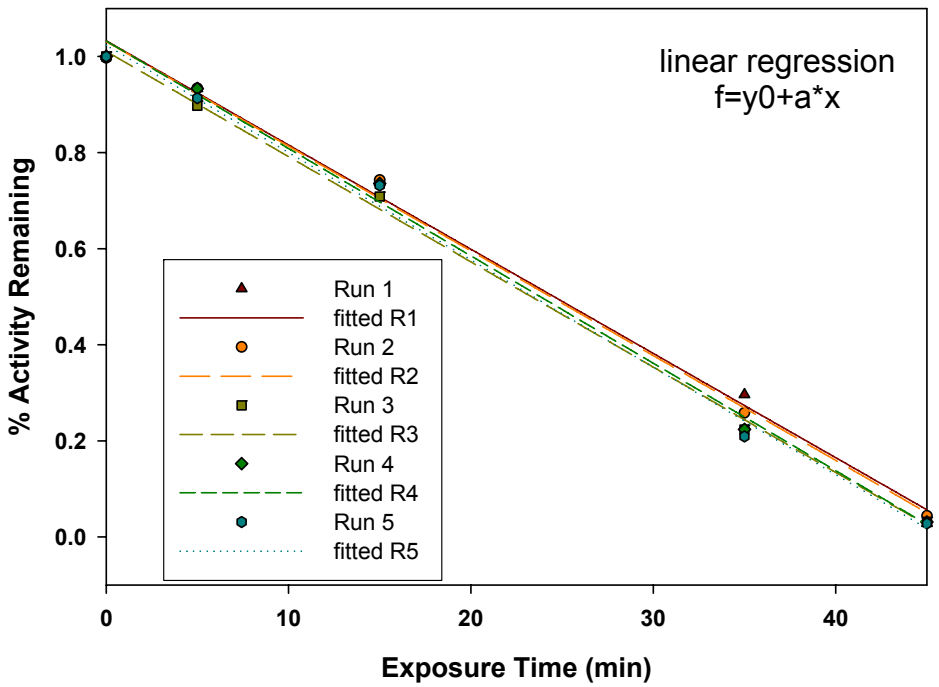

Figure 13. Plot of data obtained from 5 runs of the photocatalytic degradation of a dye, methyl orange, at 350 nm. Data was fitted with a linear regression model, as indicated by the lines in the graph.

3.4 Typical Photocatalytic Testing Protocol

1. Weigh out 10mg of your sample powder
2. Mix your 10mg of sample with 10mL of Methyl Orange dye in PBS concentration of 90 x 10^{-6} mol/L
3. Sonicate for 15min
4. Vortex mix well ~ 10sec
5. Pipette 0.5mL in to Microcon 100K MWCO centrifuge filter tubes (x2) these are the t=0 samples
6. Pipette 7mL from the starting 10mL slurry into a 7mL vial these are your working vials.
7. Attach small pieces of Velcro to side of vial.
8. Place vials max of 10 per experiment on shaker table inside the Sandia National Laboratories photocatalytic reactor.

9. Assure all Velcro pieces are well attached to vial and shaker bed.
10. Set shaker at 250min^{-1}
11. Set desired exposure time using LabView program for SNL reactor
12. Once exposure cycle is done, remove 7mL vials with slurry, vortex well until even mixture ~ 10sec.
13. Pipette 0.5mL into microcon 100K centrifuge tubes (x2)
14. Repeat for all samples
15. Vortex well ~ 10sec before placing the vials back on the shaker table
16. Do second exposure, repeat process until desired total exposure time.
17. Centrifuge all centrifuge tubes at 7,000rpm for 10min.
18. Collect samples and pipette to a 1.5mL UV cuvette
19. Evaluate abs value using UV-vis spectrophotometer

3.4 Parts list for UV exposure experiments

Enclosure

80/20 Inc. extrusions

2 ea 1030 extrusion 40 in. long
2 ea 1020 extrusion 40 in. long
4 ea 1010 extrusion 24 in. long (lamp mount)
8 ea 1010 extrusion 23 in. long (box and lamp mount)
4 ea 1010 extrusion 22 in. long
4 ea 4104 4 hole inside corner bracket
4 ea 4115 4 hole corner bracket
6 ea 4119 2 hole corner bracket (lamp mount)
4 ea 2203 furniture style glide
20 ea 2427 panel mount block
3 ea 2071 black detent hinge
1 ea 2730 locking handle
¼-20 bolts, economy T-nuts, and drop-in nuts as needed

fabricated panels

1 ea UV box top
1 ea UV box bottom
2 ea UV box side
1 ea UV box door
1 ea UV box back
1 ea plastic window (UV opaque Lucite)
1 ea fan panel (for heat exchanger)
1 ea air dam

Lamps

2 ea UV bench lamp, 365 nm, p/n U-97605-10, Cole Parmer
2 ea UV bench lamp, 264 nm p/n U-97605-00, Cole Parmer
1 ea Panacol UV-H 254 hand Lamp (405 nm), Tangent Industries, Inc.

Test tubes

p/n315010 from Quartz Scientific, Inc.
p/n U-62994-08 silicon stopper from Cole Parmer

Heat exchanger

P/n 35145k513, McMaster Carr

Heater/cooler recirculator

Julabo Model F32-HE with 3/8” pipe adapter

Pt100 sensor, p/n 8980003

UV/Vis spectrometer

Ocean Optics model USB2000-UV-VIS

P300-1-SR fiber optic cable

OOIIRRad-C software for absolute irradiance and color

SPECCAL calibration of above

4. Titanium Dioxide Nanoparticle Synthesis Routes

4.1 Introduction

Two main nanoparticle synthesis routes were explored in this project: (A) solution routes and (B) solvothermal routes. There are several approaches for type A routes. One approach is to take a room temperature solution of the desired precursor and inject this into a hot solution of a high boiling solvent and surfactant. This allows for a supersaturation level to be obtained followed by a nucleation shower. Once formed the nanoparticles will undergo Ostwald ripening and increase in size unless a surfactant (or capping ligand) is in place to prevent this from occurring.

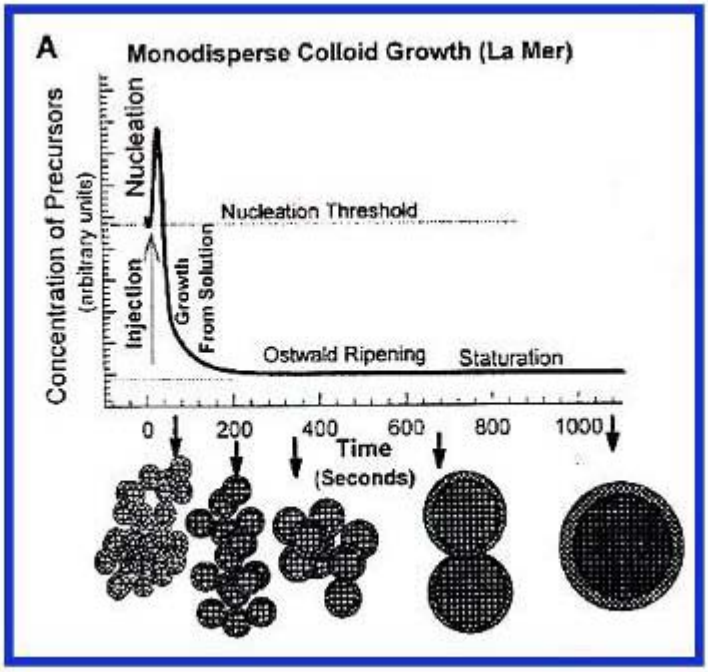

Figure 14. La Mer Growth principles for particle growth pathways.

Figure 14 shows the fundamental behavior of particles over time for these systems, often referred to as the La Mer growth process. In addition to the injection methodology, the utilization of surfactants to serve as templating agents in the form of water-in-oil microemulsions was also employed. In this approach, the cores of the micelles (or reverse micelles) serve as a limiting environment to particle growth through simple spatial confinement of the dynamic reaction environment. This process typically involves the formation of two water-in-oil microemulsions in separate vials that contain the appropriate surfactant and one reactant. These two solutions are then mixed, the contents of the micellar cores mix, and nanoparticle nucleation and growth proceeds, as shown in Figure 15. The use of a surfactant-free solution route, carried out in an acidic environment to produce anatase nanomaterials in a one-pot process, was also investigated.

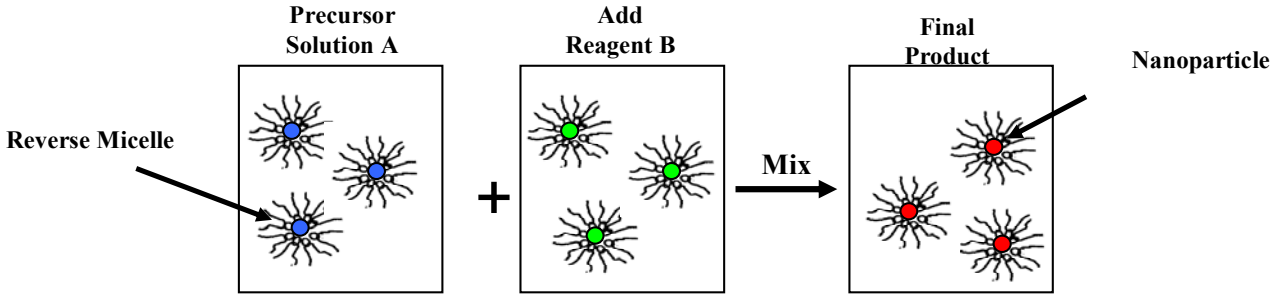

Figure 15. Microemulsion based synthesis route to nanophase TiO_2.

In contrast, for type B routes, high pressures and temperatures allow for the supersaturation to occur. But with no relief from the pressure and the presence of surfactants, crystallization can occur at much lower temperatures. For this investigation both routes were used; however, the majority of results are based on the solution routes.

4.2 Solution Route

For the solution routes, several different methods were used – the two major ones are described below. One solution preparation route employed methyl imidazole/water (MeIm/H_2O) where a 3-neck round bottom flask, equipped with a septum, reflux condenser, and a gas adapter (Fig. 16), methyl imidazole (MeIm) (14.5 mL) and water (H_2O) (0.5 mL) were mixed and refluxed (170 °C). The $M(OR)_x$/solv (solv = toluene or hexanes) stock solution was drawn into a syringe (3.0 mL) in the glovebox, transferred to the Schlenk line, and rapidly injected (~ 1.0 s) into the heated MeIm/H_2O solution. The mixture was refluxed for 0.5 to 2 hrs. After the solution was cooled, centrifuged, and decanted, the MO_x particles were precipitated using another solvent (i.e., acetone, methanol, isopropyl alcohol). The precipitated particles were washed twice with the appropriate solvent. The nanoparticles were then characterized using Transmission Electron Microscopy (TEM) by taking an aliquot of the desired precipitate suspended in hexanes and placing it directly onto a carbon-coated copper TEM grid (300 mesh) purchased from Electron Microscopy Sciences. The aliquot was then allowed to dry. The resultant particles were studied using a Philips CM 30 TEM operating at 300-kV accelerating voltage. The nanoparticles were also characterized by powder X-ray diffraction (XRD). The XRD patterns of the resulting nanoparticles were obtained on a Siemens 5D500 or Scintag diffractometer using Cu KR radiation, excited at 40 kV and 30 mA. The X-rays were collimated at the source with 1° divergence scatter slits with a detector that had 1° scatter and receiving slits using graphite diffracted beam monochromators. Diffuse reflectance data were recorded utilizing a Shimadzu UV-Vis spectrophotometer equipped with an integrating sphere.

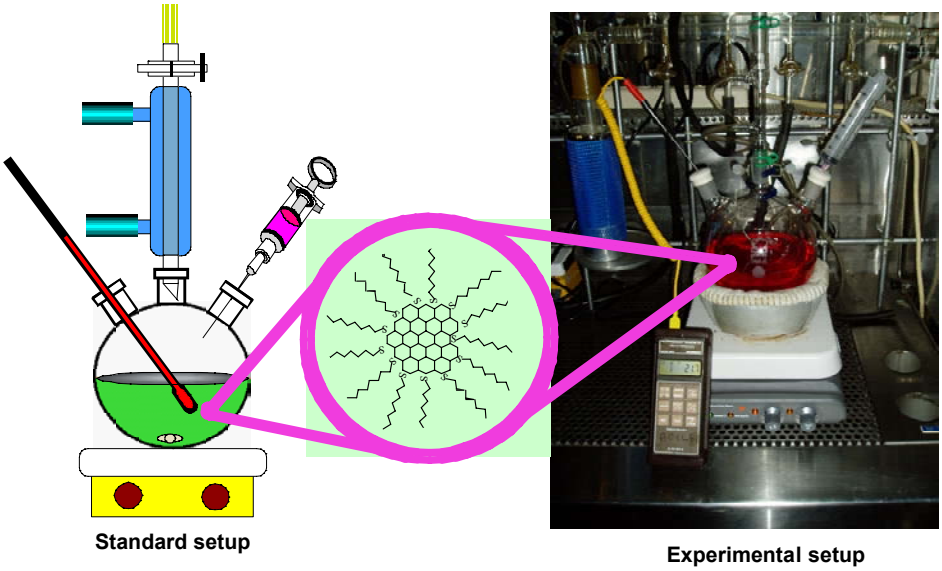

Figure 16. Experimental setup for the preparation of nanoparticles in hot solution. The solvents most commonly used are methyl imidazole (MeIm) and H_2O. The temperature used in this synthesis is 170 °C.

Another method used for nanoparticles synthesis was the microemulsion preparatory route. This method was utilized to form nanocrystalline TiO2 at room temperature through the utilization of the anionic surfactant, dioctyl sulfosuccinate, and the nonionic surfactant Triton X-100. This technique was also applied to the Ln_2O_3 nanoparticles where the commercially available $Ln(NO_2)_3$ (Ln = Eu, Gd, Ho) was dissolved in H_2O/28% $NH_3 \cdot H_2O$ and added to a solution of CTAB/cyclohexane/1-hexanol solution followed by stirring for 30 minutes. The solvent was then removed and the resultant nanoparticles were calcined at 600 °C for 2 hrs. The nanoparticles were then characterized using TEM by taking an aliquot of the desired precipitate suspended in hexanes and placing it directly onto a carbon-coated copper TEM grid. The aliquot was then allowed to dry.

4.3 High temperature and pressure route

Lastly, a high temperature and pressure Parr digestion bomb (Fig. 17) was used for nanoparticle synthesis. Again, for this study this method was only applied to the Ln_2O_3 system. $LnCl_3$ (Pr, Eu) was dissolved in benzyl alcohol and heated at 200 °C for 48 hrs. In the case of doping TiO_2, $Ln(OR)_3$ and $Ti(OR)_4$ were dissolved in benzyl alcohol and heated at 200 °C for 48 hrs. The nanoparticles were then characterized using TEM by taking an aliquot of the desired precipitate suspended in hexanes and placing it directly onto a carbon-coated copper TEM grid. The aliquot was then allowed to dry.

Figure 17. Parr digestion bomb for nanoparticle syntheses. In this high pressure and high temperature technique, the precursor of choice was dissolved in benzyl alcohol and heated at 200 °C for 48 hrs. In the case of doping TiO_2, $Ln(OR)_3$ and $Ti(OR)_4$ were dissolved in benzyl alcohol and heated at 200 °C for 48 hrs.

5. Nanoparticle Synthesis, Characterization, and Evaluation

5.1 Introduction

A variety of nanoparticles and engineered constructs of nanoparticles were characterized and evaluated during this project. The following are broken down into the various subsets of particles synthesized including (A) TiO_2, (B) TiO_xN_y, (C) noble metal (Au, Ag) doped TiO_2, (D) and lanthanide doped TiO_2. We compared the results using commercially available nanocrystalline TiO_2. Details of the synthesis, characterization, and discussion of the photocatalytic results for each type are presented below.

5.2 TiO_2 Nanoparticles

Several different routes were utilized to synthesize nanocrystalline TiO_2. Using approach A to generate anatase (TiO_2) nanoparticles required the use of $Ti(OR)_4$ precursors. Several routes are reported in the literature and most proved to be useful for production of anatase nanoparticles: (a) Colvin *et al*. who used the cross-reduction of a metal halide and a metal alkoxide to form nanoparticles (eq 1),[23] and (b) Stucky and coworkers who used benzyl alcohol as a reductant/modifier (eq 2),[24] and (c) the hydrolysis of titanium tetraisopropoxide with water followed by heating (eq 4). We investigated all of these reactive pathways and several of our own (i.e., MeIm/H_2O route as discussed above and the microemulsion routes).

---

[23] Trentler, T.J.; Denler, T.E.; Bertone, J.F.; Agrawal, A.; Colvin, V.L. *J. Am. Chem. Soc*., **1999**, 121, 1613-1614

[24] Niederberger, M.; Bartl, M.H.; Stucky, G.D. *Chemistry of Materials*, **2002**, 14(10), 4364-4370.

$$Ti(OR)_4 + TiCl_4 \longrightarrow TiO_2 \quad (1)$$

$$Ti(OR)_4 + BzOH \longrightarrow TiO_2 \quad (2)$$

$$Ti(OR)_4 + MeIm/H_2O \longrightarrow TiO_2 \quad (3)$$

$$Ti(OR)_4 + H_2O \longrightarrow TiO_2 \quad (4)$$

In general each route was effective in the synthesis of anatase nanomaterials; however, the materials generated were sometimes identified by TEM to be polydispersed and/or fused nanoparticles, and thus have limited utility in a photocatalytic setting where effective surface areas are key.

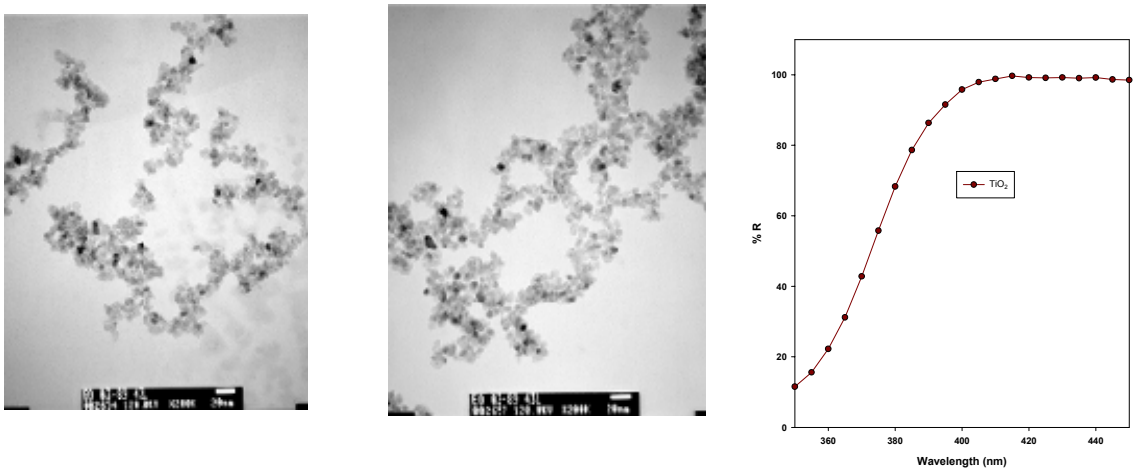

Figure 18. TEM images (left, middle) of nanocrystalline TiO2 synthesized with Triton X-100, and the associated diffuse reflectance plot of the material (right).

One of the most effective techniques to produce nanocrystalline TiO2 was that of the microemulsion route that employed the reaction presented by eq 4.[25] The as-synthesized material produced by this technique is amorphous and must be processed at elevated temperatures for a crystal structure to emerge. For the case that utilized the nonionic surfactant Triton X-100,[26] which forms reverse micelles when dissolved in cyclohexane, very fine nanoparticles were observed through TEM that were processed at 400 ^{o}C to produce the anatase crystal structure (Figure 18). The XRD data for this material is presented in Figure 19 and the average crystallite size produced by a mathematical fit of the data roughly matches that observed in the TEM images very well.

---

[25] Lee, M.; Park, S.; Lee, G.; Ju, C.; Hong, S. *Catalysis Today*, **2005**, 101(3-4), 283-290.
[26] Stathatos, E.; Lianos, P.; Del Monte, F.; Levy, D.; Tsiourvas, D. *Journal of Sol-Gel Science and Technology*, **1997**, 10(1), 83-89.

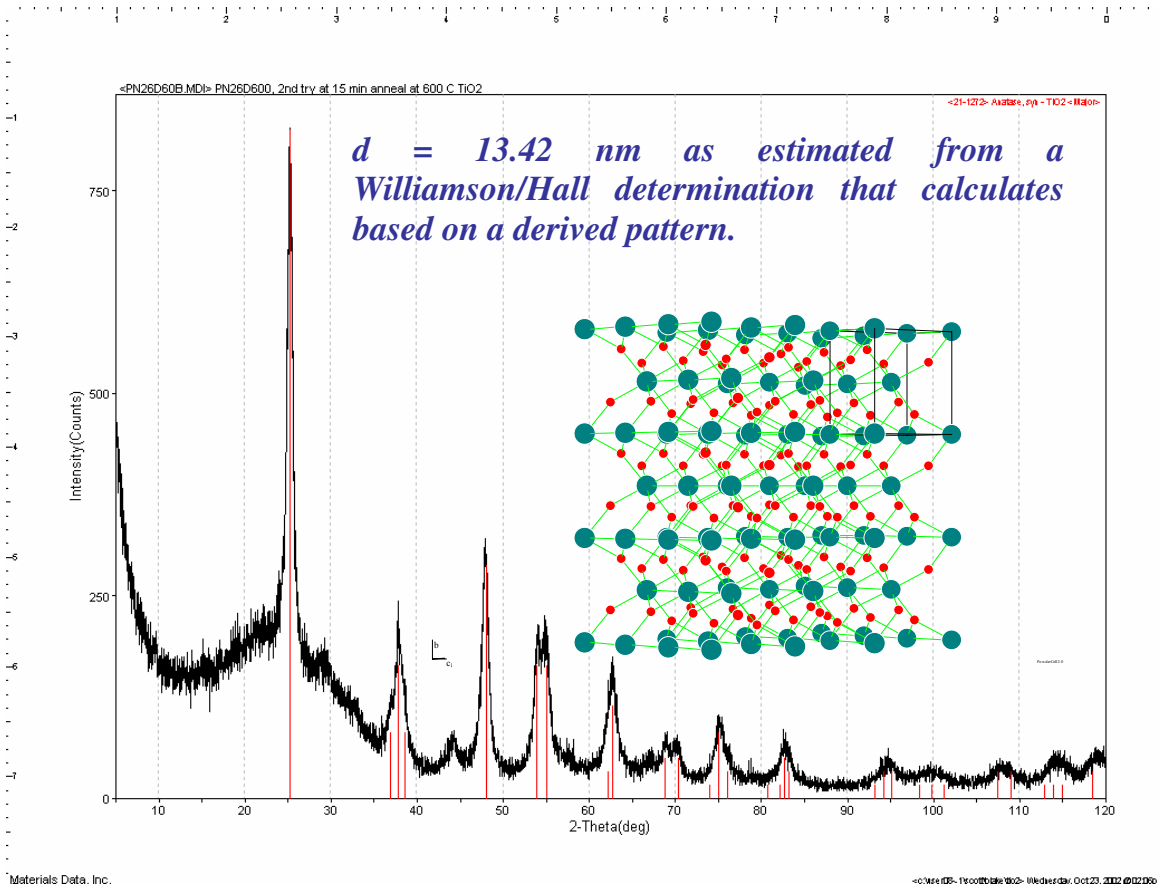

Figure 19. XRD data taken from heat-treated TiO_2 produced using Triton X-100 with an image of the anatase unit cell, with anatase indexed peak locations presented as red lines.

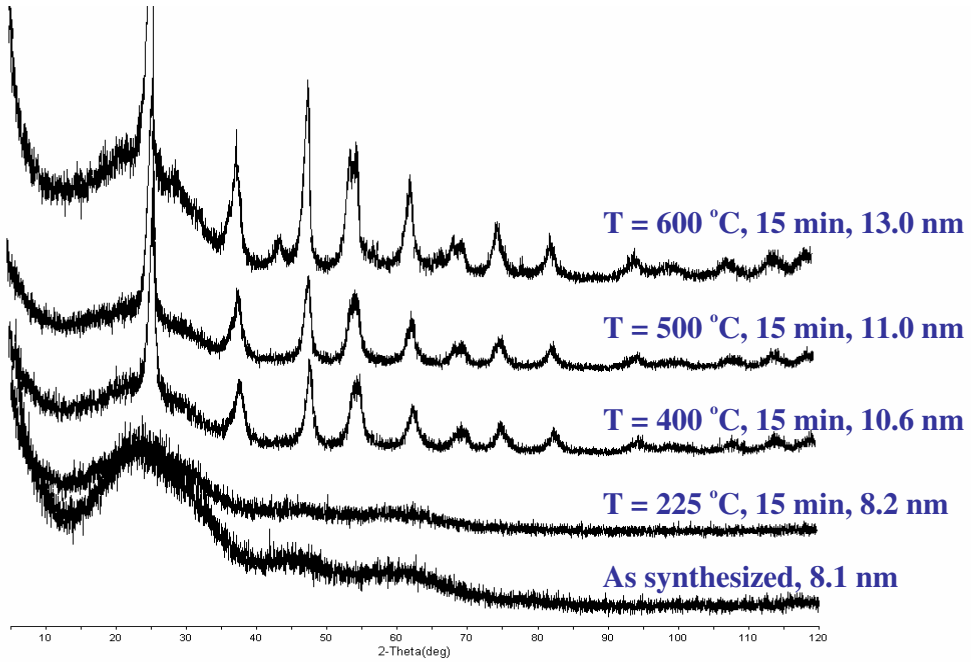

Figure 20. Effect of temperature and time on the crystalline structure and average crystal size of TiO2 synthesized with the microemulsion route.

We also investigated the impact of thermal processing temperature and the time at temperature on the crystal structure and the calculated crystallite size (Figure 20). There is no observed transition from amorphous to anatase until the thermal processing temperature reaches 400 °C. After that, as the temperature is heated there is an observed increase in the average crystal size that corresponds to an annealing effect that is reported in the scientific literature.[27] When the temperature reaches 600 °C, the rutile crystal structure is observed to emerge as faint peaks.

The impact of the particle size on photocatalytic activity is clearly seen in Figure 21. As the particle size decreases, there is also an increase in the effective surface area of the photocatalyst, thus producing an increased rate in degradation of methyl orange at 300 nm illumination.

[27] Colgan, M. J.; Djurfors, B.; Ivey, D. G.; Brett, M. J. *Thin Solid Films*, **2004**, 466(1-2), 92-96.

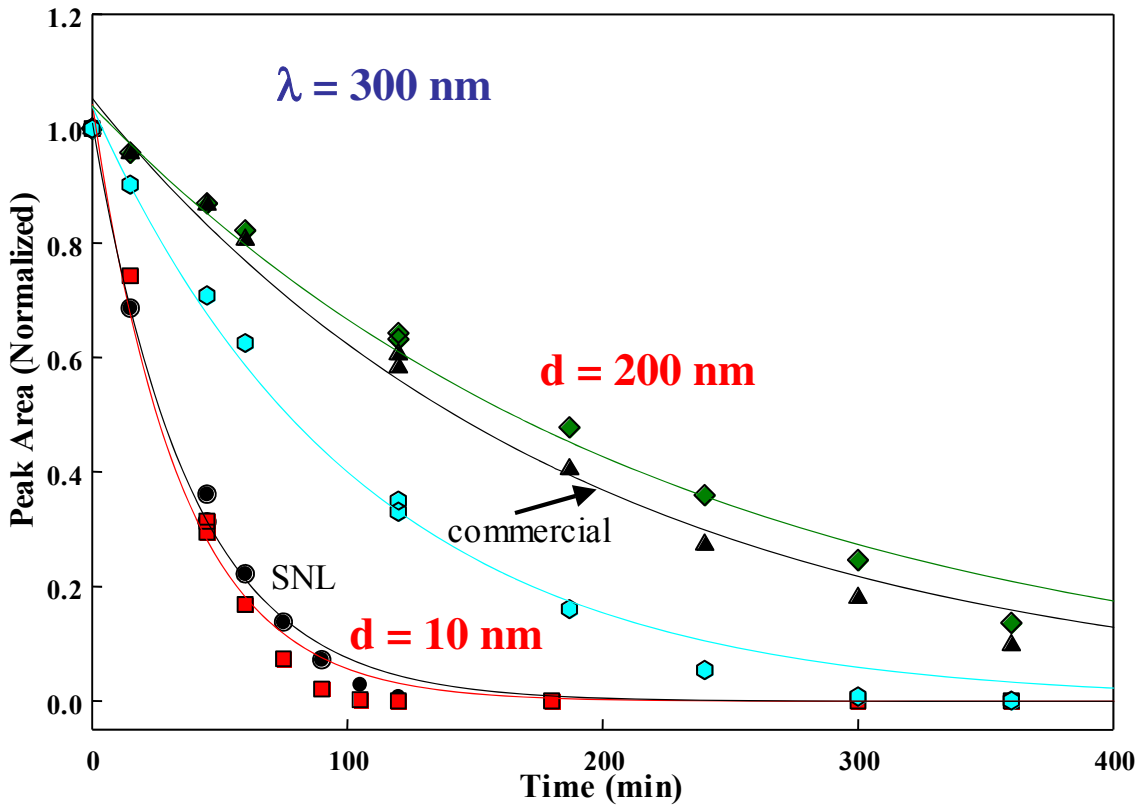

Figure 21. Impact of particle size on photocatalytic activity. Commercially available TiO_2 (d = 200 nm) is much less active than synthesized nanocrystalline TiO_2 (d = 10 nm) with equal weight % loadings of material.

We have also determined that nanocrystalline TiO_2 can act as a strong biocide. We utilized three 22 mL scintillation vials containing 10 mL of a live culture of *E. coli* cells with a cell density of $1x10^6$ cells/mL in each. In one vial, we added 5 mg of commercial 200 nm diameter TiO_2. In another, we added 5 mg of the nanocrystalline TiO_2 reported above. The third vial we used as a control as UV light alone is also known to be an efficient biocidal component. We then illuminated this suspension in the photoreactor at 350 nm. Cell viability was monitored as a function of a chemiluminescent assay for ATP production (one of the key markers of viable cells) through a secondary reaction with luciferase at specific time intervals. Figure 22 indicates that the nanocrystalline TiO2 is the most effective biocidal component evaluated, deactivating 100% of the *E. coli* within 15 minutes of exposure.

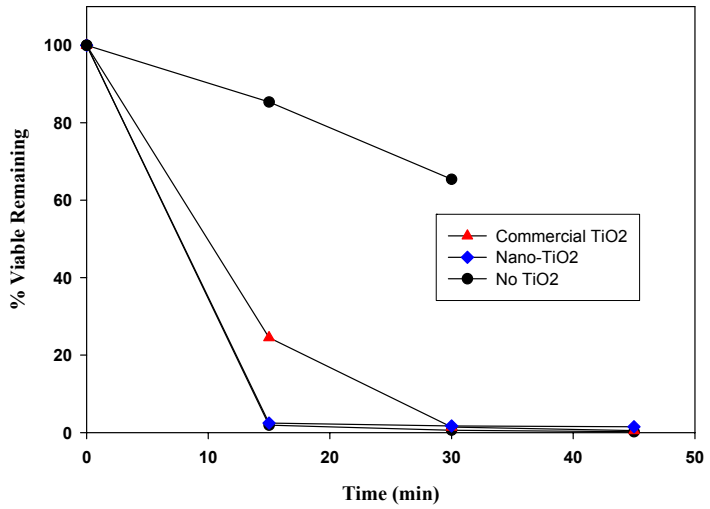

Figure 22. Plot of biocidal efficiency of nanocrystalline TiO2 in the inactivation of *E. coli* cells at 350 nm.

Another technique utilized in the synthesis of TiO_2 calls for equal molar amounts of titanium isopropoxide and acetyl acetone in isopropanol. After reflux for 2 hr, deionized water was added to the solution to precipitate the titania crystals. It was observed that adding deionized water at equal volume or more of the solution allowed more TiO_2 crystals to precipitate, resulting in an increased yield. The solution was centrifuged to collect the milky white pellets and dried at ambient temperature. The yield of the TiO_2 powder is usually between 40 and 50 percent. TEM imaging and EDS analysis were performed on the sample.

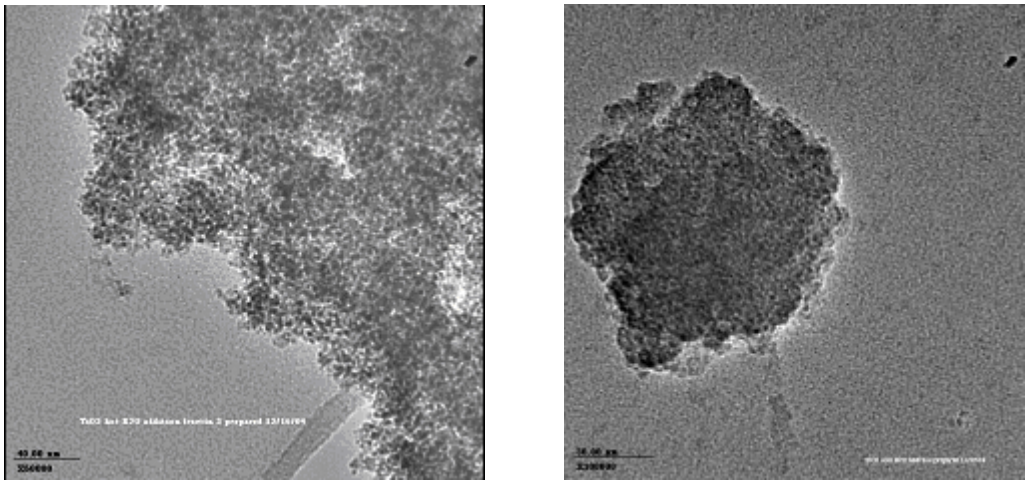

Figure 23. **TEM images of TiO_2 synthesized with titanium tetraisopropoxide and acetyl acetone. Left, image at 60K magnification. Right, image at 100K magnification, showing particles approximately 100nm in size.**

TEM images show that the dried powder crystals obtained by this synthesis (prep#1) are heavily aggregated and do not disperse in water (Figure 23). The EDS analysis (not shown) shows the composition of the fine powder crystals to be titanium and oxygen. All samples for TEM imaging were prepared by suspending the sample in 2% Triton X-100 diluted with ethanol and depositing this on the TEM grid.

From the previously heated TiO_2, a temperature of about 320°C seems to be the ideal temperature for dispersion of flocculated particles. The dispersion synthesis for preparing nanocrystals of iron-oxide, which uses 1-octadecene as a solvent (b.p. 320 °C) to achieve uniform, monodisperse nanoparticles, was modified to suit the current preparation of TiO_2. The previously synthesized were "dissolved" in 1-octadecene with a small amount of HCl added (to control particle size) and refluxed for 1/2 hour. Then, isopropanol was added to precipitate the TiO_2 crystals. The mixture was centrifuged to separate a pellet with an oily, waxy texture. This was washed with isopropanol, yielding a more powdery pellet. The titania powder was dried at ambient temperature. An example of a dry specimen TEM image shows a flocculated powder (Figure 24), which looks similar to the aggregated powder prior to the dispersion synthesis. The dry specimen was prepared by simply dipping the TEM grid into the powder.

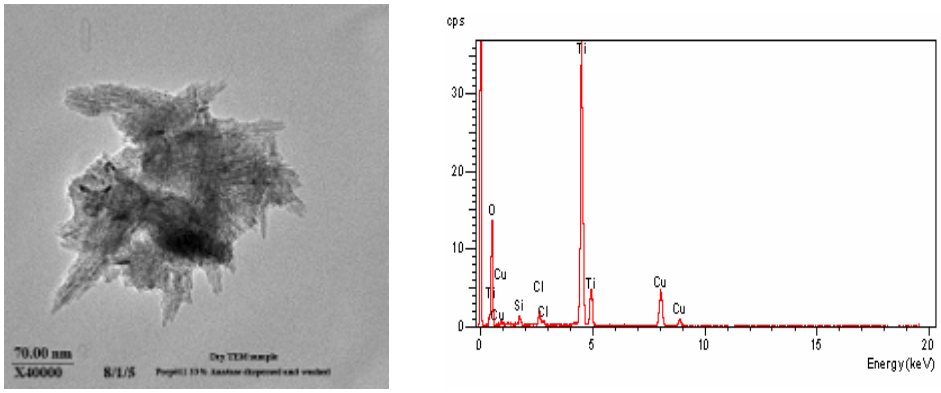

Figure 24. TEM image and EDS spectrum of "dry" TiO_2 after dispersion in 1-octadecene. (Note: the Cl may be from HCl during the dispersion synthesis.)

Unlike the dry powder TEM image, a wet specimen TEM image has a very different characteristic: this shows monodisperse particles with a uniform size of approximately 10 nm (Figure 25). When added to deionized water, the newly made powder produces a glowing, iridescent suspension. This suspension lasts for weeks before settling to the bottom of the water container.

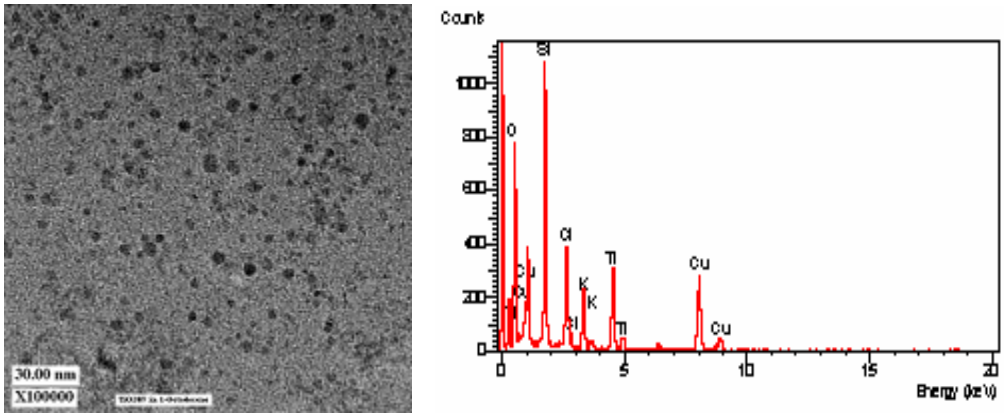

Figure 25. TEM image and EDS spectrum of a "wet" specimen TiO_2 after dispersion in 1-octadecene showing dispersed particles of less than 10nm. (Note: K in the EDS spectrum may be impurities from the TEM instrument.)

5.3 Nitrogen Doped TiO_2 Nanoparticles.

While initial investigations focused on the use of cation dopants, literature reports indicated that anion doping was generating highly active material that was moved into the visual range. Therefore, nitrogen-doped TiO_2 was synthesized by the hydrolysis with ammonium hydroxide as shown in eq 5. The presence of nitrogen incorporated as a substitutional defect has been shown to be a highly effective dopant and is observed to redshift the resultant bandgap of the material into the visible spectrum.[28] The resulting white precipitate was dried *in-vacuo* and then heated at 400 ^{o}C for 1h. Only under an atmosphere of air did a yellow powder form. Using N_2, Ar, O_2, or any other gas attempted yielded only a white powder identified as TiO_2. The white and yellow powders (Fig. 26) were analyzed by powder X-ray diffraction and found to be anatase. TEM analyses indicated that both the white powder and yellow powder are nanomaterials (Fig. 27). The powder proved to be more dispersed prior to heating (white) than afterwards (yellow) where the materials are sintered to some degree. The dark field TEM indicated the yellow powder was crystalline.

$$Ti(OR)_4 + (xs)\ NH_4OH \longrightarrow \text{white powder} \longrightarrow TiO_xN_y \qquad (5)$$

[28] Wang, Z.; Cai, W.; Hong, X.; Zhao, X.; Xu, F.; Cai, C. *Applied Catalysis, B: Environmental,* **2005**, 57(3), 223-231.

Figure 26. Image of TiO_xN_y yellow powder produced after heating.

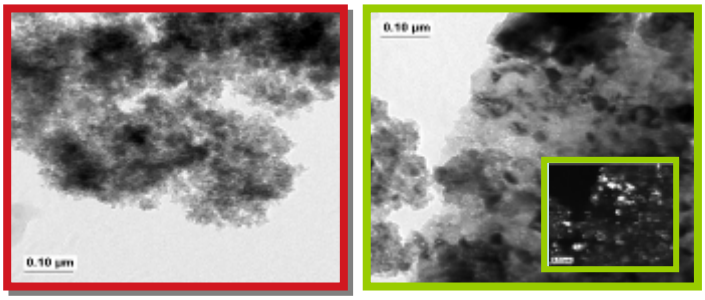

Figure 27. TEM images of (left) white powder and (right) yellow powder. (inset image is darkfield TEM of image on right).

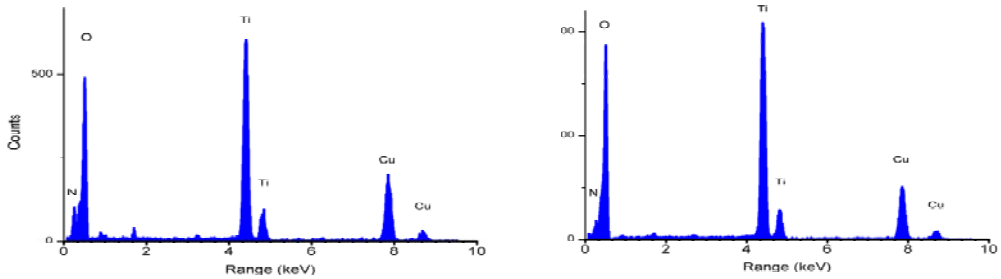

Figure 28. EDS analysis of TiON powder (left) white powder as-synthesized and (right) yellow powder produced after heating at 400 ^{o}C for 1h.

Energy dispersive spectroscopy revealed the presence of nitrogen in both materials (Fig. 28). Raman spectroscopy analyses indicated that both the white and yellow powder were identical. There were two, very-low-intensity Raman bands present in the spectrum of the N-doped anatase but not the commercial anatase that was used as a comparison. These bands occur at 1320 and 1950 cm^{-1}. The 1320 cm^{-1} band was assigned to a fundamental vibration of nitrite (NO_2^-), and the 1950 cm^{-1} band as a combination of the 1320 cm^{-1} band and another nitrite band expected to occur near 600 cm^{-1} (but obscured by anatase bands). It is unusual (but not unknown) that the combination band is more intense than the fundamental

band, as occurs in this spectrum. Elemental analysis (combustion) showed the amount of nitrogen present was ~2 %. Repeated washing and firings with NH_4OH led to increased N levels at ~ 4%; however, we were never able to obtain the levels of N doping reported in the literature. Testing of this material showed the white powder (Fig. 28, left) did not possess increased activity. The materials processed under air that formed the yellow material showed some catalytic activity; however, the material under O_2 (TiON O_2) was identified as anatase with no N present, had even higher activity (Figure 29).

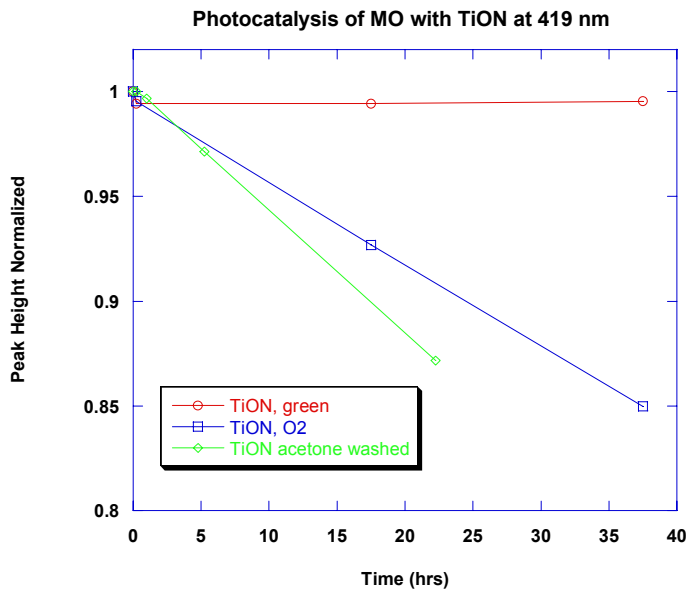

Figure 29. Graph depicting the comparison between different types of TiON in the photocatalytic degradation of methyl orange at 419 nm as a function of processing.

One of the major drawbacks to the TiON synthesized in this fashion was the fact that it does not disperse well in water. TiON composition was determined to be 98.43% anatase (18.08 nm-particle size) and 1.57% rutile (15.37 nm-particle size) by XRD analysis that involved the use of computer model fits of the data. A dispersion synthesis was performed (Figure 30), but this did not change the particle size, according to XRD analysis. The photocatalytic reactivity test also showed poor performance. Attempts to improve this photocatalytic reactivity were performed by two methods that were previously reported in the literature. One method is to mix the rutile phase with the anatase phase to give 25% rutile and 75% anatase; the second method is to heat anatase at a temperature greater than 450 °C, which has been reported as the temperature required for the beginning of anatase to rutile conversion.

The first method was performed by mixing 0.55 gram of TiO_2 with 0.45 gram of TiON. Since the TiO_2 utilized was determined by XRD analysis to have a phase composition of 33% anatase and 67% rutile, the final composition should be approximately 65% anatase. The mixture was mixed in deionized water and sonicated for 1/2 hour. The solution was centrifuged and the pellet was allowed to dry in the hood at ambient temperature. After the centrifugation of the solution, some powder was lost and, hence, the calculated ratio may have

been altered. Both non-dispersed and dispersed TiON powders were used. In the second method, one gram of TiON was heated at 550 °C for 2 hours. Again, both non-dispersed and dispersed TiON powders were heated. The powder begins to turn brown after 1/2 hour of heating at this temperature. After 1 1/2 hr, the powder was very dark brown and appeared to be burnt. After 2 hr, the burnt powder reverted back to the original color of milky yellow.

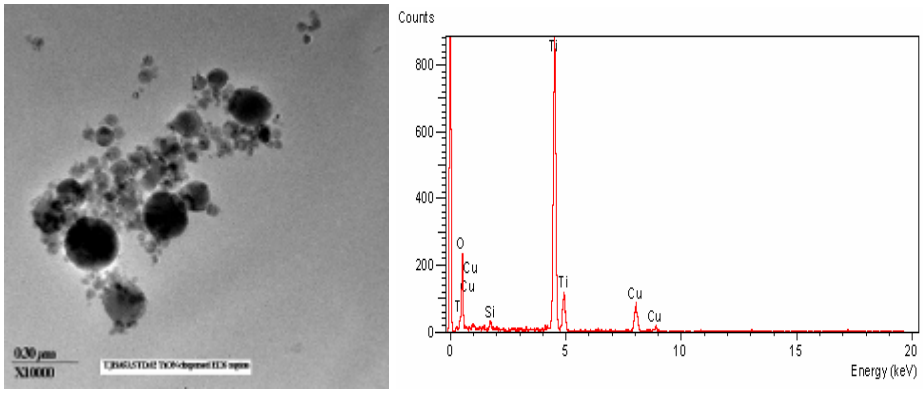

Figure 30. TEM image of TiON showing large agglomerated particles. EDS composition shows the Ti and oxygen composition but N peak cannot be reliably observed because the location of the peak at 1-2 keV cannot be distinct from the other elements in this region.

The diffuse reflectance plots of the doped TiON are presented in Figure 31. As expected, those samples doped with N exhibit a red-shift into the visible spectrum in terms of their respective absorption onsets when compared to normal TiO_2.

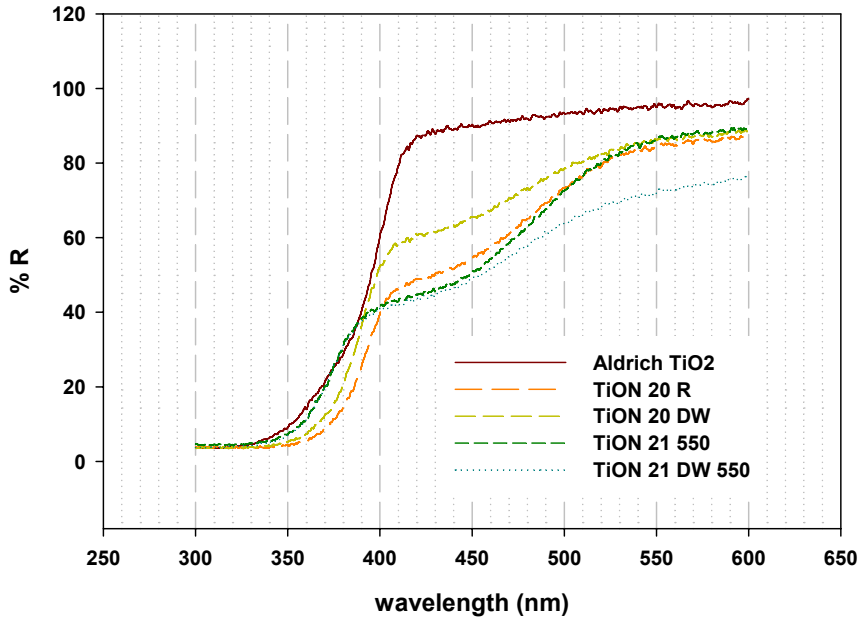

Figure 31. UV-Vis diffuse reflectance plots showing the impact of the N dopant.

5.4 Noble Metal Doped TiO_2 Nanoparticles

Literature reports indicated that noble metals deposited on TiO_2 presented some unique catalytic properties.[29] We pursued two approaches to achieving metal dopants incorporated into a TiO2 photocatalyst. The first followed the techniques reported in the scientific literature where metal salts are reduced on the surface of the TiO_2 to form islands of metal on the surface.[30] Alternatively, we reasoned that high surface area TiO_2 on a metal surface (particularly an active metal) would generate even higher activity. Figure 32 shows a cartoon of the two basic complementary syntheses undertaken that we have termed core-shell and shell-core from the perspective of the TiO2.

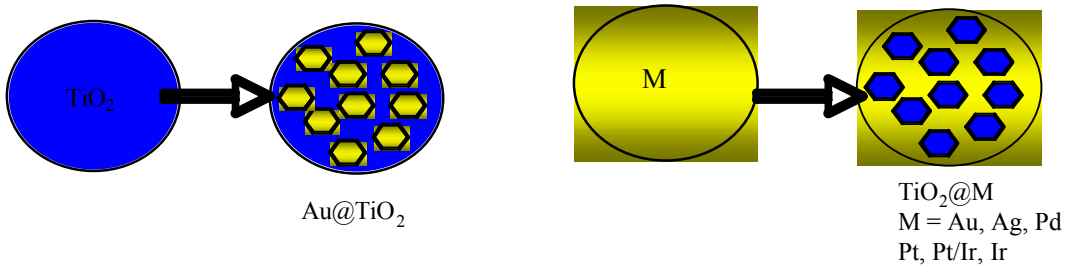

Figure 32. Metal particles on TiO_2 (left) and the inverse TiO_2 on metals (right).

For the methodologies that created metal islands on the TiO2, an image of the typical product is shown in Figure 33. In this process, titanium tetraisopropoxide is hydrolyzed first. Then, $HAuCl_4$ is dissolved into that solution to allow the Au^{3+} ions to become adsorbed onto the surface of the TiO_2. Then, a concentrated solution of $NaBH_4$ is mixed into the solution to reduce the gold ions to a gold metal surface. TEM images show fine deposits of Au within a nanocrystalline TiO_2 matrix (Figure 33). EDS mapping confirms the presence of both Au and Ti.

[29] Zakrzewska, K.; Radecka, M.; Kruk, A.; Osuch, W. *Solid State Ionics*, **2003**, 157(1-4), 349-356.
[30] Haick, Hossam; Segatelian, Yelena; Paz, Yaron. *Langmuir*, **2003**, 19(7), 2540-2544.

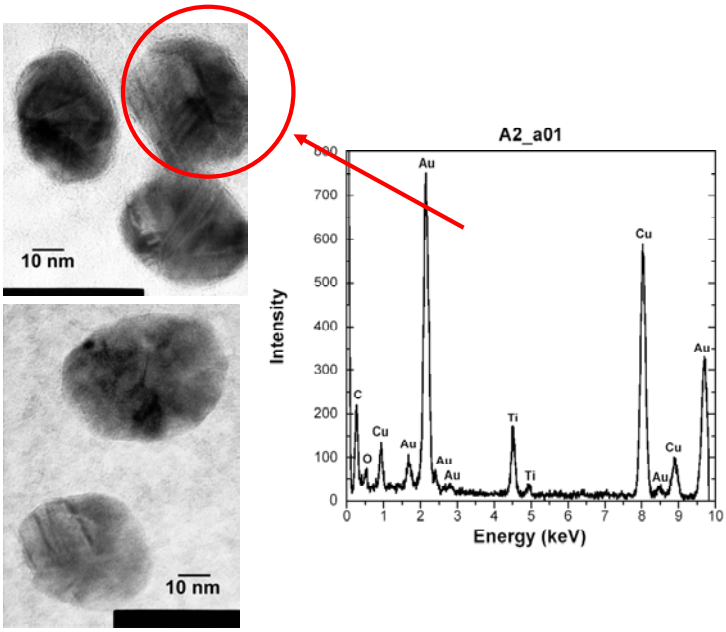

Figure 33. TEM images (left) of TiO_2-Au doped photocatalyst and (right) EDS of the same indicating the presence of Au and Ti. The Cu peaks are attributed to the TEM grid.

The Au-doped samples were then tested to see if there was any improvement to the photocatalytic efficiency observed. The results are shown in Figure 34, and indicate that the presence of the Au dopant positively impacts the catalytic rate of methyl orange degradation for both visible and ultraviolet exposure wavelengths.

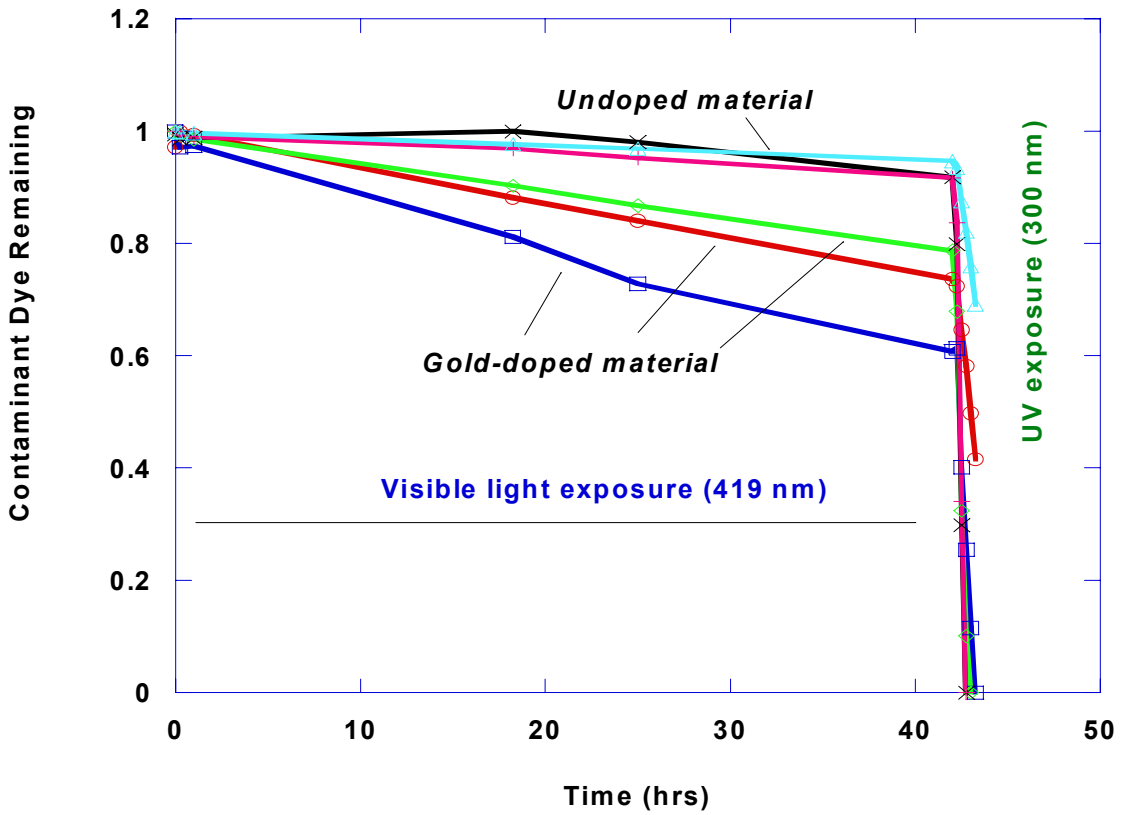

Figure 34. Plot showing the comparison between Au-doped and undoped TiO_2 as a function of wavelength.

In order to realize the inverse type of metal-doped material, with TiO_2 located on the surface of the metallic nanoparticles, we chose to investigate dual functionalized surfactants to prevent aggregation while allowing for complexation with developed metal alkoxides to form TiO_2@M.

The general approach was to use a bifunctional surfactant where one side would preferentially bind to the metal and the other to the alkoxide. Once bound then the alkoxide could be hydrolyzed to form islands of TiO_2 on the surface of the particle. The surfactants were selected based on being long chain alkyls to maximize the separation to insure minimal interaction until desired. The metal-organic species selected and shown below were chosen based on the ability to selectively functionalize the metal and isolate reactive sites or to exploit the functional groups of the ligands already present.

We chose to investigate CdSe initially due to the well-characterized systems already in place for the production of this material. A schematic of the process employed is shown below. Step 1 was the bifunctionalization of a CdSe nanoparticle (the TEMs shown are the actual component of the process). Once bifunctionalized, the particles were reacted with selected amounts of the alkoxide $(OPy)_2Ti(OPr^i)_2$ (see Fig. 35). After this modification, which yielded clusters of compounds by TEM analysis, water was added. Instead of the separate islands of TiO_2, CdSe imbedded in TiO_2 was isolated. It was thought the intersection of each CdSe with the TiO_2 yielded the desired imperfections. Schematics and actual results are shown in Fig. 36. Testing of this material proved difficult since it was insoluble in water and could not be dispersed adequately to maintain catalytic activity for any significant period of time.

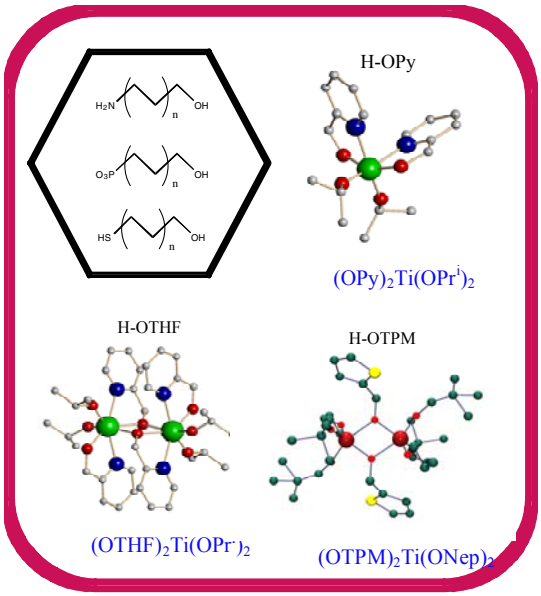

Figure 35. Structure of a $(OPy)_2Ti(OPr^i)_2$ alkoxides.

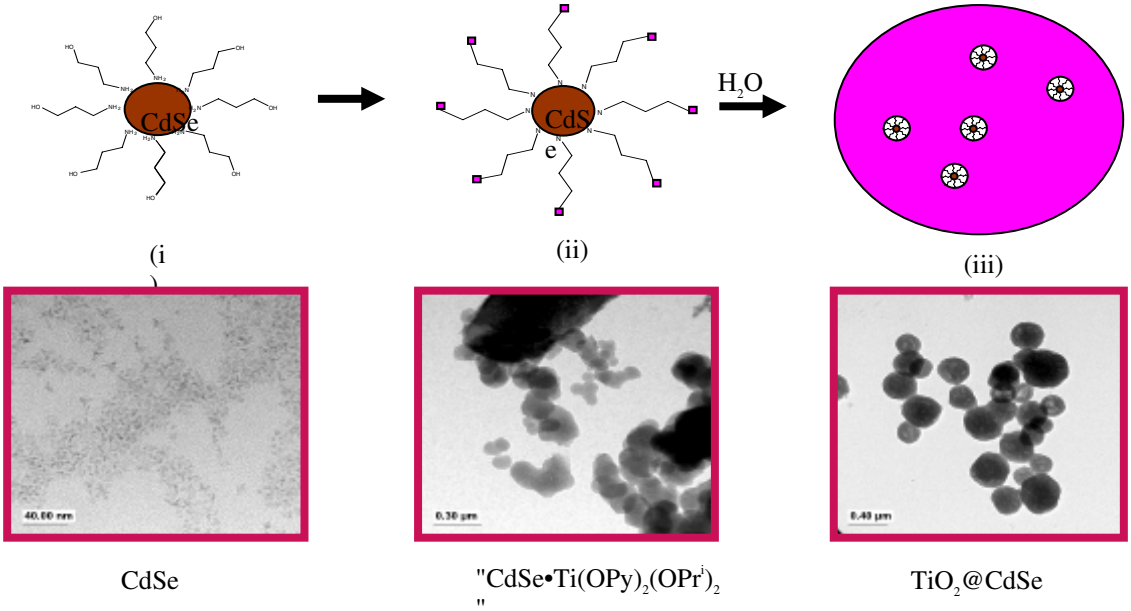

Figure 36. Schematic and experimental modification of CdSe materials with TiO_2.

Therefore, alternative supports were investigated. The first was to investigate the deposition of TiO_2 onto a nanoparticle of Au^o. Again, the basic concept was to functionalize the Au with an amine or thiol leaving the -OH ready for functionalization by a metal alkoxide. For this method, we selected the phenol-substituted surfactants shown in Fig. 37 due to the rigidity of the surfactant. These surfactants were included in place of the standard amine surfactant used in the preparation. Unfortunately, the reduction step for the Au ($AuCl_4$ to Au using $NaBH_4$) makes it difficult to retain the -OH group. That is, the OH is no longer active, either bound to the metal or rendered inert by the BH_4 group.

Therefore, a less demanding reduction was necessary and Ag nanoparticles were therefore studied. Switching to Ag lead to more simplistic reduction pathways (using $AgNO_3$, H_2O, and DMF). Again we generated nanoparticles but instead used the bifunctionalized alkoxide to bind to the surface. These are shown in Fig. 36, where one side of the molecule is sterically encumbered by the bidentate OPy ligand, which consists of a methanol moiety and the bound py ring. The other half of these moieties is available for chemistry. In particular, Fig. 38a has iso-propoxide groups and 38b has NH_2 of the aminophenoxide ligand available for reactivity. These were dissolved in toluene and then added to the synthesis of the Ag nanoparticles.

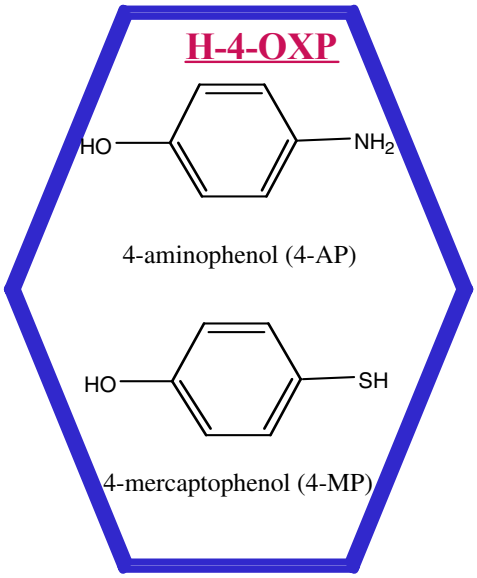

Figure 37. Schematic of bifunctionalized phenol.

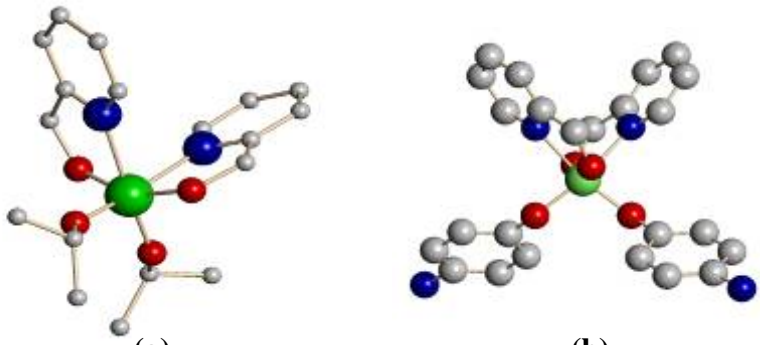

(a) (b)

Figure 38. **Structure plots of (a) $(OPy)_2Ti(OPr^i)_2$ and (b) $(OPy)_2Ti(4AP)_2$.**

Using the simple alkoxide derivative (Fig. 38a) led to the formation of a nanomatrix of TiO_2 with Ag nanoparticles imbedded inside of the network (Fig. 39a). The uncontrolled hydrolysis of the OPr^i ligand allowed for the Ti-O-Ti network to form. Using the aminophenol derivative (Fig. 38b), however, led to Ag nanoparticles surrounded by a skin of TiO_2 material (Fig. 39b).

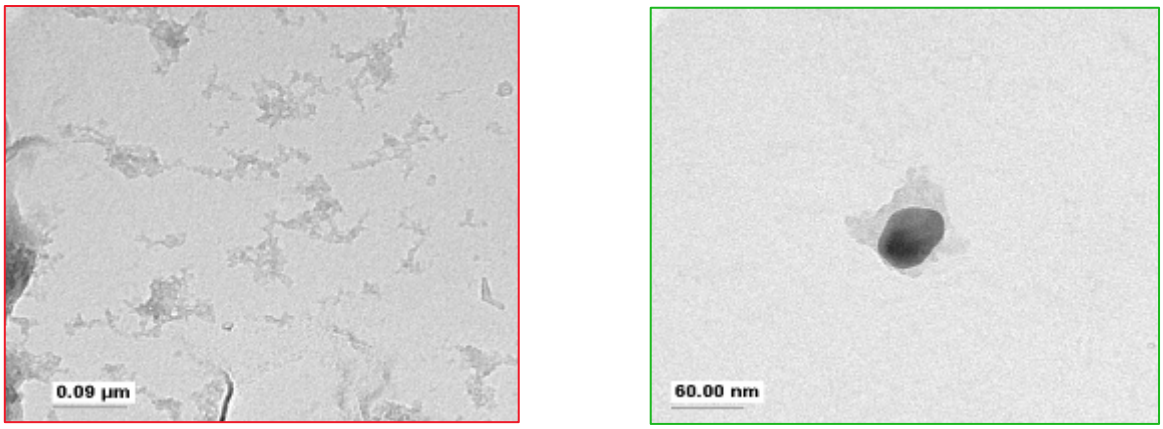

(a) (b)

Figure 39. TEM images of Ag nanoparticles. The nanoparticles were generated in the presence of (a) $(OPy)_2Ti(OPr^i)_2$ and (b) $(OPy)_2Ti(4AP)_2$.

These materials again showed no improvement over the TiO_2 undoped photocatalyst.

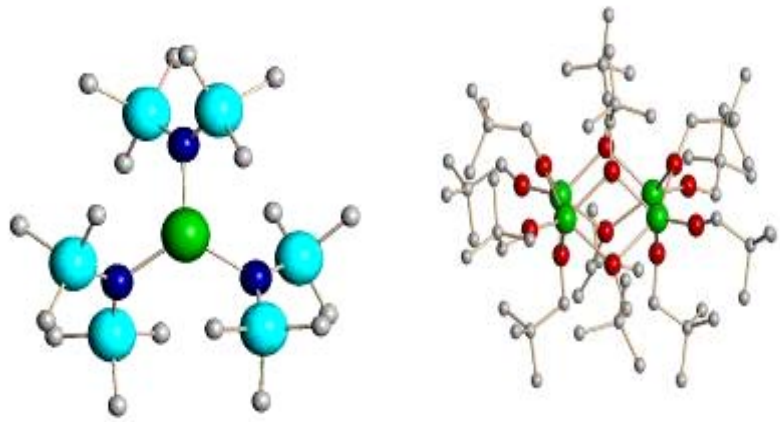

Figure 40. **Structure of (a) $Ln(N(SiMe_3)_2)_3$ and (b) $Ln_4(\mu\text{-}ONep)_8(ONep)_4$**

5.5 Lanthanide doped TiO_2

Due to the success of the photocatalytic activity of the Au doped TiO_2 and TiO_xN_y materials, other dopants were explored. The metals used in the next phase of this study were the lanthanides (Ln). Lanthanide alkoxides $Ln(OR)_x$ were used as dopants for the nano-TiO_2 and TiO_xN_y. A general description of the synthesis of these alkoxide precursors is as follows: Lanthanide amide (eq 5) $Ln(NR_2)_3$ (Ln = Y, Ce, Pr, Eu, Gd, Tb, Ho, Er, Yb, and Lu), were synthesized through the reaction of LnX_3 and three equivalents of ANR_2 (A = Li, K; R =$Si(CH_3)_3$) in THF or Et_2O [3-5]. A hexane solution of HONep (~5 mL) was added dropwise to a vial containing a solution of the appropriate $Ln(NR_2)_3$ complex in ~15 mL of hexane.

$$LnCl_3 + 3\,LiNR_2 \rightarrow Ln(NR_2)_3 + 3\,LiCl \quad (5)$$

$$Ln(NR_2)_3 + 3\,HOR \rightarrow Ln(OR)_3 + 3\,HNR_2 \quad (6)$$

After stirring, the resultant clear reaction mixture concentrated by rotary evaporation and then either cooled at -35 °C or left at room temperature until crystals formed. Fig. 40a shows the structures of the resultant species from eq 5. Lanthanide alkoxide synthesis (eq 6): Lanthanide chloride was reacted with three equivalents of lithium amide and the resultant lanthanide amide was sublimed for purification (twice in some cases) and further reacted with three equivalents of neo-pentanol. This solvent was evaporated from this clear mixture to obtain X-ray quality crystals that were then analyzed by several characterization techniques. Figure 41b shows the structures of the resultant species from eq 6.

5.6 Doping with $Ln(OR)_3$.

Once the appropriate $Ln(OR)_3$ (Ln = Eu, Er, and Y) was synthesized (see above), further investigations began by doping TiO_xN_y with them. In the case of using $Y(OR)_3$ as the dopant, the TEM images (Fig. 41, left) show a nanophase (8.2 nm) material, confirmed anatase TiO_2, and material segregation into Ti-rich and Y-rich areas. The EDS (Fig. 41, right) confirmed ~2 wt% Y in the sample.

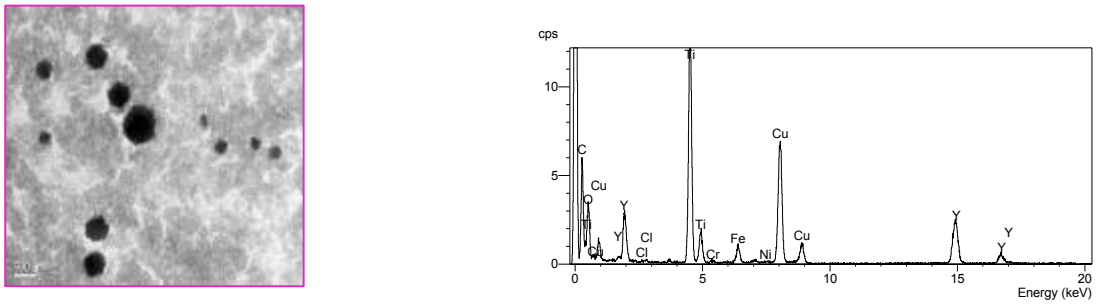

Figure 41. Y-doped TiO_xN_{1-x} (5:1 [Ti]:[Y]) TEM image and EDS spectra. The alkoxides were used to dope TiON in an effort to move the photocatalytic activity to the visible region. The TEM image shows a nanophase (8.2 nm) material, confirmed anatase TiO_2, and material segregation into Ti-rich and Y-rich areas. The EDS confirmed ~2 wt% Y in the sample. The EDS also shows C and Cu peaks, which are a result of the TEM grid.

In the case of using $Er(OR)_3$ as a dopant, the TEM image (Fig. 42, left) shows nanophase (8.2 nm) material, confirmed anatase TiO_2, and no obvious material segregation. The EDS confirmed ~2 wt% Er present in the sample. The photocatalytic results of the Ln-doped TiON materials showed Eu-doped TiON to be the best performer in comparison to TiO_2, Ag-doped TiO_2, Au-doped TiON, and other Ln-doped TiON materials.

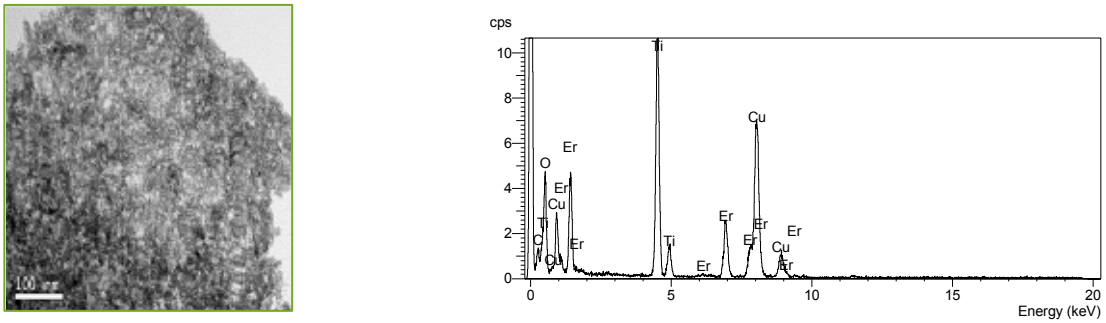

Figure 42. Er-doped TiO_xN_{1-x} (5:1 [Ti]:[Er]) TEM and EDS spectra. The alkoxides were used to dope TiON in an effort to move the photocatalytic activity to the visible region. The TEM image shows nanophase (8.2 nm) material, confirmed anatase TiO_2, and no obvious material segregation. The EDS confirmed ~2 wt% Er present in the sample. The EDS also shows C and Cu peaks, which are a result of the TEM grid.

The photocatalytic testing of these materials based on the modified lanthanide doped TiON are presented in Figure 43. Of the various methodologies and dopants investigated, it appears that the presence of a small amount of Eu has the most positive impact, followed by the Y dopant. The amounts of photocatalyst per sample were held constant for the test. Surprisingly, the presence of Au with the TiON was one of the worst performers, whereas it was one of the best for the TiO_2.

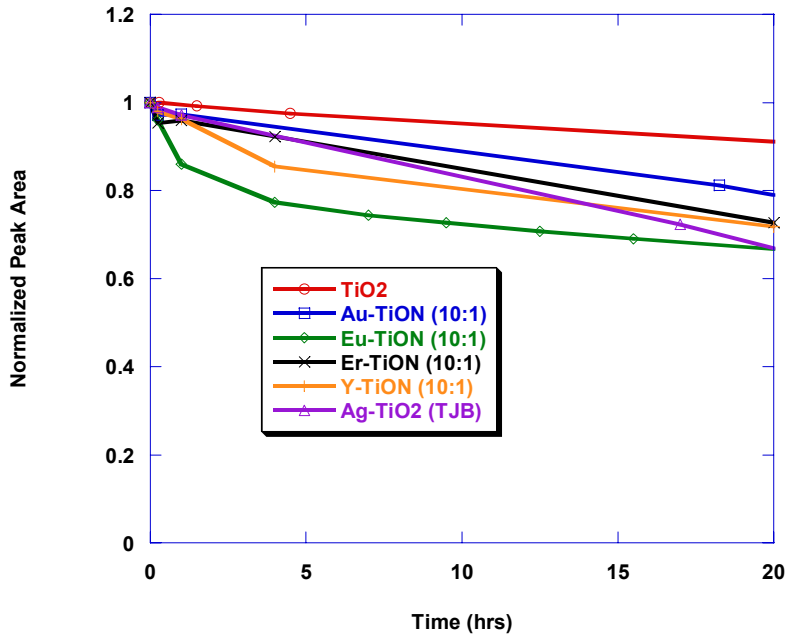

Figure 43. Plot of photocatalytic degradation of methyl orange with various metal dopants of TiON at 350nm.

5.7 Synthesis of Ln_2O_3 Nanoparticles using MeIm/H_20 prep

Due to the success of the photocatalysis of the materials presented above, it was decided to prepare Ln_2O_3 materials by three different preparative routes and with three different ligand sets to further our understanding of the dopant properties and synthesis. The TEM and EDS results of Ln_2O_3 nanomaterial synthesis using the hot solution prep described as shown in Figs. 44-48.

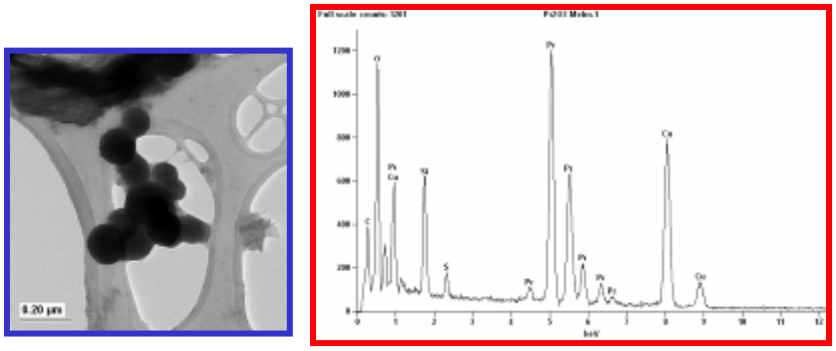

Figure 44. Pr_2O_3 nanoparticles were approximately 200 nm in size. The background of this particular image is a lacey carbon grid. The particles are agglomerated; however, separate particles can still be identified. The EDS spectrum identifies Pr, O, C, and Cu. The C and Cu peaks are a result of the TEM grid the samples were placed on.

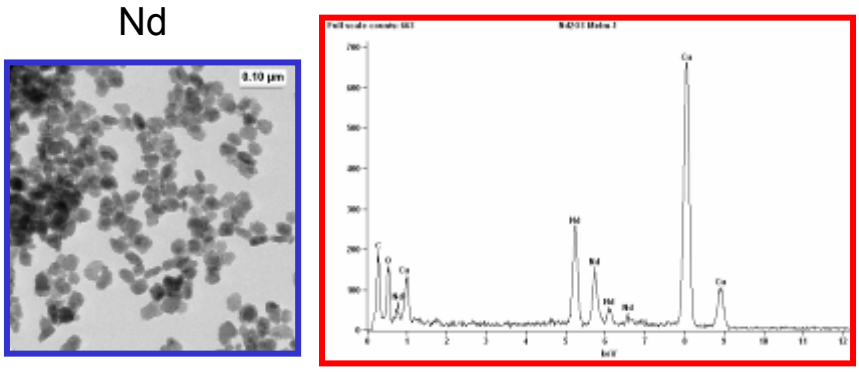

Figure 45. Characterization of Nd_2O_3 nanoparticles. The particles are monodispersed and separate particles about 40 nm in size are easily identifiable. The EDS spectrum identifies Nd, O, C, and Cu. The C and Cu peaks are a result of the TEM grid the samples were placed on.

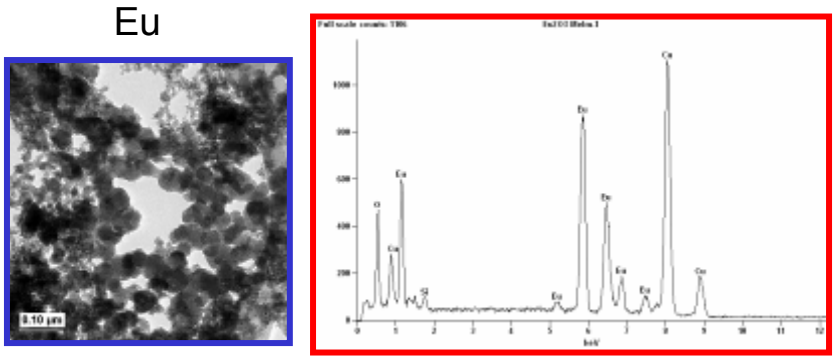

Figure 46. Characterization of Eu_2O_3 nanoparticles. The particles are somewhat agglomerated; however, separate particles about 20 nm in size can still be identified. The EDS spectrum identifies Eu, O, C, and Cu. The C and Cu peaks are a result of the TEM grid the samples were placed on.

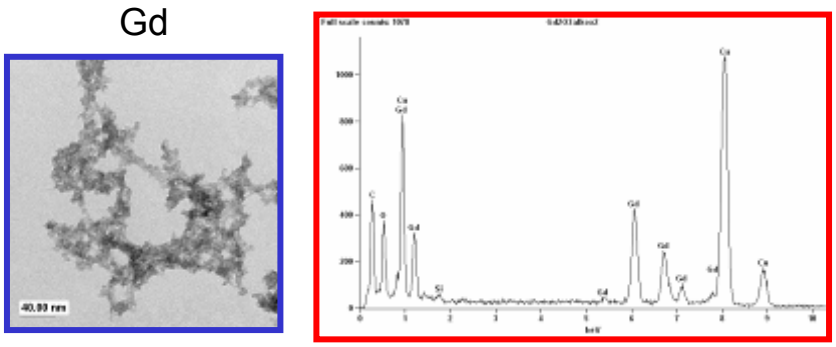

Figure 47. Gd_2O_3 nanoparticles were approximately 10 nm in size. The particles are agglomerated, however, separate particles can still be identified. The EDS spectrum identifies Gd, O, C, and Cu. The C and Cu peaks are a result of the TEM grid the samples were placed on.

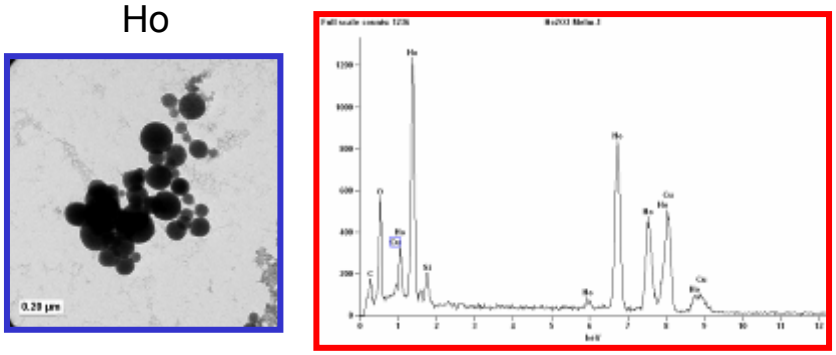

Figure 48. Characterization of Ho_2O_3 nanoparticles. The particles are well-dispersed and separate particles about 90 nm in size can be identified. The particles are spherical in shape, unlike some of the images, which leads us to further explore cause and effect of morphology. The EDS spectrum identifies Ho, O, C, and Cu. The C and Cu peaks are a result of the TEM grid the samples were placed on.

Using solution routes to prepare Ln_2O_3 nanoparticles proved to be successful in that for the majority of prior cases presented, the particles were spherical in shaped and easily identifiable. Shorter growth periods may be attempted to decrease particle size according to the La Mer Growth Principle. Smaller particle size would also contribute to increased photoactivity if the same principle applied to Au is applied here. Results in the literature prove that Au becomes catalytically active at the nano scale.

5.8 Synthesis of Lanthanide Oxide Materials using the Microemulsion Prep

Another method used for nanoparticle synthesis was the microemulsion prep where the commercially available $Ln(NO_2)_3$ (Ln = Eu, Gd, Ho) was dissolved in H_20/28% $NH_3 \cdot H_2O$ and added to a solution of CTAB/cyclohexane/1-hexanol solution followed by stirring for 30

minutes. The solvent was then removed and the resultant nanoparticles were calcined at 600 °C for 2 hrs. The nanoparticles were then characterized using TEM by taking an aliquot of the desired precipitate suspended in hexanes and placing it directly onto a carbon-coated copper TEM grid. The TEM and EDS results of the synthesis using the microemulsion prep described above are shown in Figs. 49-51.

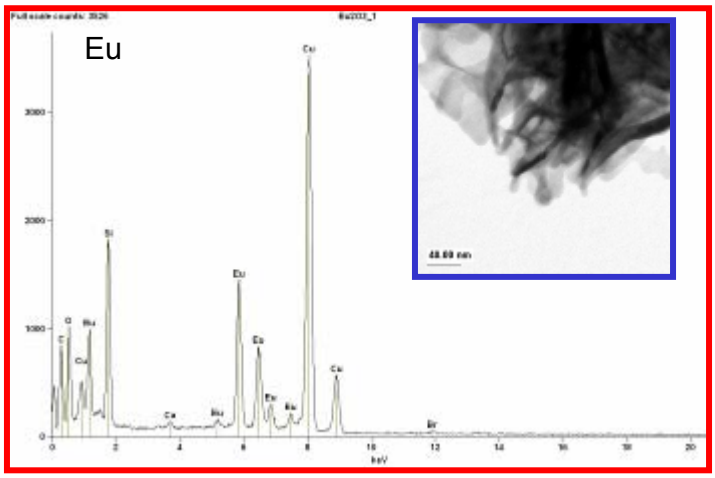

Figure 49. Europium oxide material synthesized using a microemulsion prep. The image shows a claw-like material that doesn't have much of a definite morphology. The scale bar on this image is that of 40nm. The EDS reflects peaks of Eu, O, C, and Cu. The C and Cu are a result of the TEM grid.

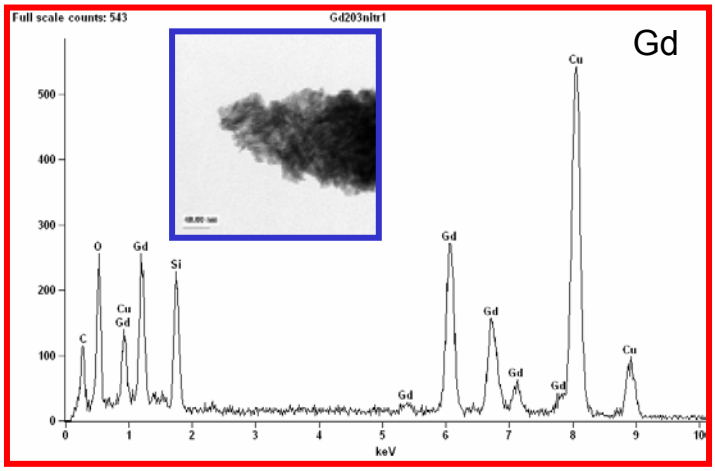

Figure 50. Gadolinium oxide material synthesized using a microemulsion prep. The image shows a mass of stick-like material held together by a glue that we believe to be silicon, as depicted in the EDS. The scale bar on this image is that of 40nm. The EDS reflects peaks of Gd, O, C, Si, and Cu. The C and Cu are a result of the TEM grid.

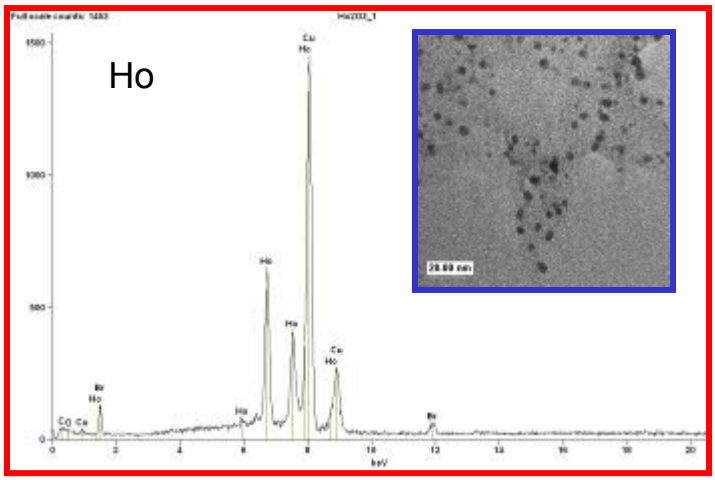

Figure 51. A holmium oxide material synthesized using a microemulsion prep. The image shows monodispersed spheres that are approximately 8nm in size that leads us to further explore cause and effect of morphology. The EDS reflects peaks of Ho, O, C, and Cu. The C and Cu are a result of the TEM grid.

5.9. Gadolinium-Doped TiO_2

The purpose of this part of the project was to treat the surface of TiO_2 nanoparticles with lanthanide metal nanoparticles in an attempt to partially reduce, or otherwise alter, the surface of the TiO_2 and observe the effect on photocatalysis. All reactions/manipulations were carried out in an argon atmosphere unless otherwise noted. All glassware was oven-dried overnight at 140 °C and transferred hot into the drybox. **SAFETY NOTES**: *Pure lanthanide metal nanoparticles are pyrophoric when exposed to air. Aqua regia is a strong acid and oxidizing agent.*

15-crown-5 (Aldrich) was dried overnight with activated molecular sieves (4A) and distilled (88 – 95 °C, 0.01 torr). (Aldrich catalog bp: 100 – 135 deg C, 0.2 torr.) Gadolinium (III) chloride (Aldrich, anhydrous) was used without further purification. THF was purified by stirring overnight with NaK/benzophenone followed by refluxing for 3.5 h, then distilled.

All glassware contacting the alkalide was thoroughly cleaned with detergent and rinsed well This was followed by filling with aqua regia and heating to boiling with a heat gun. The aqua regia-filled glassware was allowed to sit overnight. The aqua regia was emptied and the glassware thoroughly rinsed with water then thoroughly rinsed with (18 megaohm) water.

In the drybox, NaK (1:1 molar ratio, 0.232 g, 3.74 mmol) was added to a 50 mL (14/20) erlenmeyer flask. THF (ca. 40 mL) was added along with a small glass stirbar. This flask was capped with a glass stopper and put into the drybox freezer at around –35 deg C and stirred for 3 h by placing the stirplate under the freezer, outside the drybox. The flask was then removed from the freezer and 15-crown-5 (1.62 g, 7.38 mmol) was quickly added. After addition, the flask was immediately returned to the freezer and the reaction mixture stirred overnight. (Within about 1 min of crown addition, the mixture turned an opaque blue.)

In the drybox, a 250 (24/40) Erlenmeyer flask was charged with gadolinium (III) chloride (0.552 g, 2.09 mmol) and THF (ca. 200 mL). The flask was capped with a glass

stopper, and the salt was dissolved by stirring for 30 min. This flask was put into the drybox freezer, and stirring was continued for 2.5 h. The alkalide was then added to the stirred salt solution through a cold C frit in one portion. The alkalide flask was rinsed with 2 x 10 mL cold THF and the rinsing added through the frit as well. Stirring was continued for 15 min. The reaction mixture was then kept in the freezer for ca. 3h during which time the precipitate settled substantially. Enough of the solids had settled so about 225 mL of the supernatant could be syringed off. The remaining solids were separated by centrifugation in the drybox. The solids in all six tubes were washed into a Schlenk flask with a total of about 10 mL THF, and the solvent was pumped off. The solids were transferred into a 10 mL (14/20) flask and the flask stoppered with a slightly greased glass stopper.

Yield: 0.698 g (33 %) of a black, free-flowing powder [“Gd^0 mix”] based on

$$2\ GdCl_3 + 3\ K^+(15\text{-crown-}5)_2Na^- \rightarrow 2\ Gd^0 + 3\ K^+(15\text{-crown-}5)_2Cl^- + 3\ NaCl$$

Ideally, this should be 15% Gd by mass. No further purification was carried out. Removal of the salts is accomplished by aqueous workup after reaction with TiO_2.

Additionally, The TiO_2 nanopowder (Aldrich, catalog #637254, anatase) was oven-dried at 105 °C for 3 h. In a typical preparation, in the drybox, a 25 mL (14/20) rb flask was charged with “Gd^0 mix” (5 mg), a small stir bar, and TiO_2 (50 mg). THF (10 – 15 mL) was then added. The flask was capped with a glass stopper (ungreased), and the reaction mixture was stirred vigorously overnight. The flask was then removed from the drybox and *slowly* exposed to air while stirring. The solids were separated by centrifugation and washed with 2 x 2 mL of THF followed by washing with 4 x 1 mL deionized water . The sample was oven-dried at 110 °C overnight. Three other reactions with varying amounts of “Gd^0 mix” (11, 28, and 55 mg) were conducted in a similar manner. For the lower (5 and 11 mg) dopings, the reaction mixtures turned a homogeneous white within 30 minutes of THF addition, and reaction workup was identical. For the 28 mg doping, the mixture turned a light grey. For the 55 mg doping, the mixture lightened only slightly to a dark grey throughout. These were exposed to air slowly until all dark material disappeared. In both of these reactions, some yellowish material settled out; only the suspended white material was pipetted out for purification. Yield: 40 – 45 mg in all cases.

The diffuse reflectance plots for the Gd doped samples are presented in Figure 52, and indicate that the presence of the Gd induces a blue-shift in the bandgap of the doped material that is observed to be dependent on the amount of Gd utilized.

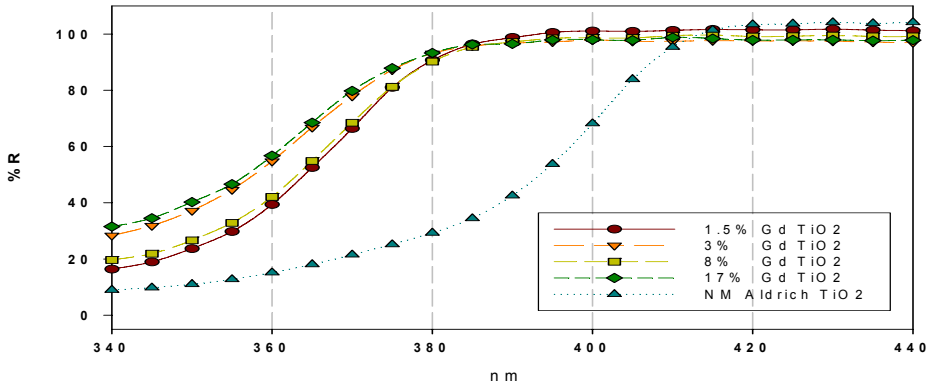

Figure 52. Diffuse reflectance plots of the Gd doped TiO_2

The photocatalytic efficiency of the Gd doped materials is shown in Figure 53 as a function of wt% Gd after 45 minutes of exposure. The presence of the Gd produces a very active photocatalyst at 350 nm, with the 1.5% Gd being the most efficient of those analyzed.

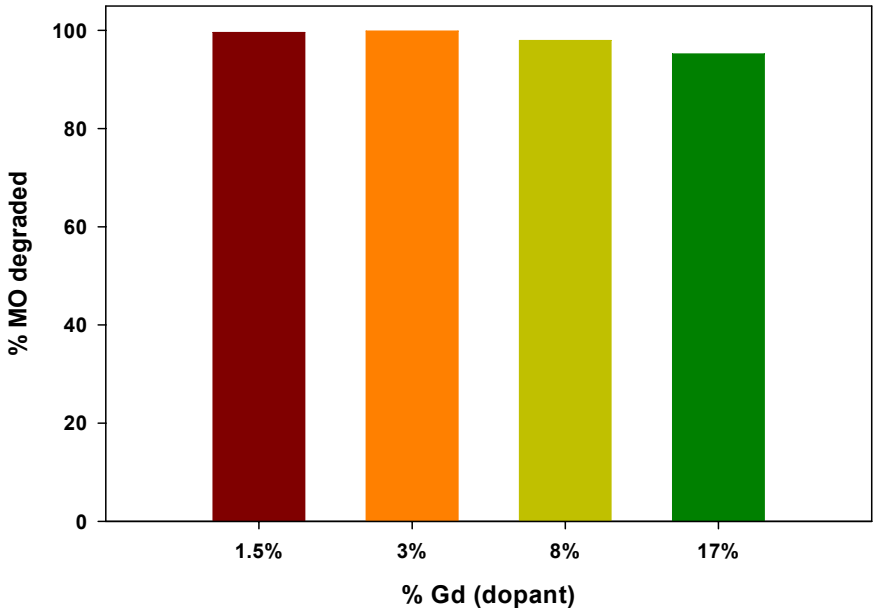

Figure 53. Photocatalytic efficiency bar graph of the Gd doped materials as a function of wt% Gd. The plots were generated from data obtained after 45 minutes of exposure at 350 nm.

5.10 Synthesis of LnOCl particles using a Parr Digestion Bomb Prep

The TEM and EDS results of the LnOCl synthesis using the Parr digestion bomb described above are shown in Figs. 54-55.

Pr

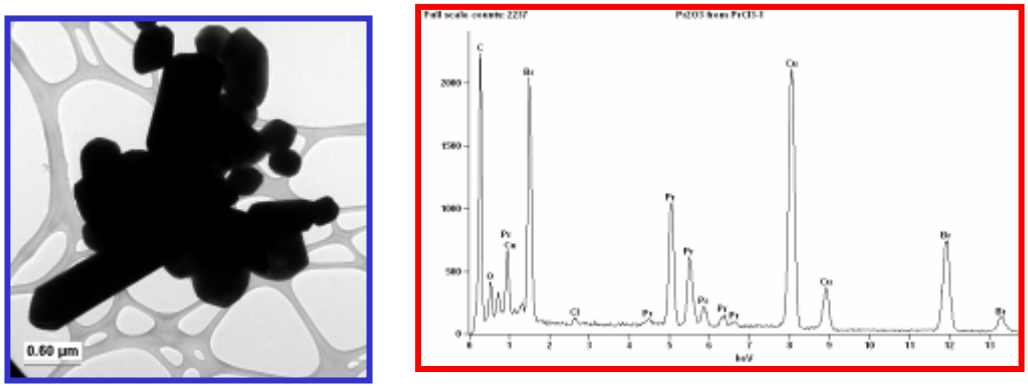

Figure 54. Hexagonal-shaped PrOCl crystals. The background of this particular image is that of a lacey carbon grid. The particles, synthesized using a high temperature and pressure Parr Digestion Bomb technique, range f from 600nm-1.2 microns in size. The EDS spectrum indicates that Pr, O, Cl, C, and Cu are present in the sample. The C and Cu are a result of the TEM grid.

Eu

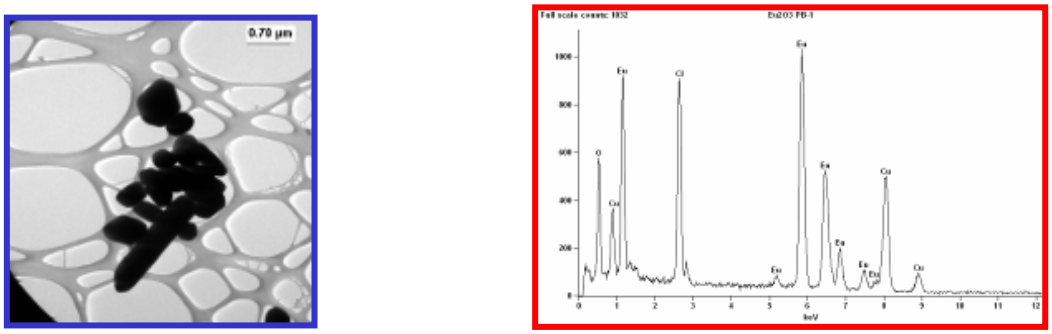

Figure 55. Hexagonal-shaped EuOCl crystals. The background of this particular image is that of a lacey carbon grid. The particles, synthesized using a high temperature and pressure Parr Digestion Bomb technique, range from 700 nm-1.4 microns in size. The EDS spectrum indicates that Eu, O, Cl, C, and Cu are present in the sample. The C and Cu are a result of the TEM grid.

This synthesis route was used in an attempt to make Ln_2O_3 nanoparticles as well; however, we found that using $LnCl_3$ as a precursor yields LnOCl nanocrystals ranging from 600 nm – 1.4 microns in size. The resultant particles in turn are not good dopants or remediation materials because of the presence of the halide. Therefore, the study of using $LnCl_3$ as a precursor to Ln_2O_3 was truncated at this juncture.

5.11 Doping Ti compounds with Lanthanide Alkoxides using Parr Digestion Bomb

A high temperature and pressure Parr digestion bomb was used for nanoparticle synthesis. TiO_2, $Ln(OR)_3$ and $Ti(OR)_4$ were dissolved in benzyl alcohol and heated at 200 °C for 48 hrs. The nanoparticles were then characterized using TEM by taking an aliquot of the desired precipitate suspended in hexanes and placing it directly onto a carbon-coated copper TEM grid The aliquot was then allowed to dry. The resultant particles were studied using a Philips CM 30 TEM operating at 300-kV accelerating voltage. The nanparticles were also characterized by powder X-ray diffraction (XRD). Finally, the $Ln(OR)_3$ (Ln = Pr, Yb, Tb) materials previously prepared were used in the Parr digestion bomb prep to dope the anatase TiO_2. The TEM and EDS results are given in Figs. 56-58.

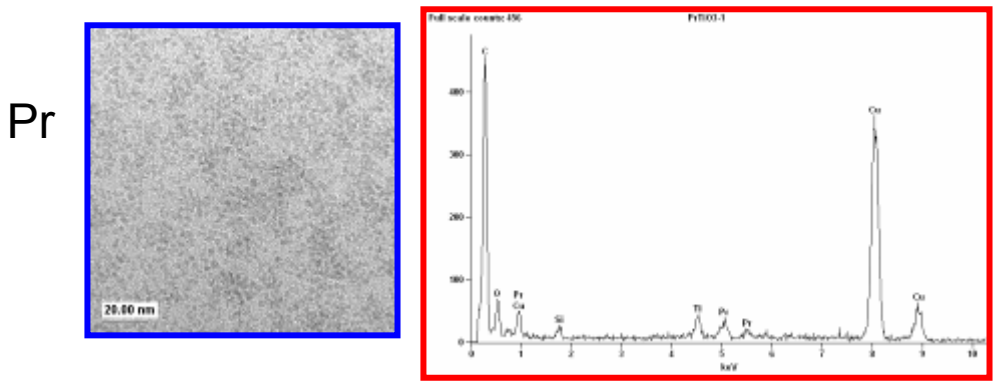

Figure 56. Nanoparticles of Pr-doped TiO_2. The particles, prepared in a high temperature and pressure Parr Digestion Bomb technique, are spherical in shape and approximately 2nm in size. The EDS shows Pr, O, Ti, C, and Cu present in the sample. The C and Cu are a result of the TEM grid.

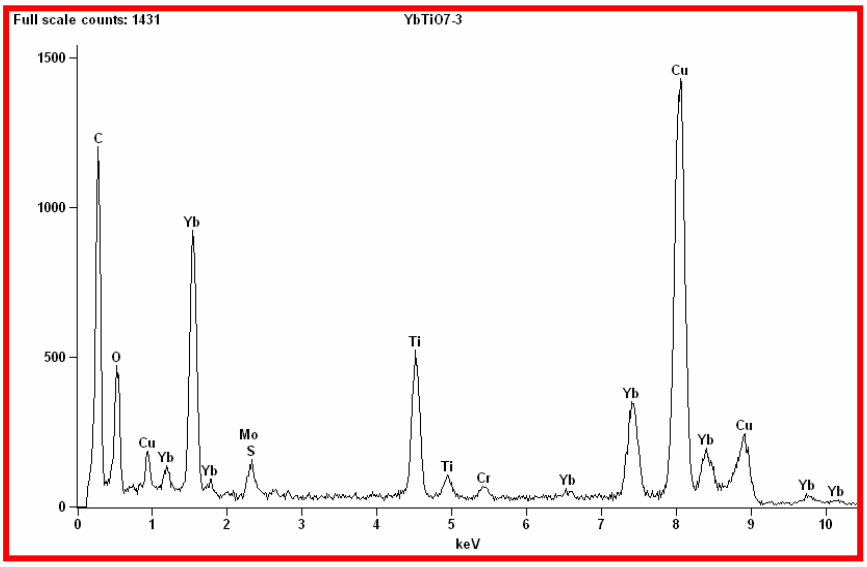

Figure 57. Nanoparticles of Yb-doped TiO_2. The particles, prepared in a high temperature and pressure Parr Digestion Bomb technique, are spherical in shape and approximately 2nm in size. The EDS shows Yb, O, Ti, C, and Cu present in the sample. The C and Cu are a result of the TEM grid.

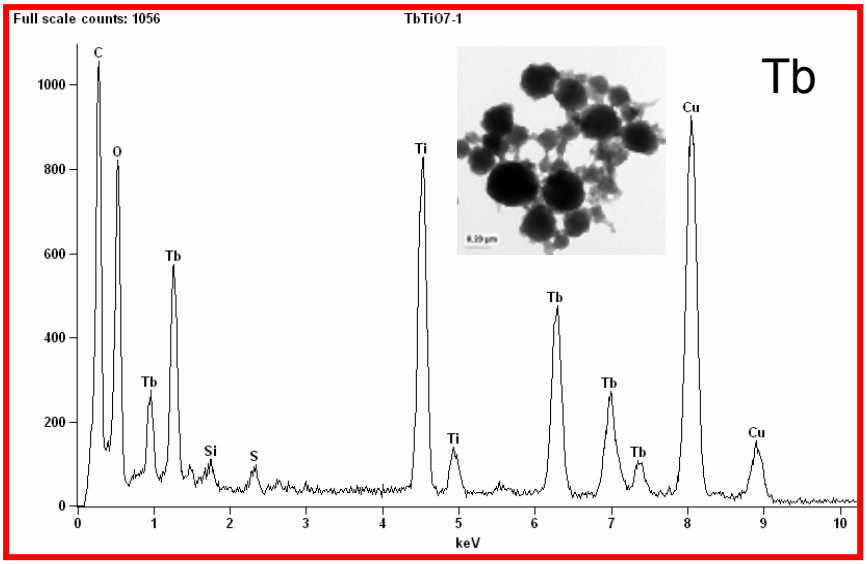

Figure 58. Nanoparticles of Tb-doped TiO_2. The particles, prepared in a high temperature and pressure Parr Digestion Bomb technique, are spherical in shape and approximately 200 nm in size. The EDS shows Tb, O, Ti, C, and Cu present in the sample. The C and Cu are a result of the TEM grid.

The previously synthesized alkoxides were used to dope the Ti compounds in an effort to increase photocatalytic activity of our materials. We found this was not the case after testing these doped materials. Typical photocatalytic efficiencies as a function of wavelength for the Pr doped TiO2 are presented in Figure 59, and indicate that the material is very weakly catalytic when compared to the reference material. Similar results were obtained for all of the doped materials (Tb, Sc, and Yb) synthesized using this technique.

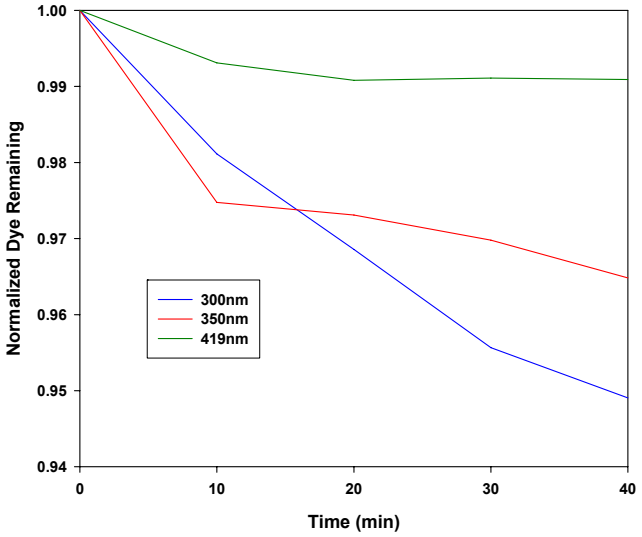

Figure 59. Photocatalytic efficiency of Pr doped TiO2 as a function of wavelength

Further studies may include preparing a single-source precursor to use in the high temperature and pressure technique. In addition, the single-source precursor may contribute to size reduction of the resultant particles. A decrease in size distribution may increase photocatalytic activity being as this process is a surface area dominated phenomena.

5.12 Ammonia-Based Lanthanide Doping of TiO_2

This doping method chosen is based on a literature procedure in which europium or ytterbium is dissolved in liquid ammonia and deposited on titania (by evaporation of the ammonia) to study the *catalysis of the lanthanide metal*. The lanthanides in the literature procedure were deposited in high amounts (5 – 15 % by mass). In the present study, we use smaller amounts of the lanthanides, since we are concerned with *catalysis by titania*. Initially, a relatively large (ca. 5%) doping was used to ensure observation of the lanthanide metal by EDS analysis. Afterwards, more "useful" levels (< 3%) were used.

In a typical procedure, a 50-mL three-neck rb flask equipped with a stir bar, solids addition funnel, dry-ice condenser, and inlet tube was charged with titania powder in the drybox. The lanthanide metal was weighed and transferred to the addition funnel. The apparatus was removed from the dry box and placed in a dry-ice isopropanol bath under an argon atmosphere. About 20 mL of anhydrous ammonia was condensed into the flask. The lanthanide metal was then added in one portion to the stirred ammonia suspension. Upon addition, the solution became very dark blue, almost black, in color. After about two hours, the color lightened and stabilized to a pale blue. The dry ice bath was then removed to allow the ammonia to evaporate. The product was stored in the dry box. TEM and EDS analysis were performed on this sample as well as heated samples.

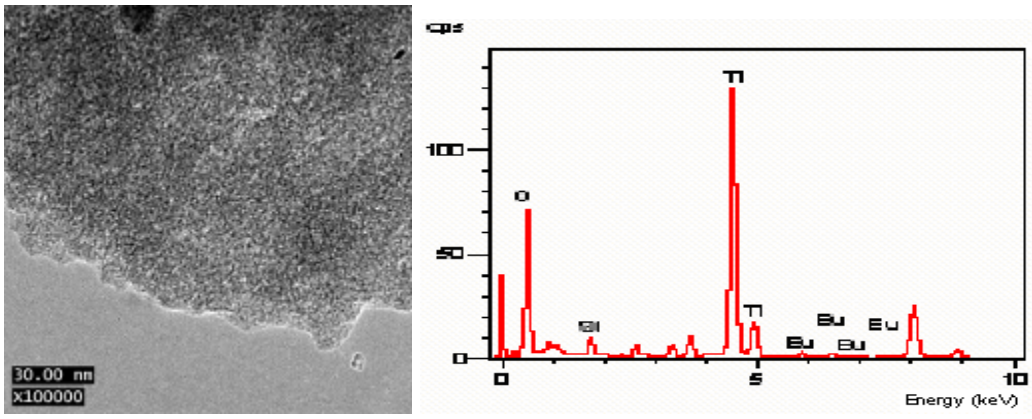

Figure 60. TEM image and EDS spectrum of 3% Eu doped aggregated TiO_2 utilizing ammonia-based approach.

TEM images show that, after Eu doping, TiO_2 is still aggregated, while EDS analysis confirmed the composition of Ti and Eu (Figure 60). Ideally, the lanthanide is initially deposited as $Ln(NH_2)_2$ or $Ln(NH_2)_3$. Heating removes ammonia first, then hydrogen gas, to finally give the lanthanide metal nitride (equation 1). The doped powder was heated under vacuum at 212°C for 2 hours. Another sample was heated at 318°C for 2 hours.

$$Ln(NH_2)_2 \text{ or } Ln(NH_2)_3 \xrightarrow[\sim 200°C]{-NH_3} Ln(NH) \xrightarrow[\sim 300°C]{-1/2\ H_2} LnN \quad (Ln = Eu \text{ or } Yb) \qquad (1)$$

TEM images of the 212°C-heated sample show that the crystals begin to break up (Figure 61 left). After heating at 318°C, the aggregated particles become completely dispersed (Figure 61 right), although the powder still did not suspend well in water. A diffraction pattern was obtained, showing the crystallinity of the 318°C-heated powder (Figure 62).

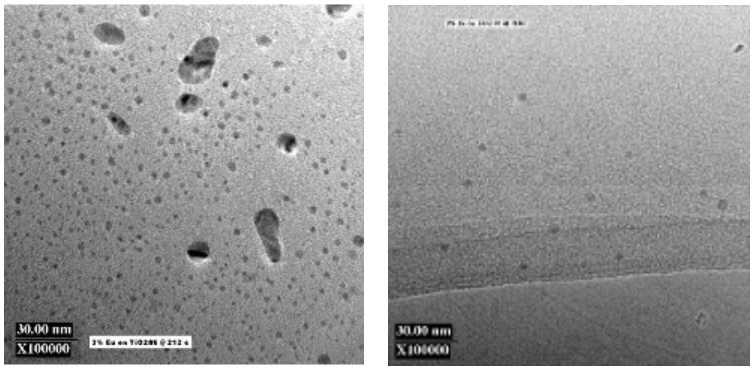

Figure 61. Left, TEM image of 3% Eu doped TiO_2 heated at 212°C. Right, TEM image of 3% Eu doped TiO_2 heated at 318°C. As the temperature increases, the aggregated particles begin to break up into smaller particles.

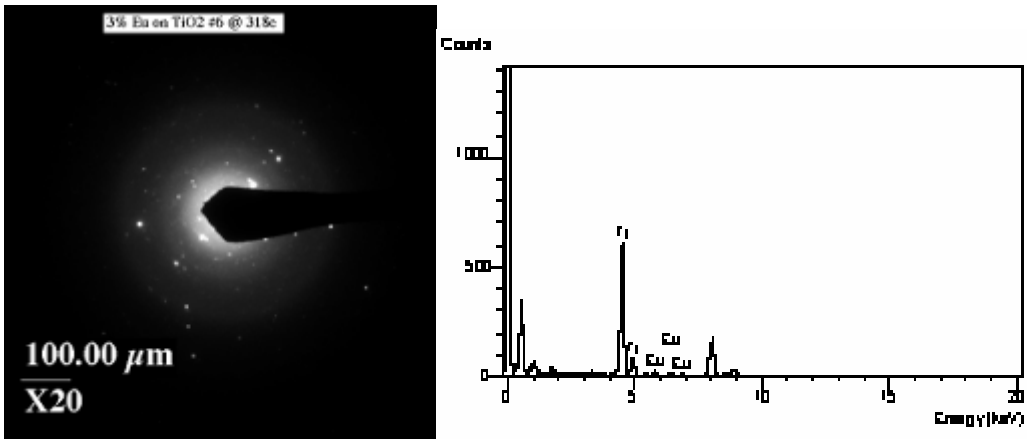

Figure 62. Left, diffraction pattern of 3% Eu doped TiO_2 heated at 318°C. Right, EDS spectrum confirms no change in the sample composition.

The undoped TiO_2 was heated under similar conditions. However, the crystal sizes were not uniform. This may be due to the technique used. Since the heating was performed in a round bottom flask under vacuum in a sand bath, it was not possible to heat the sample uniformly. The lattice of a particle was observed at 400K magnification, showing approximately 7nm in size (Figure 63).

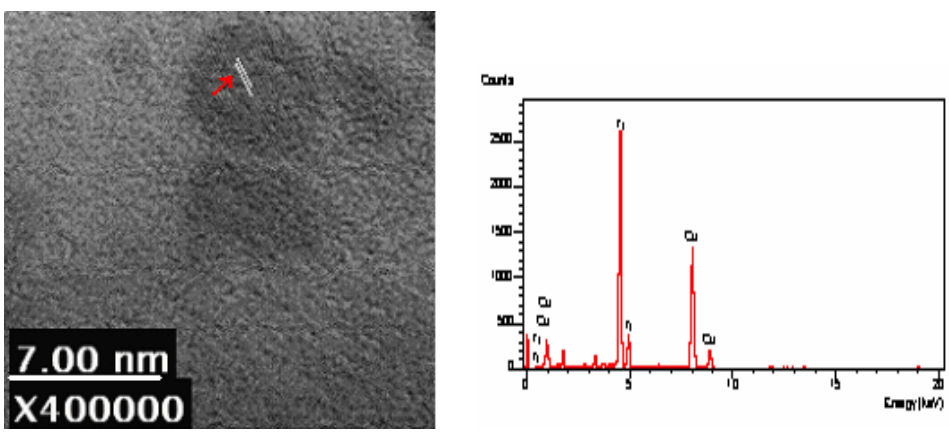

Figure 63. TEM image and EDS spectrum of TiO_2 heated at 318°C. Lattice fringes, shown by the red arrow, are observed at 400K magnification.

The Eu and Yb dopants had a decided impact on the bandgap of the materials as shown in Figure 64. All of the samples exhibit a red-shift to the visible spectrum as compared to the undoped TiO_2. The most dramatic red-shift for the Eu dopants in Figure 64 (left) occurs at 3% Eu and processed at 318 ^{o}C, whereas for the Yb (Figure 64, right) the most dramatic shift occurs at 5% Yb processed at the same temperature value of 318 ^{o}C.

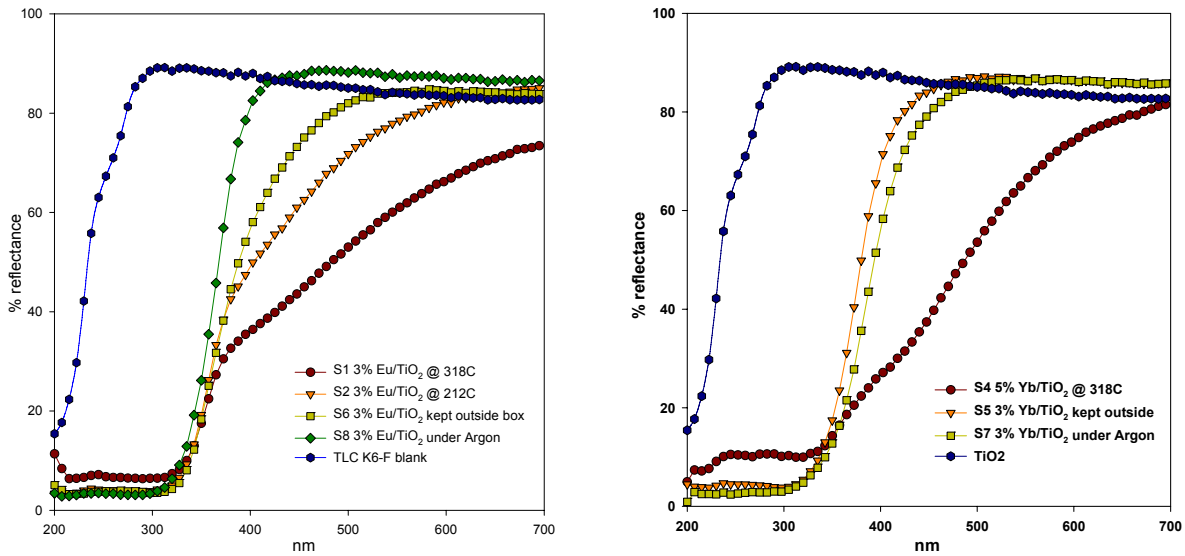

Figure 64. Diffuse reflectance plot of the Eu (left) and Yb (right) doped non-dispersed TiO_2 under various conditions and dopant levels.

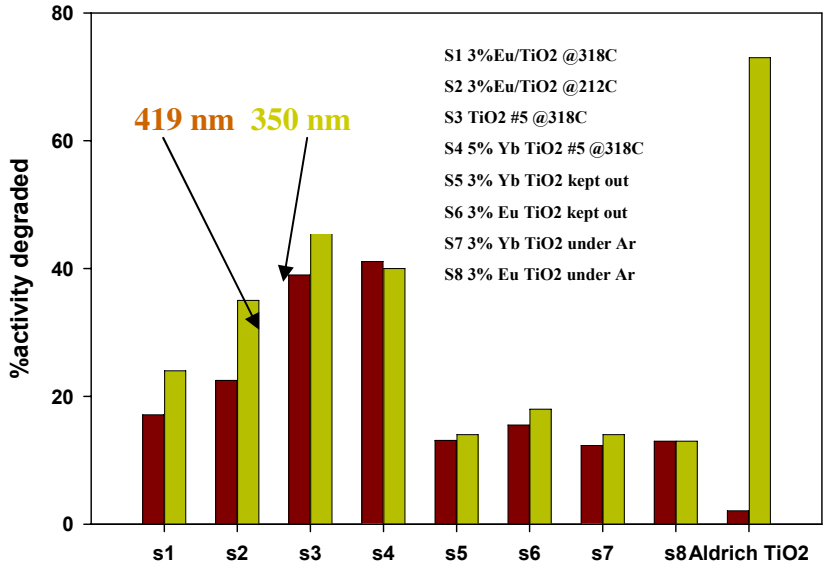

Figure 65. Comparison bar graph of the photocatalytic efficiency of various doped non-dispersed TiO_2 after 45 minutes of exposure at 350 and 419 nm exposures.

The photocatalytic efficiencies for the various Eu and Yb dopants of the non-dispersed TiO_2 are presented in Figure 65. Under exposure of 419 nm for 45 minutes, there are several doped systems that perform significantly better than the commercially available undoped TiO2. In contrast, with a 350 nm exposure for 45 minutes, the commercially available TiO2 outperforms any of the doped samples. The increased efficiency of these materials as photocatalysts under visible light illumination is attributed to the observed red-shift in the bandgaps as presented in Figure 64.

The next stage of this effort was to determine if an enhanced dispersion of the TiO_2 would yield enhanced doped photocatalysts. The dispersion of the TiO2 utilized the techniques presented previously in the section on undoped TiO_2. The dispersed TiO_2 was doped with Eu and Yb in the same fashion as previously described for the non-dispersed materials. Several papers in the literature have reported that very low metal doping levels (0.1% to 1%) may improve activity; hence, doping at lower total weight percent was also performed.

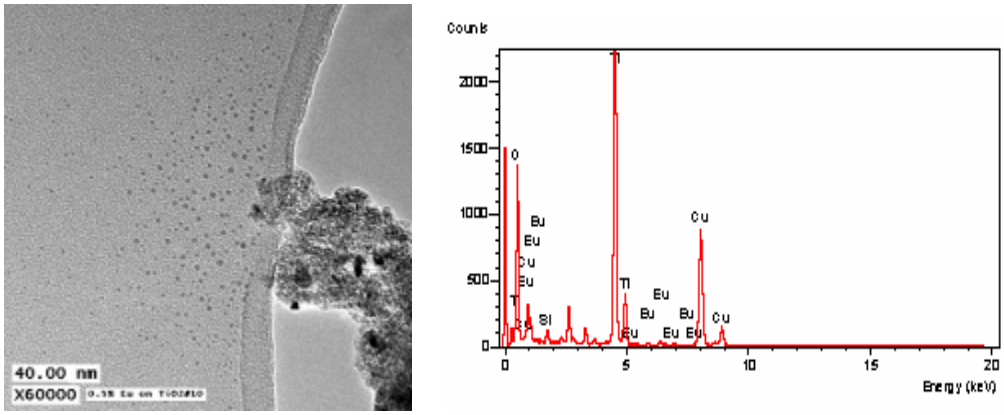

Figure 66. TEM image shows some loose TiO_2 particles after doping with 0.5% Eu. EDS spectrum confirms TiO_2 and Eu composition.

The newly made monodisperse TiO_2 was doped with Eu at a total weight percent of 0.5%. TEM images show there are loose TiO_2 particles after doping with Eu (Figure 66). The EDS spectrum also confirms the composition. After heating at 200°C, TEM images of the doped TiO_2 show loose (7 – 10 nm) particles that appear self-assembled (Figure 67).

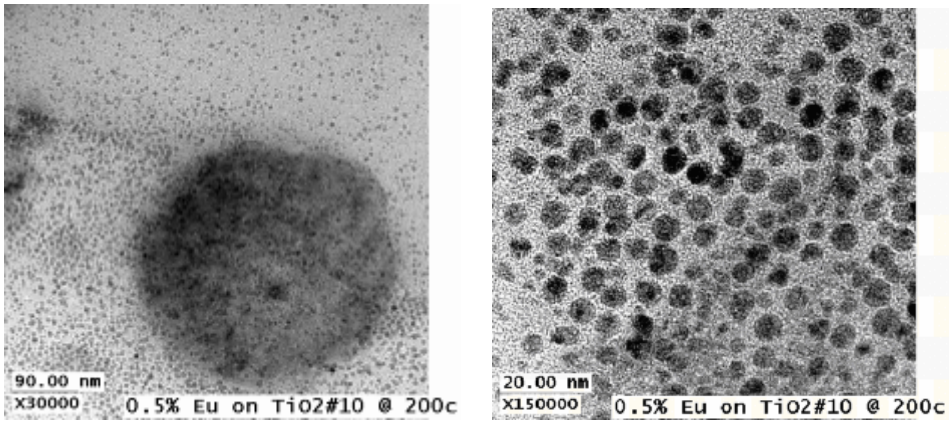

Figure 67. TEM images 0.5% Eu doped TiO_2 heated at 200°C showing loose particles.

It appears that at a higher heating temperature of 300°C, an agglomeration process begins to occur (Figure 68). EDS spectra were taken throughout the TEM imaging area to confirm consistent composition.

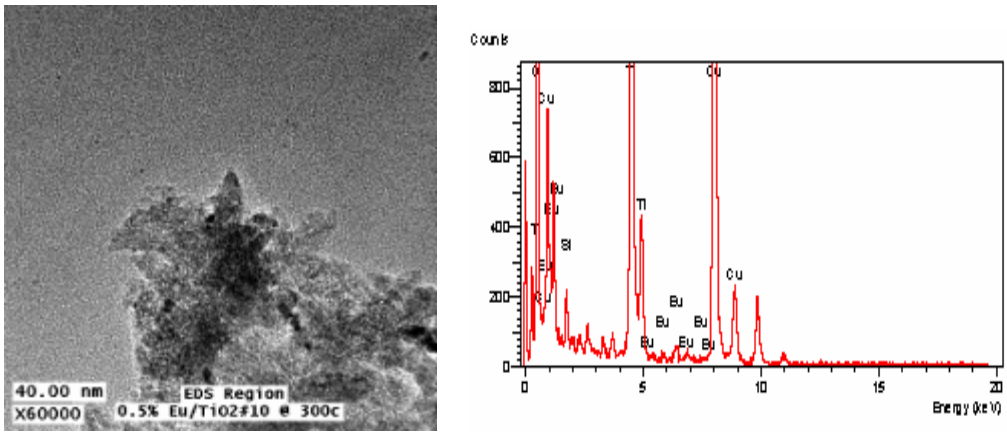

Figure 68. 0.5% Eu doped TiO_2 utilizing ammonia-based approach at 300°C shows that TiO_2 particles begin to agglomerate. EDS spectrum shows the composition has not changed.

This TiO_2 powder was also doped with ytterbium using the ammonia-based approach. Yb metal comes in large chunks and is very hard to handle in the dry box. It was determined that a 1% Yb doping was the minimum level that could be reliably measured. After doping, the samples were heated at 217°C, 320°C and 400°C. A temperature of 400°C was used the see if more agglomeration would take place. TEM images of 1% Yb-doped TiO_2 show loose TiO_2 particles (Figure 69).

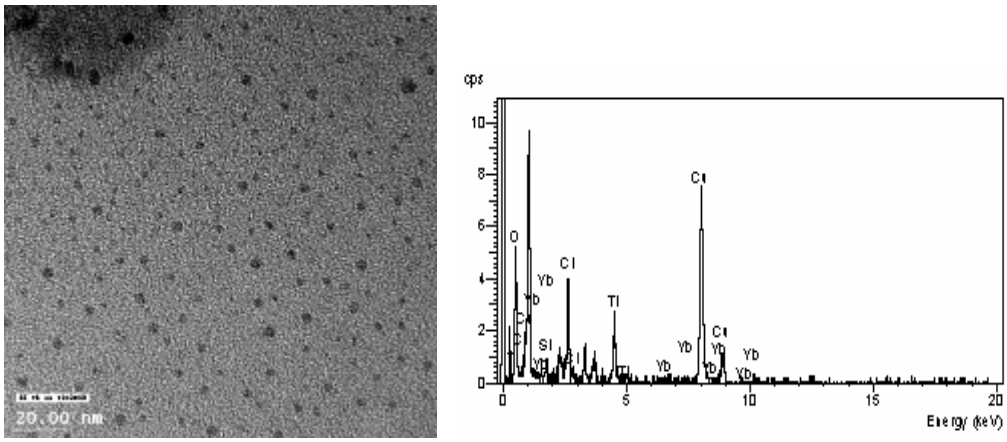

Figure 69. TEM images of 1% Yb doped TiO_2 with ammonia-based approach show loose TiO_2 particles in the sample prior to heating. EDS spectrum confirms the sample composition.

When the sample is heated to 217°C, the TEM image shows that agglomeration occurs (Figure 70 left). No dispersed TiO_2 particles can be observed throughout the TEM specimen; this is in contradiction to the 0.5% Eu doped TiO_2 heated at 200°C. After heating at 320°C, dispersed TiO_2 can be seen throughout the TEM specimen (Figure 70 right).

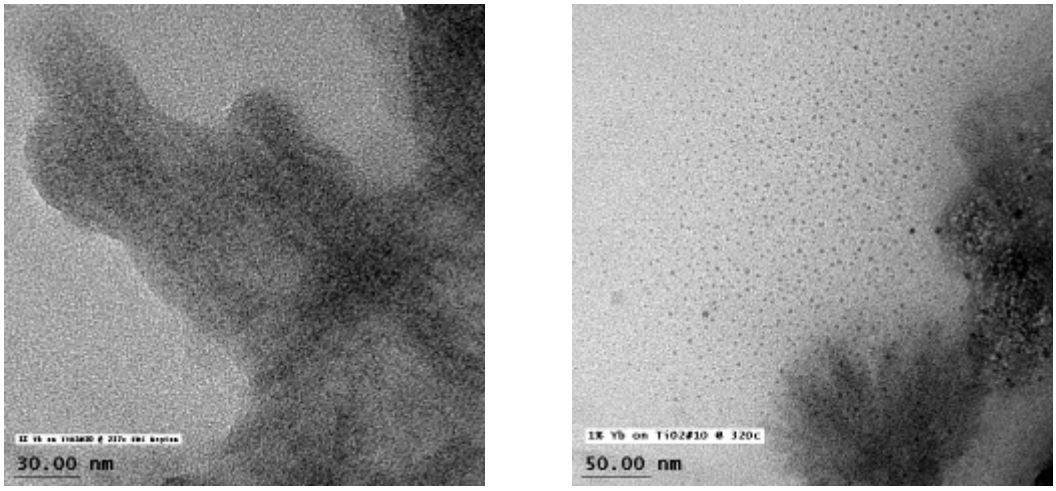

Figure 70. Left, TEM image shows 1% Yb doped TiO_2 sample at 217°C. Right, TEM image shows the sample at 320°C showing TiO_2 particles.

At 400°C, the TEM image shows the sample to be heavily agglomerated (Figure 71). The EDS spectrum of each sample was taken to ensure consistency in the composition. All locations of peaks are the same in each sample. Previously heated samples of 0.5% Eu doped TiO_2 at 300 °C also indicate that TiO_2 particles begin to agglomerate. The heated sample of 1% Yb doped TiO_2 appears to have the same behavior: as the temperature increases, more particles agglomerate, with the exception of the 217°C sample, which is inconsistent with the 0.5% Eu doped TiO_2 at the same temperature. It is inconclusive if there is any structural change or phase change below 400 °C.

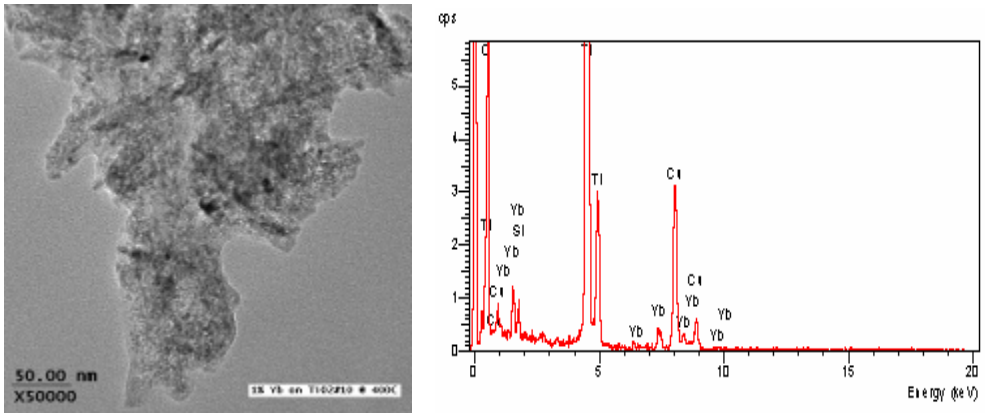

Figure 71. TEM image of the sample annealed at 400 °C shows heavy agglomeration, no TiO_2 particles were observed. EDS spectrum shows that heating at high temperature did not change the composition.

The results obtained from the photocatalytic degradation of methyl orange using these samples are shown in Figure 72. The illumination wavelength is 350 nm. These results indicate that the presence of the dopants, specifically the 0.5% Eu, afford photocatalysts that are as effective as the undoped and commercially available photocatalysts, but offer no compelling advantage over them. The presence of Yb at any level using this synthetic technique appears to have a consistently negative impact on the performance of the photocatalysts.

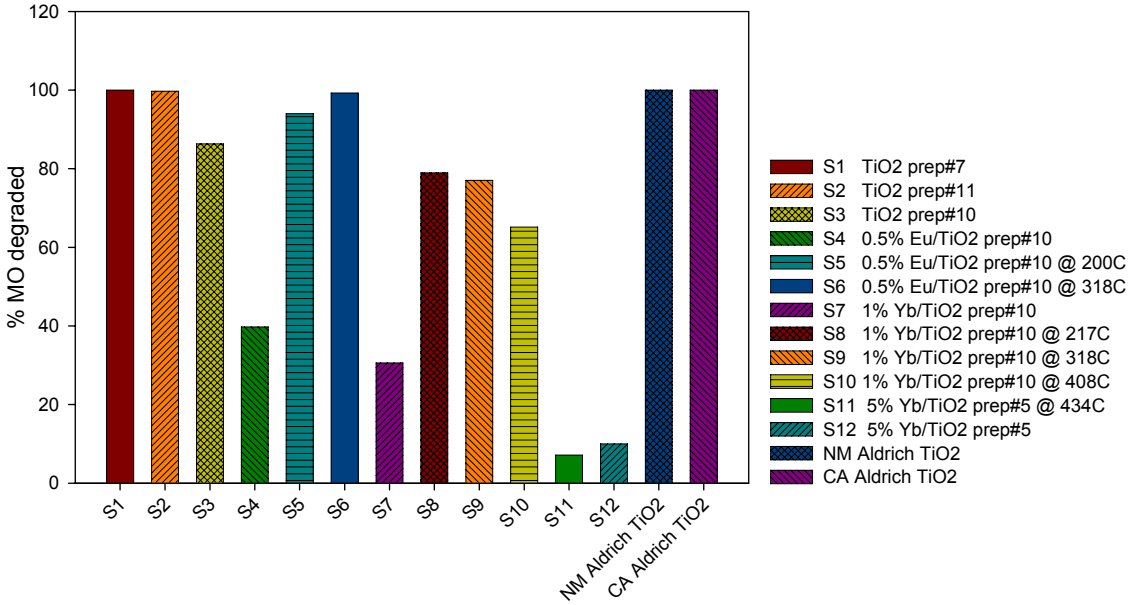

Figure 72. Bar graph comparison performance plot of the doped TiO2 samples with undoped and commercially available materials at 350 nm after 45 minutes of exposure.

6. Doping Commercially Available Nanocrystalline TiO_2

6.1 Introduction

Photocatalysis reactions have shown that Aldrich TiO_2 used as the standard is consistently one of the most active compounds tested. This material is available in several different crystal structures and particle sizes, and is relatively inexpensive This section of the report details our attempts to modify the commercially available material in an attempt to produce a cost-effective process amenable to rapid technology transfer.

6.2 Initial Results and Doping with Lanthanides

When the powder is added to deionized water, it agglomerates heavily and settles to the bottom of the container within a couple of days. XRD results have shown the phase composition to be 73.57% anatase with particle size of 58.21nm and 26.43% rutile with particle size of 47.68nm (Figure 73). The Aldrich (#634662) sample was dried at 105°C overnight prior to doping with Eu at 0.5%, 1.0%, 2.0% and 3.0%. Once the samples were doped, each was heated at 135°C, 221°C, and 300°C.

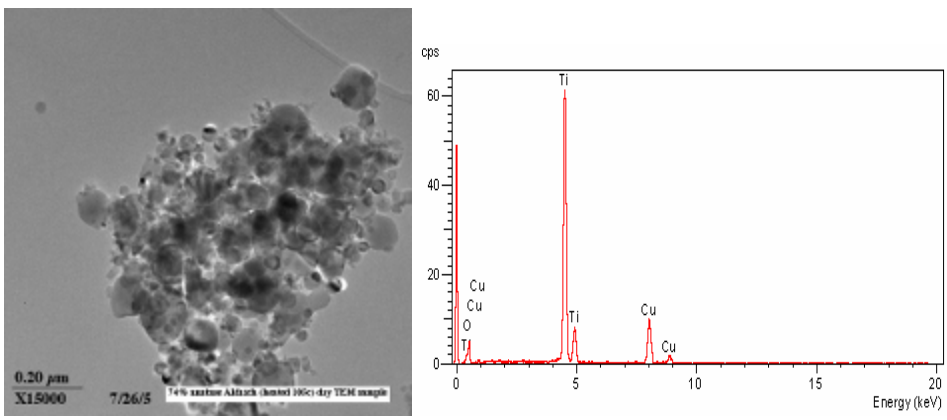

Figure 73. TEM image of the Aldrich TiO_2 (catalog# 634662) dry sample shows the large particles of mixed anatase and rutile phase. EDS spectrum shows the peaks of Ti and oxygen.

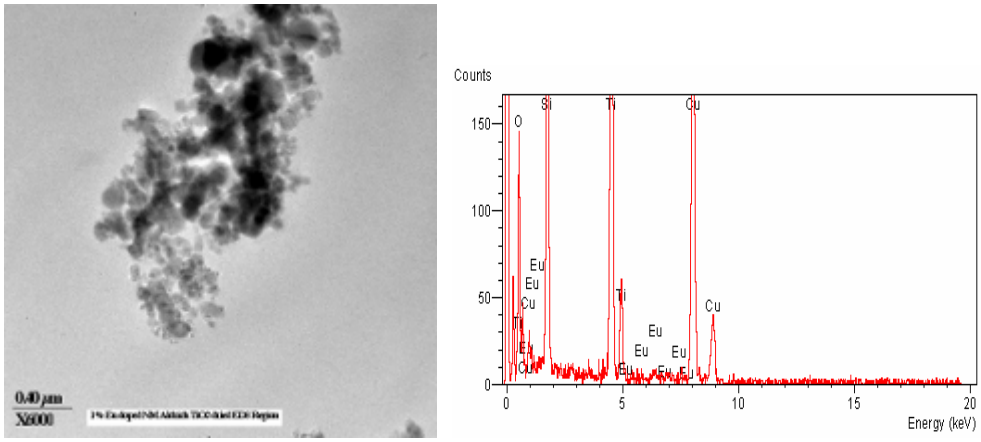

Figure 74. TEM images of 1% Eu doped agglomerated Aldrich TiO_2 particles dried overnight at 105°C. The EDS spectrum confirms the Eu dopant and TiO_2 composition.

The TEM image of the Aldrich TiO_2 (catalog #634662) doped with 1% Eu shows no physical change in the agglomeration of TiO_2 (Figure 74). The EDS spectrum confirms the composition of Eu and TiO_2. Heating the 1% Eu doped Aldrich TiO_2 (#634662) at 135°C yields a more dispersed sample (Figure 75). The sample was heated at this temperature because results obtained from photocatalytic studies suggested that TiO_2 heated at lower temperatures seems to be more active. TEM images show very little difference in particle size between the samples heated at 221°C (Figure 76 left) and 300°C (Figure 76 right). However, heating at these two temperatures may result in even smaller particles than samples heated at 135°C.

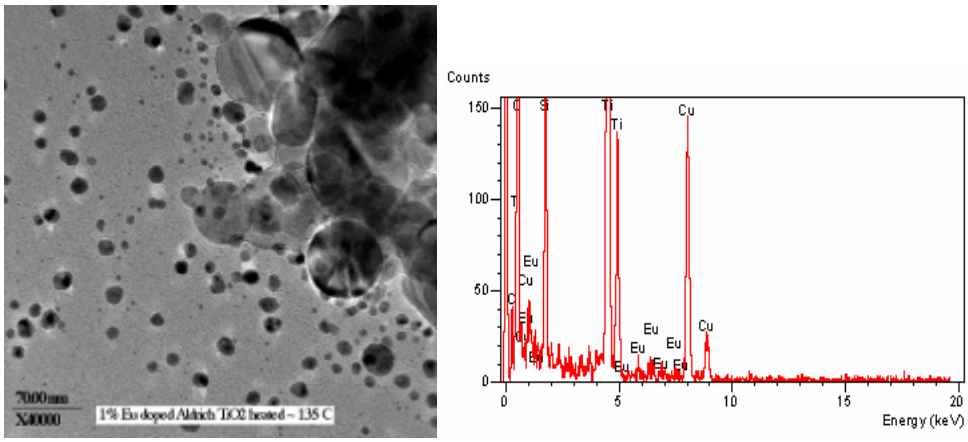

Figure 75. TEM images of 1% Eu doped agglomerated Aldrich TiO_2 at 135 °C. The particles appear to break up into smaller particles of approximately 30 nm. EDS spectrum show that there is no change in the composition of the sample.

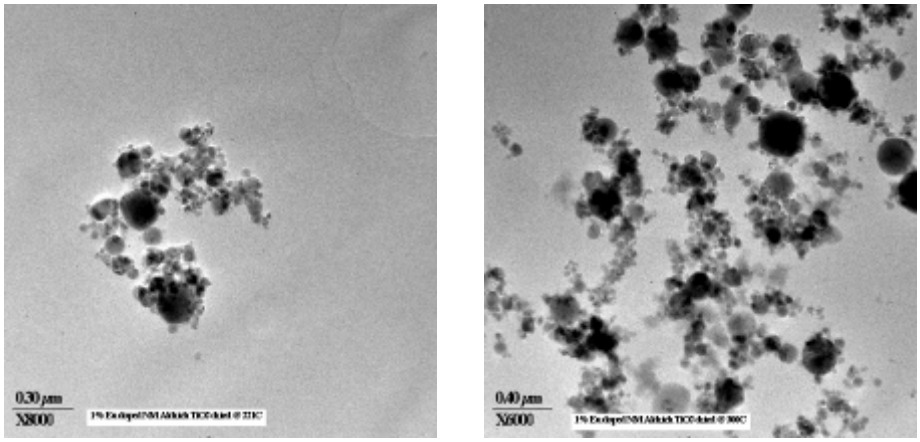

Figure 76. Left TEM image shows 1% Eu doped TiO_2 at 221 °C. Right TEM image shows the sample heated at 300 °C.

Diffuse reflectance and photocatalytic efficiency measurements for the 0.5 – 3.0% Eu doped commercially available nanocrystalline TiO_2 are presented in Figures 77-82. A complete list of the sample identifications utilized and the corresponding compositions is also presented in Table 1 for reference.

Table 1.
List of Sample IDs and Compositions for the Eu Doped Commercial Nanocrystalline Non-Dispersed TiO_2

Sample No.	Composition
JP1.82.1	0.5% $EuTiO_2$ Aldrich
JP1.84.1	0.5% $EuTiO_2$ Aldrich @ 135°C
JP1.84.2	0.5% $EuTiO_2$ Aldrich @ 223°C
JP1.84.3	0.5% $EuTiO_2$ Aldrich @ 310°C
JP1.82.2	1.0% $EuTiO_2$ Aldrich
JP1.84.4	1.0% $EuTiO_2$ Aldrich @ 135°C
JP1.84.5	1.0% $EuTiO_2$ Aldrich @ 221°C
JP1.84.6	1.0% $EuTiO_2$ Aldrich @ 309°C
JP1.82.3	2.0% $EuTiO_2$ Aldrich
JP1.84.7	2.0% $EuTiO_2$ Aldrich @ 135°C
JP1.84.8	2.0% $EuTiO_2$ Aldrich @ 220°C
JP1.84.9	2.0% $EuTiO_2$ Aldrich @ 300°C
JP1.82.4	3.0% $EuTiO_2$ Aldrich
JP1.84.10	3.0% $EuTiO_2$ Aldrich @ 140°C
JP1.84.11	3.0% $EuTiO_2$ Aldrich @ 221°C
JP1.84.12	3.0% $EuTiO_2$ Aldrich @ 317°C

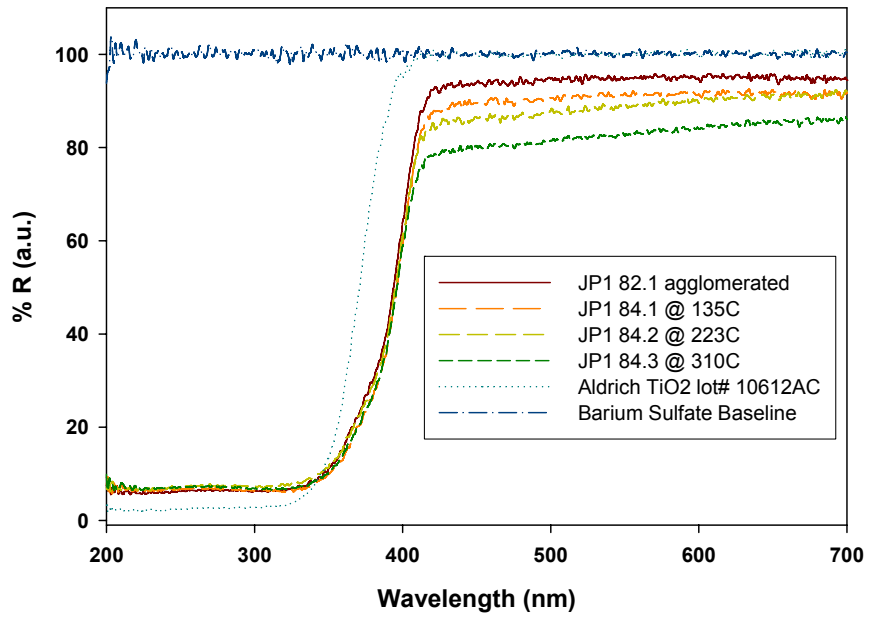

Figure 77. Diffuse reflectance plot of 0.5% Eu doped commercial non-dispersed TiO_2

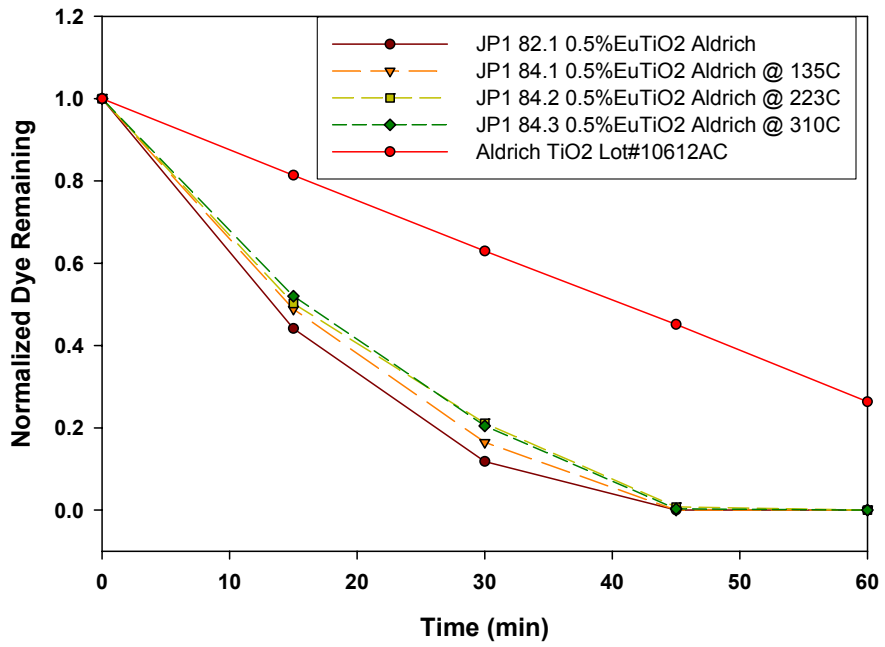

Figure 78. Photocatalytic activity of 0.5% Eu doped commercial non-dispersed TiO_2

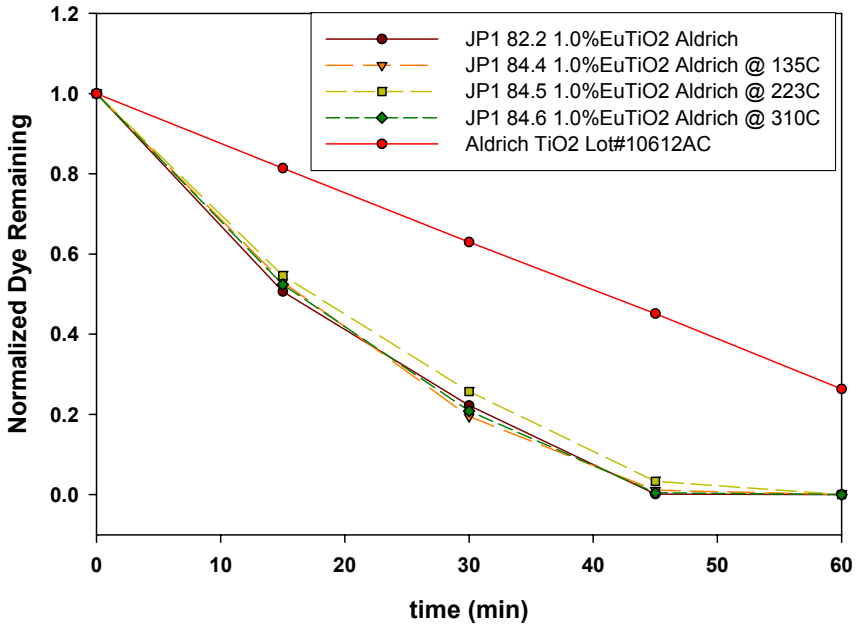

Figure 79. Photocatalytic activity of 1.0% Eu doped commercial non-dispersed TiO_2

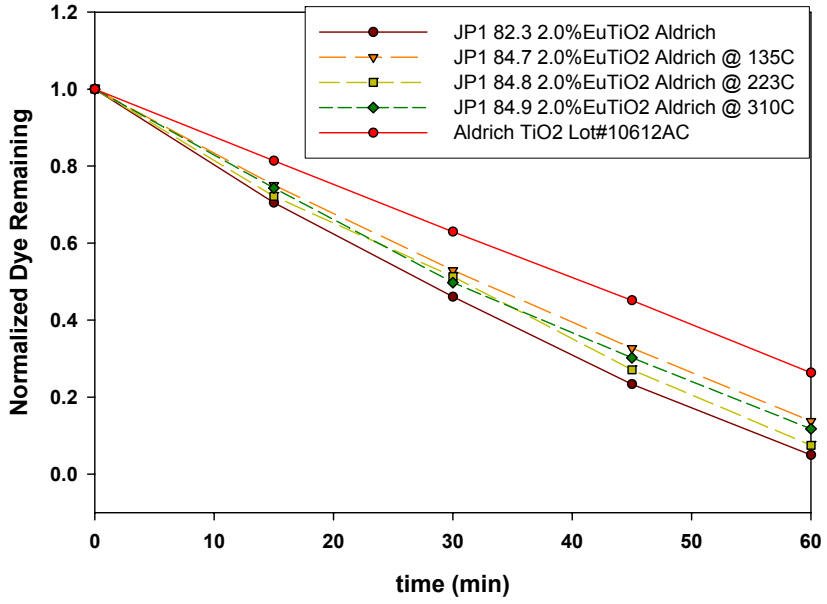

Figure 80. Photocatalytic activity of 2.0% Eu doped commercial non-dispersed TiO_2

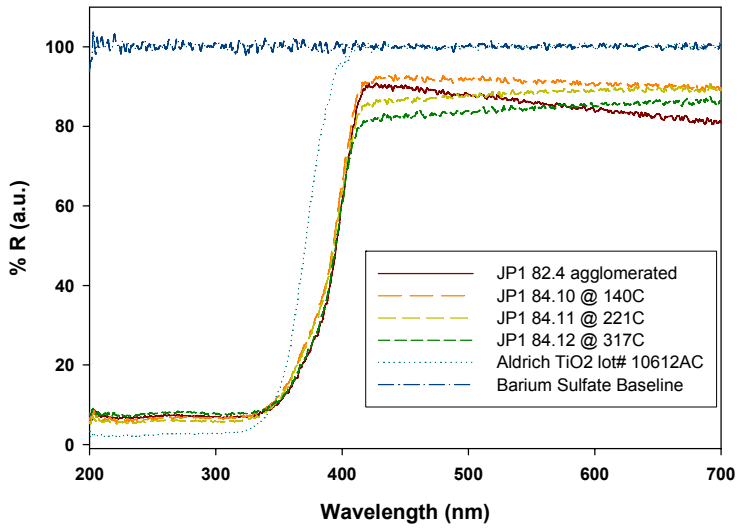

Figure 81. Diffuse reflectance plots of 3.0% Eu doped commercial non-dispersed TiO_2

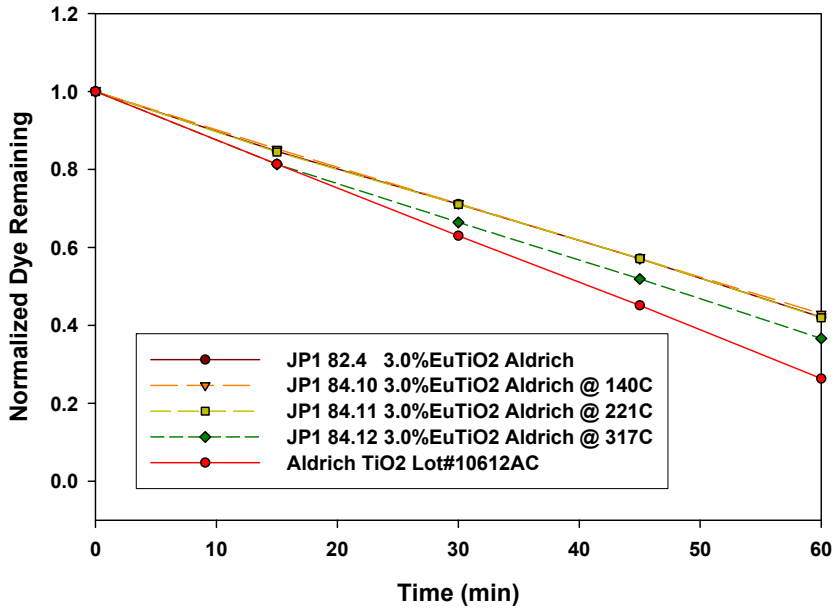

Figure 82. Photocatalytic activity of 3.0% Eu doped commercial non-dispersed TiO_2

The diffuse reflectance plots for the 0.5% Eu doped materials (Figure 77) indicates a slight red-shift in the observed bandgaps for all of the doped materials that appears to be invariant to the processing temperature. The photocatalytic efficiency of the doped materials is higher than that of the undoped material, as shown in Figure 78. After 45 minutes of exposure at 350 nm, roughly 100% of the dye is degraded in the vials containing the doped materials, whereas ~ 50% intact dye remains in the vials containing the reference starting material. As the amount of Eu dopant is increased, there is an observed decrease in the photocatalytic efficiencies of the materials. At 1% doping (Figure 79), there is still a marked improvement in photocatalytic efficiency of the doped samples as compared to the reference material. At 2% Eu (Figure 80), the doped materials (40% dye remaining after 45 minutes) still perform better than the undoped TiO2, but the margin of improvement has significantly dropped. At 3% Eu, the diffuse reflectance data (Figure 81) again indicates that a red-shift in the bandgaps has occurred that is invariant to processing conditions, but now the photocatalytic efficiency of the doped material (Figure 82) is worse than that of the undoped. This general trend indicates that there is an optimal amount of Eu necessary to achieve the optimal improvement in performance, and that this occurs at trace amounts of Eu relative to the amount of TiO_2.

6.3 Enhanced Dispersion and Doping of Commercially Available TiO_2

The next attempt is to modify the Aldrich TiO_2 (#634662) powder using 1-octadecene to possibly reduce particle size and achieve longer particle suspension. The samples were dispersed and washed prior to doping with Eu at different percentages: 0.5%, 1.0%, 2.0% and 3.0%. The TEM images of the Aldrich TiO_2 (#634662) dry specimen after the dispersion synthesis shows that the particles are smaller in size (Figure 83). Once the samples were doped, they were heated at 135, 260 and 360°C. TEM image of a wet specimen (Figure 84 left) shows smaller dispersed particles. The dispersion synthesis has reduced the size of some particles to approximately 10 nm (Figure 84 right). However, the particle suspension still did not last very long and settling was observed.

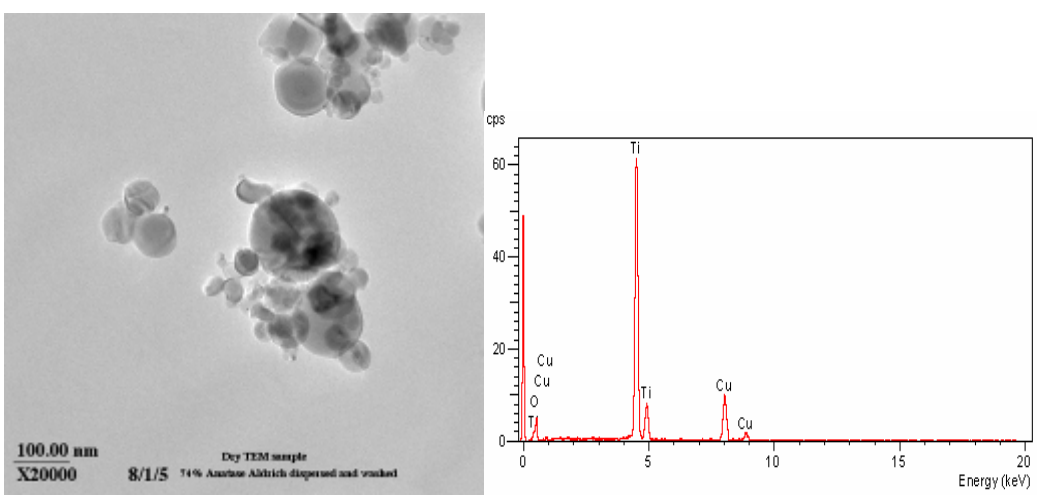

Figure 83. "Dry" TEM images of dispersed Aldrich TiO2 (#634662), showing smaller particles. The EDS spectrum shows Ti and oxygen peaks.

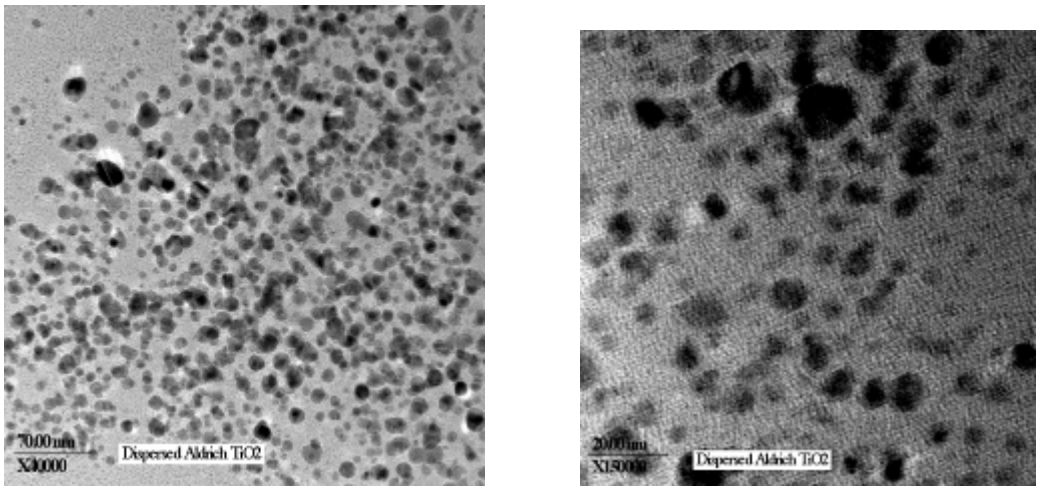

Figure 84. Left, TEM images of dispersed and washed Aldrich TiO_2. Right, image taken at a 150K magnification showing some particle sizes less than 10nm.

The TEM images of 1% Eu doped dispersed Aldrich TiO_2 of the unheated sample show that some agglomeration process begins to occur (Figure 85); the EDS spectrum confirms the composition of the TiO_2 and Eu. The image of the doped sample also shows smaller particles on larger particles. Literature suggests this may indicate the two phases: anatase and rutile.

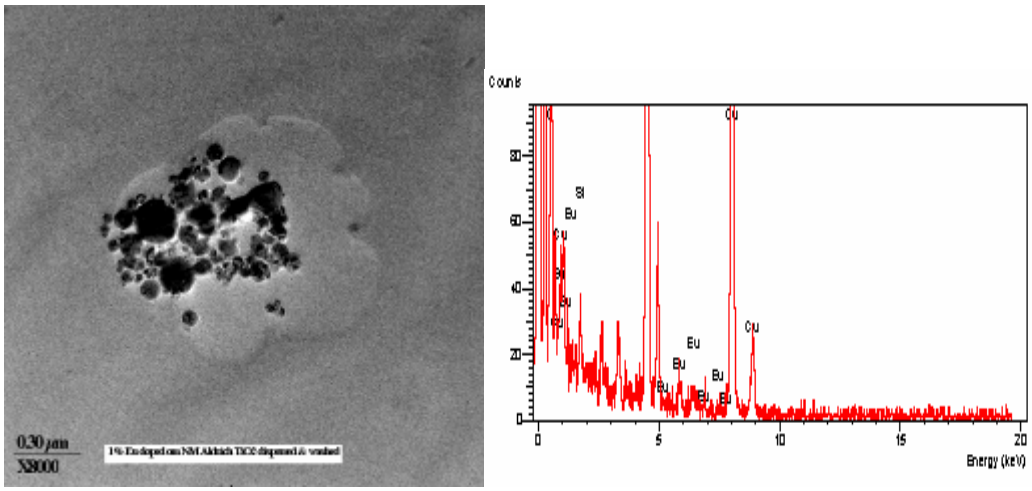

Figure 85. TEM image of 1% Eu doped dispersed Aldrich TiO2. EDS spectrum sample shows Ti (not labeled at 4-5 keV) and Eu.

TEM images of 1% Eu doped dispersed Aldrich TiO_2 heated at 135°C (Figure 86 left) and sample heated at 260°C (Figure 86 right) do not show much of a difference in the particle sizes and characteristics. EDS spectrum of each sample confirms no change in the composition. TEM images of a sample heated at 360 °C were not taken, but it is speculated that heavy agglomeration most likely occurs.

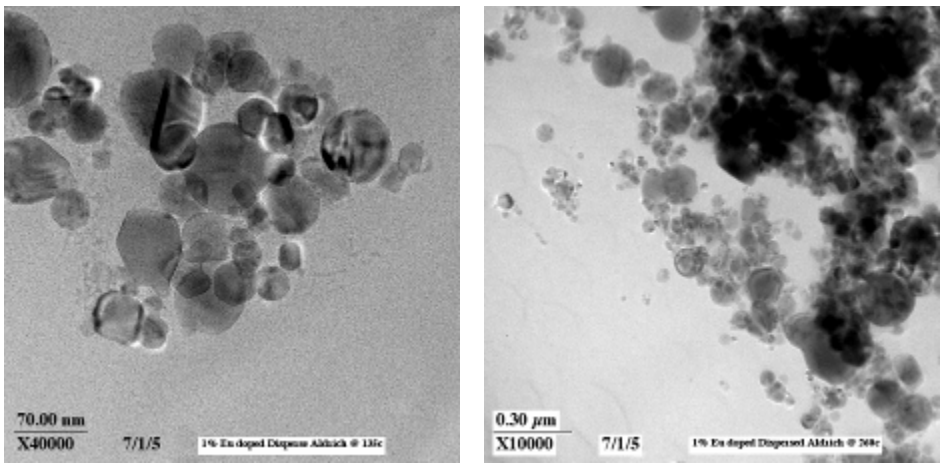

Figure 86. Left, TEM image of 1% Eu doped dispersed Aldrich TiO2 heated at 135°C. Right, TEM image of sample heated at 260°C.

Table 2. List of Sample Codes and Compositions for Eu Doped Dispersed TiO_2

Sample	Composition
JP1.86.2	1.0% $EuTiO_2$ Aldrich
JP1.86.3	2.0% $EuTiO_2$ Aldrich
JP1.87.4	1.0% $EuTiO_2$ Aldrich @ 135°C
JP1.87.5	1.0% $EuTiO_2$ Aldrich @ 260°C
JP1.87.6	1.0% $EuTiO_2$ Aldrich @ 360°C
JP1.87.7	2.0% $EuTiO_2$ Aldrich @ 135°C
JP1.87.8	2.0% $EuTiO_2$ Aldrich @ 260°C
JP1.87.9	2.0% $EuTiO_2$ Aldrich @ 360°C

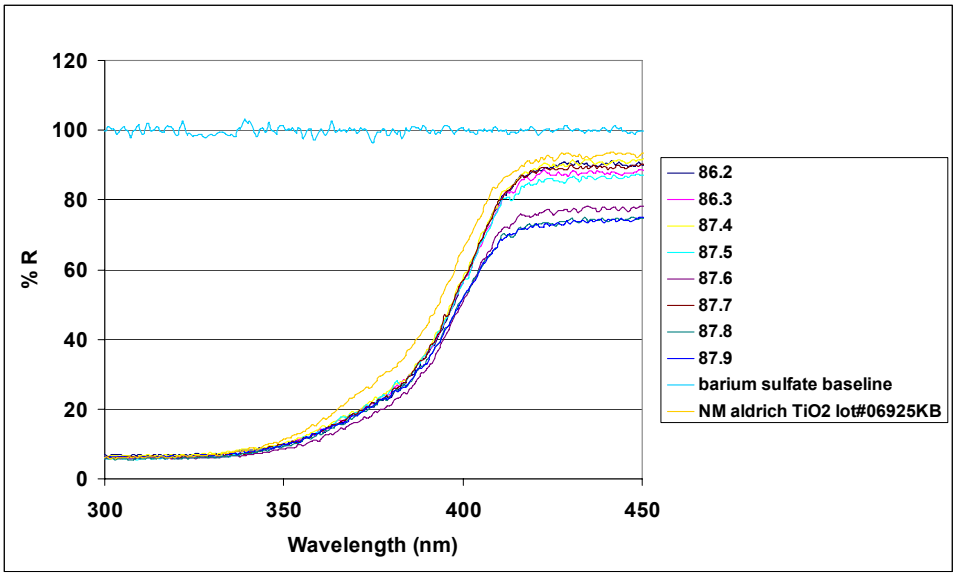

Figure 87. UV-Vis diffuse reflectance data from the Eu doped dispersed TiO_2

The diffuse reflectance data obtained from the Eu doped samples on the dispersed commercial nanocrystalline TiO_2 is presented in Figure 87. No significant red-shift in any of the bandgaps is observed, although there is a slight red-shift for the 1% Eu dopant levels that were also processed at the highest temperatures (360 ^{o}C) analyzed. This may indicate that even higher temperatures and/or adjustment of the dopant levels are needed to afford greater changes in the bandgap of the material. These materials were also evaluated in terms of photocatalytic activity at 350 nm (Figure 88). None of the samples were observed to outperform the undoped TiO_2 reference material.

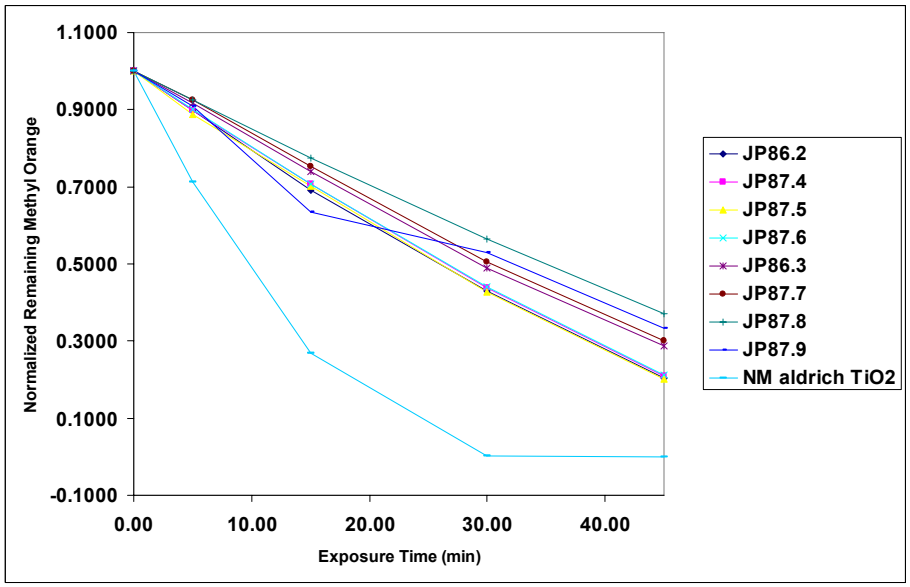

Figure 88. Plot of Photocatalytic Activity of Eu Doped/Dispersed TiO_2 with UV exposure at 350 nm.

Since the previous doping synthesis of Aldrich TiO_2 (catalog #634662) was performed with Eu metal, Yb doping was also carried out to give a photocatalytic reactivity performance comparison between the two metals. The doping of Yb was performed on both non-dispersed and dispersed Aldrich TiO_2. The previous photocatalytic reactivity analysis had shown that low weight percent doping and low temperature heating of the doped Aldrich TiO_2 appeared to be the most active. Therefore, 0.5% and 1% were used for this doping, while the samples were processed at only one temperature of 150 °C.

Table 3. List of Yb-doped Samples and Compositions for Dispersed TiO_2

Sample #	Sample Name	Composition
JP2.14.05	0.5% $YbTiO_2$ Aldrich	634662
JP2.14.10	1.0% $YbTiO_2$ Aldrich	634662
JP2.16.05.DW	0.5% $YbTiO_2$ Aldrich	634662
JP2.16.10.DW	1.0% $YbTiO_2$ Aldrich	634662
JP2.14.05.150	0.5% $YbTiO_2$ Aldrich	634662
JP2.14.10.150	1.0% $YbTiO_2$ Aldrich	634662
JP2.16.05.150.DW	0.5% $YbTiO_2$ Aldrich	634662
JP2.16.10.150.DW	1.0% $YbTiO_2$ Aldrich	634662

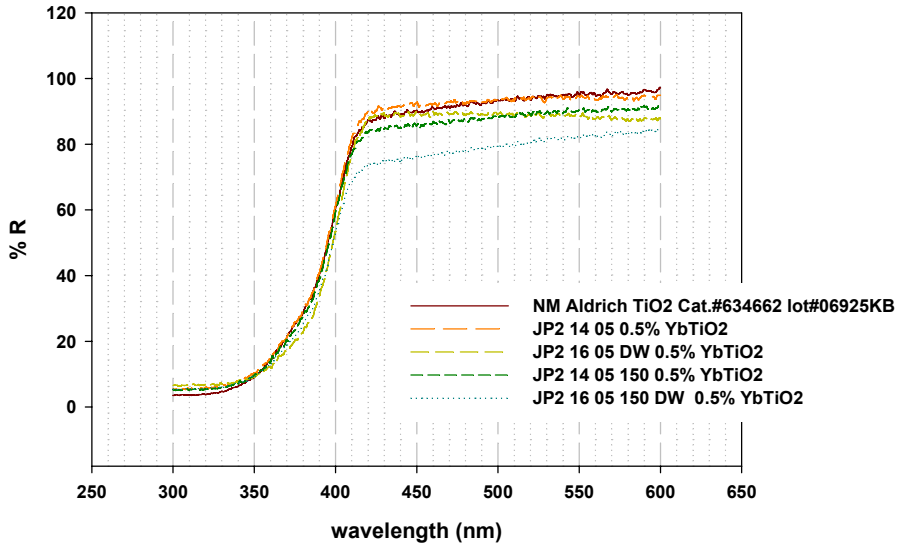

Figure 89. UV-Vis diffuse reflectance data from the 0.5% Yb doped dispersed TiO_2.

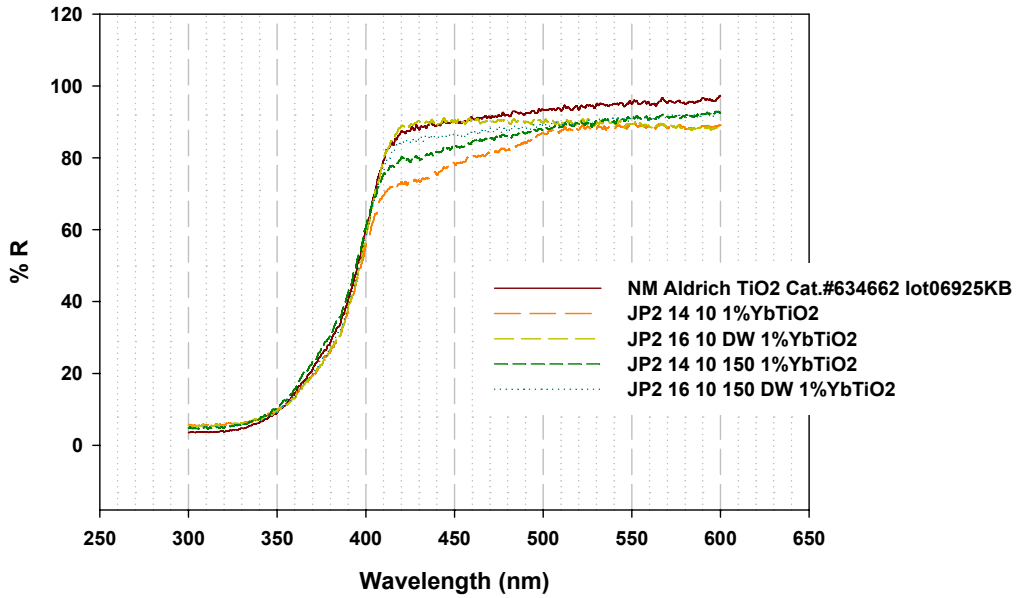

Figure 90. UV-Vis diffuse reflectance data from the 1% Yb doped dispersed TiO_2

The diffuse reflectance data for the Yb doped samples is presented in Figures 89 and 90. For the 0.5% doped samples, there is almost no shift in the observed bandgap energies. For the 1.0% doped samples, there is a slight shift in the observed bandgap towards the visible but this change is not as dramatic as was observed previously. As there was no dramatic difference in the bandgap energies, these samples were not evaluated in the photochemical reactor.

7. Summary

We have explored several different avenues in order to develop a more thorough understanding of the photocatalytic processes and important characteristics that make a good photocatalyst. There are numerous reports in the literature as to how to synthesize nanocrystalline materials, and we have utilized several of those as well as developed our own techniques in the pursuit of that goal. We have investigated the surface science of photocatalysis utilizing our expertise with LEEM. We have also taken multiple approaches to obtain both substitutionally doped TiO_2, as well as other routes to introduce either noble metals and/or lanthanides within a TiO_2 framework, and vice versa. We have also investigated the impact of synthesizing a "fresh" batch of TiO_2 for each dopant experiment as compared to trying to modify commercially available nanocrystalline TiO2. We have found that the lanthanide dopants formed through either a mixed hydrolysis or high-temperature seeding route to be the most effective in terms of improving the photocatalytic efficiency as compared to undoped nanocrystalline TiO_2 under UV illumination conditions. The best performing photocatalysts under visible lighting conditions were doped with both nitrogen and rare earth metal oxides.

Distribution

Internal:

1	MS 9161	K. F. McCarty, 8761
1	MS 9292	B. A. Simmons, 8764
1	MS 1349	T. J. Boyle, 1815
1	MS 9403	T. Zifer, 8762
1	MS 8764	E. Cruz, Org 8674
1	MS 1415	D. R. Jennison, Org 1114
1	MS 9403	D. H. Morse, 8772
1	MS 1349	R. A. Kemp, 1815
2	MS 0899	Technical Library, 4536
2	MS 9960	Central Technical Files, 8945-1